The impact of a seaward port expansion on maintenance dredging in the Port of Rotterdam

MSc Thesis

Sjoerd van der Lugt

Delft University of Technology

TU Delft

The impact of a seaward port expansion on maintenance dredging in the Port of Rotterdam

MSc Thesis

in partial fulfilment of the requirements for the degree of
Master of Science in Civil Engineering
at the Delft University of Technology

by

Sjoerd van der Lugt

S. van der Lugt
4921763

Thesis committee:	Dr. A. Kirichek	Delft University of Technology, chair
	Dr. ir. B.C. van Prooijen	Delft University of Technology
	Dr. L.M. Keyzer	Port of Rotterdam, external supervisor
	Ir. S. Neumann	Port of Rotterdam, external supervisor
Project Duration:	October, 2025 – June, 2026	
Faculty:	Faculty of Civil Engineering and Geosciences, Delft	

Cover: Aerial photo of the Port of Rotterdam.

TU Delft

Abstract

The Port of Rotterdam is the dominant maritime gateway of the North Sea region and has repeatedly expanded seaward to accommodate increasing maritime, industrial, and logistical demand. Following large-scale developments such as Maasvlakte 2, the Port of Rotterdam is now assessing new spatial expansion options. One option is a direct seaward extension of Maasvlakte 2, referred to as a Seaward Port Expansion (SPE). Five design alternatives have been developed for this concept, denoted A1, A2, B1, B2, and C, representing progressively larger seaward extensions.

An important concern for the Port of Rotterdam is the potential effect that a future seaward expansion may have on fine sediment dynamics and, consequently, on maintenance dredging. The Port of Rotterdam depends on continuous dredging to maintain nautical depths in its access channels and port basins. After the construction of Maasvlakte 2, annual maintenance dredging volumes increased substantially, from $4.5\ \mathrm{Mm^3/yr}$ before construction to more than $10\ \mathrm{Mm^3/yr}$ in subsequent years. This raises the question of whether a future SPE could trigger an increase in siltation and dredging demand. The central hypothesis is that the modified coastal geometry may alter flow patterns, mobilise offshore fine sediment, increase fine sediment import through the Maasmond, and thereby increase sediment accumulation within the port.

This research therefore addresses the following research question: *How do alternative SPE designs affect maintenance dredging demand in the Port of Rotterdam through changes in hydrodynamics and fine sediment transport?* To answer this question, a process-based framework is combined with numerical modelling using Delft3D-FLOW and DELWAQ. The framework tracks the response of fine sediment to the SPE designs from the offshore domain, through the Maasmond transect, and into the port basins. Fine sediment is represented by three Inorganic Matter fractions: IM1 represents clay, IM2 represents fine silt, and IM3 represents coarse silt/micro floc. The results are interpreted in a semi-quantitative manner, focusing on relative differences between the SPE designs and the Reference scenario.

The numerical modelling shows that the SPE designs strengthen tidal flow contraction around the seaward expansion, increasing flow velocities and bed shear stresses near the curvature of the designs. As the design scale increases, the zone of maximum hydrodynamic forcing and potential scour shifts southwestward towards the seaward tips of the designs. The impact of these hydrodynamic changes on fine sediment dynamics strongly depends on the sediment fraction. Clay and fine silt remain largely in suspension offshore and are therefore weakly affected. In contrast, coarse silt/micro floc exhibits a more pronounced response due to its higher settling velocity. This leads to a redistribution of this fraction across the offshore domain, characterised by reduced bed mass within the scour area and increased accumulation potential in adjacent low-energy zones north and south of Maasvlakte 2. However, the estimated release of new fines to the port system from the scour area remains limited. Even under conservative assumptions, the additional volume of fines would amount to at most $0.1\ \mathrm{Mm^3/yr}$. This would correspond to an increase of less than 1% in the current annual maintenance dredging volume of the Port of Rotterdam.

At the Maasmond transect, the SPE designs do not increase fine sediment import into the port. Clay and fine silt show only limited changes in net transport. Coarse silt/micro floc shows a more pronounced response, particularly for the larger designs: Designs B2 and C reduce net import by 4% and 9%, respectively. This reduction is mainly driven by lower near-bed sediment availability at the Maasmond. The reduced sediment availability is attributed to increased retention of coarse silt/micro floc in low-energy zones adjacent to the scour area of the larger and less streamlined designs.

Consistent with the absence of increased fine sediment import through the Maasmond, the SPE designs do not lead to a systematic increase in fine sediment accumulation within the port. Clay and fine silt show only limited changes in suspended concentration and bed mass. The reduced coarse silt/micro

floc supply through the Maasmond for Designs B2 and C leads to lower bed mass accumulation of this fraction, particularly near the Maasmond and the Beerkanaal entrance.

This research shows that the coastline change associated with the SPE does not increase marine fine sediment import into the Port of Rotterdam under regular hydrodynamic conditions. For the larger designs, increased offshore retention reduces the import of coarse silt/micro floc through the Maasmond and may therefore reduce the maintenance dredging demand associated with this fraction. Within the applied model set-up, and excluding storm events, morphodynamic feedback, and construction-phase effects, the SPE designs are therefore not expected to increase maintenance dredging demand through changes in hydrodynamics and fine sediment transport alone.

Preface

This thesis marks the final milestone of my MSc in Civil Engineering, specialising in the track of Hydraulic Engineering, and with it, a chapter as a student comes to a close. Looking back, an interest in the dynamics of water has always played a role in my life. From building small stone dams in French rivers and sandcastles on the beach, to watching freight ships navigate the Nieuwe Maas with my grandfather. It makes it all the more special to complete my MSc here, in Rotterdam.

Throughout this research, I explored how a new seaward port expansion would impact fine sediment dynamics in the port, combining numerical modelling with the complex behaviour of fine sediments. Both aspects proved challenging and rewarding in equal measure. Working on an early-stage project with real potential, in a system so vital to the Netherlands, made this research particularly compelling. Ultimately, this thesis serves as a first exploration of what may happen when Rotterdam's coastline is modified once again, and I am curious to see how this project develops in the years ahead.

I am grateful to everyone at the Port of Rotterdam for their openness and support throughout this project. I would like to especially thank Lennart for his close guidance throughout the research, and thank Sterre for her guidance and for keeping the broader perspective of this project in view. I would also like to thank my supervisors Alex and Bram for their support. Being specialists in their respective domains, ports and fine sediments, their combined expertise proved vital to the successful completion of this thesis.

Finally, I would like to thank my friends, family, and especially my parents for their unconditional support throughout this process, for which I am very grateful.

Sjoerd van der Lugt
Rotterdam, June 2026

Nomenclature

Abbreviations

Abbreviation	Definition
ETM	Estuarine Turbidity Maximum
HbR	Havenbedrijf Rotterdam
IM	Inorganic Matter
MV2	Maasvlakte 2
OSR	Operationeel Stromingsmodel Rotterdam
PoR	Port of Rotterdam
RMD	Rhine-Meuse Delta
ROFI	Region of Freshwater Influence
RWS	Rijkswaterstaat
SPE	Seaward Port Expansion
SPM	Suspended Particulate Matter
TIM	Total Inorganic Matter
TMZ	Turbidity Maximum Zone
ZWU	Zeewaartse Uitbreiding

Symbols

Symbol	Definition	Unit
A	Area	[m^2]
A_{overlap}	Overlap in scour area between the Ref. and an SPE design	[m^2]
A_{SPE}	Scour area induced by an SPE design	[m^2]
$A_{\mathrm{SPE,new}}$	New scour area induced by an SPE design	[m^2]
c	Suspended sediment concentration	[gDM/m^3]
$\overline{c}$	Temporally averaged suspended sediment concentration	[gDM/m^3]
C_{fines}	Fines content in the bed	[-]
d	Particle diameter	[m]
D	Maintenance dredging demand	[m^3/yr]
E_{MV2}	Erosion rate of the MV2 scour pit	[m^3/yr]
F	Transported fine sediment mass over a defined period	[gDM]
F_{export}	Exported fine sediment mass over a defined period	[gDM]
F_{import}	Imported fine sediment mass over a defined period	[gDM]
F_{net}	Net transported fine sediment mass over a defined period	[gDM]
H_{S}	Significant wave height	[m]
J	Suspended sediment flux	[gDM/(m^{2}s)]
J_{GF}	Godin-filtered suspended sediment flux	[gDM/(m^{2}s)]
$M_{\mathrm{S}j}$	Sediment mass in bed layer Sj, with $j = 1, 2$	[gDM]
Q	Discharge	[m^3/s]
R_A	Relative increase in scour area	[-]
S	Salinity	[ppt]

Symbol	Definition	Unit
t_0	Start of the analysis period	[-]
t_1	End of the analysis period	[-]
u	Flow velocity	[m/s]
$\overline{u}$	Depth-averaged flow velocity	[m/s]
w_s	Particle settling velocity	[m/s]
$\Delta E_{\mathrm{fines,SPE}}$	Release rate of fine sediment from the SPE-induced new scour area	[gDM/s]
$\Delta F^{\mathrm{IM}}_{m,\sigma,\mathrm{norm}}$	Normalised transport difference of IM fraction at grid cell (m, σ)	[-]
ΔM_{bed}	Net change in bed mass over the analysis period	[gDM]
Δt	Numerical time step	[s]
u_{wind}	Wind velocity	[m/s]
ΔV_{SPE}	Relative increase in SPE-induced scour volume	[-]
ΔX	Relative difference in variable X between SPE and Reference	[-]
ϵ	Residual error	[-]
η	Water level	[m]
τ_b	Bed shear stress	[N/m^2]
τ_{cr}	Critical bed shear stress	[N/m^2]
$\tau_{\mathrm{cr,S}j}$	Critical bed shear stress of bed layer Sj, with $j = 1, 2$	[N/m^2]

Contents

List of Figures

List of Tables

1 Introduction

1.1. Research context

Deltas and coastal regions host nearly half of the world's population, with ports serving as key economic hubs within these areas. The Port of Rotterdam has long been the dominant maritime gateway of the North Sea region and has adapted to increasing demand through successive large-scale developments, including Europoort (1964-1966), Slufterdam (1986–1987), Maasvlakte (1964–1976) and Maasvlakte 2 (2008–2013) (Van Der Spek et al. 2020). These interventions, together with other anthropogenic modifications, have all reshaped the Rhine-Meuse Delta.

Basins and access channels in the Port of Rotterdam do not naturally meet the nautical depths required for modern shipping, making maintenance dredging an essential and continuous operational activity (Cronin et al. 2019). Between 1997 and the start of the Maasvlakte 2 construction in 2008, annual dredging volumes remained relatively stable at approximately 4.5 Mm^3/year, as depicted in Figure 1.1. In the subsequent period, volumes increased to over 10 Mm^3/year. Although this increase cannot be attributed to a single intervention, the construction of Maasvlakte 2, successive deepening of the Nieuwe Waterweg and Botlek, and the development of additional berths have collectively altered hydrodynamic conditions and sediment transport. These system-scale modifications have increased sedimentation rates within port basins and access channels, driving higher maintenance dredging demand in subsequent years (Bruijn 2018; Cox et al. 2021). Dredged material in the port consists predominantly of fine sediment from two sources: marine silts advected from the North Sea and English Channel, and fluvial fines from the Rhine–Meuse Delta (Suijlen et al. 2002; Kirichek et al. 2018). Inner harbour basins contain 90–100% fluvial mud (De Nijs et al. 2010), while marine fine sediment dominates the basins near the seaward entrance (Salomons et al. 2001), where estuarine circulation drives fine sediment import from the North Sea (De Nijs et al. 2010).

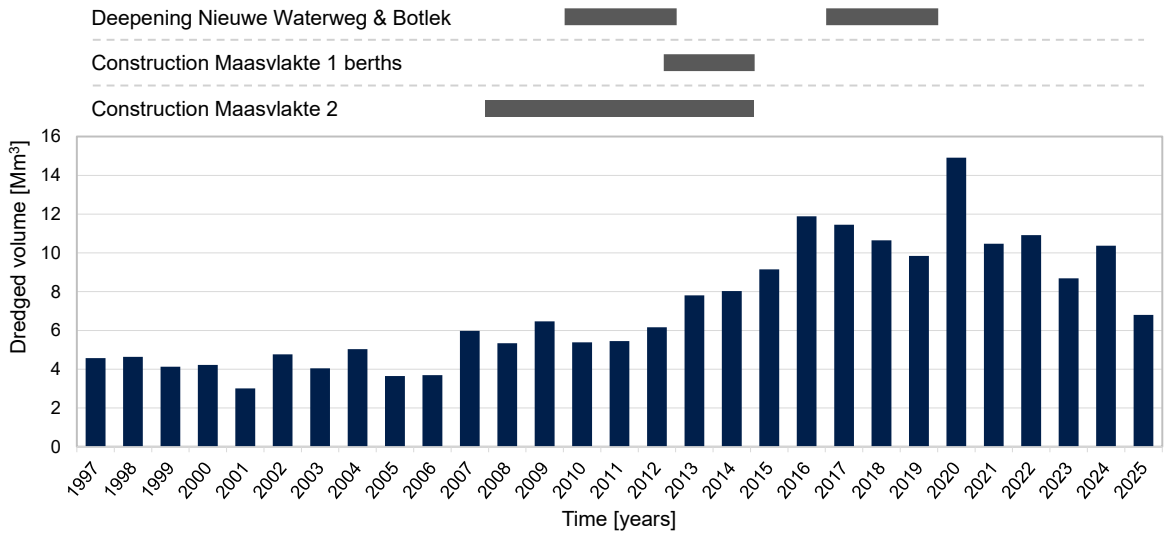

Figure 1.1: Annual maintenance dredging volumes by the Port of Rotterdam for the period 1997–2025, with grey bars indicating major infrastructure developments. Data source: Port of Rotterdam.

Figure 1.2: Satellite image showing the designated area for the SPE, bounded by the PKB Maasvlakte 2 sightline from Voorne (Haringvlietlijn) and the demarcation line defining the current municipal boundary between Rotterdam and Voorne aan Zee (NOVEX 2025).

To accommodate future port activities, the Port of Rotterdam (PoR) is assessing spatial expansion options within the NOVEX programme, a national framework guiding port and industrial development (Port of Rotterdam 2023). The alternatives under consideration include relocation or restructuring of existing port operations, intensification of the current port area, and a seaward expansion by land reclamation. The latter is referred to as the Seaward Port Expansion (SPE). The designated SPE area, a direct seaward extension of Maasvlakte 2, is shown in Figure 1.2.

The SPE project is currently in the feasibility phase, in which technical, environmental, financial, and operational implications are assessed (NOVEX 2025). Five design alternatives are evaluated, varying in size, geometry, and boundary configuration (Figure 1.3). The considered design scenarios are:

- **Design A1:** seaward extension of 377 ha with a compact and streamlined layout.
- **Design A2:** seaward extension of 447 ha with a compact and streamlined layout.
- **Design B1:** seaward extension of 626 ha with a compact and streamlined layout.
- **Design B2:** seaward extension of 785 ha with a compact and streamlined layout.
- **Design C:** seaward extension of 980 ha with a less compact and less streamlined layout, including an additional harbour basin extending the existing Prinses Arianehaven in Maasvlakte 2.

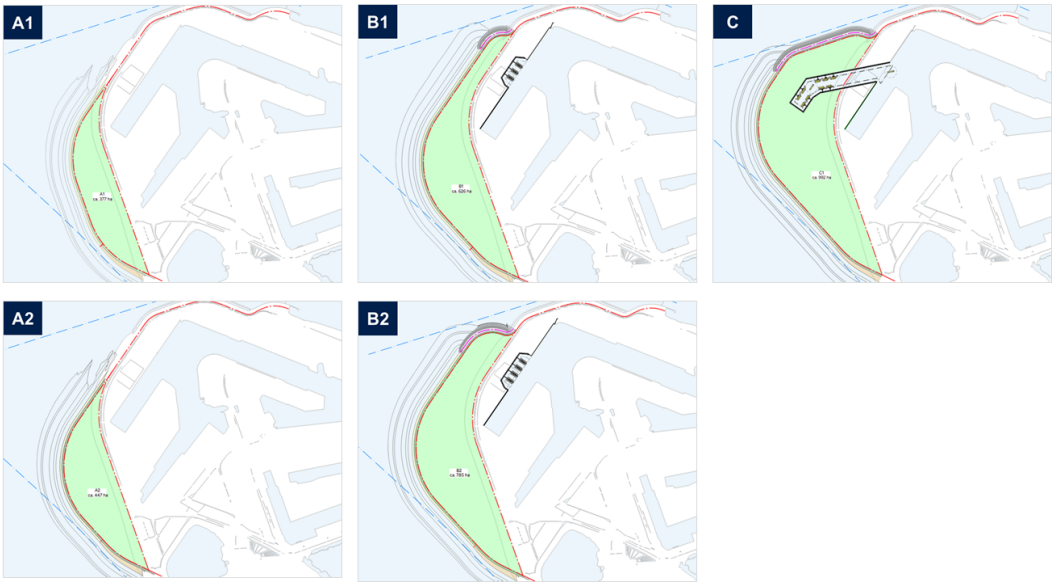

Figure 1.3: Map of the seaward side of Maasvlakte showing the proposed SPE design alternatives A1, A2, B1, B2, and C. The green areas indicate the spatial footprint of each expansion geometry (NOVEX 2025).

Key design challenges of the SPE include long-term morphological responses such as scour development and coastal maintenance under sea-level rise, as well as ecological compensation within Natura 2000 areas (NOVEX 2025). A recent study by Verbruggen et al. (2025) assessed the nautical safety implications of various SPE layouts. However, the potential impact of the SPE on fine sediment dynamics and maintenance dredging demand remains uncertain. This uncertainty is relevant because the construction of Maasvlakte 2 showed that large-scale port expansion can substantially affect dredging volumes, as illustrated in Figure 1.1.

1.2. Problem description

The SPE will modify the coastal geometry of MV2 and is expected to alter local hydrodynamic conditions, including flow patterns, flow velocity, and consequently bed shear stress. Experience from the construction of MV2 shows that a seaward coastline extension contracts the tidal flow domain, locally increasing velocities and altering sediment transport patterns (Van Kessel 2005). The resulting increased bed shear stress induced erosion of fine sediment from the coastal zone, increasing suspended particulate matter (SPM) availability (Berkenbosch et al. 2006). These modified flow conditions could drive a long-term structural change in fine sediment dynamics, increasing import through the Maasmond and into port basins, potentially raising sedimentation and maintenance dredging demand. Beyond this

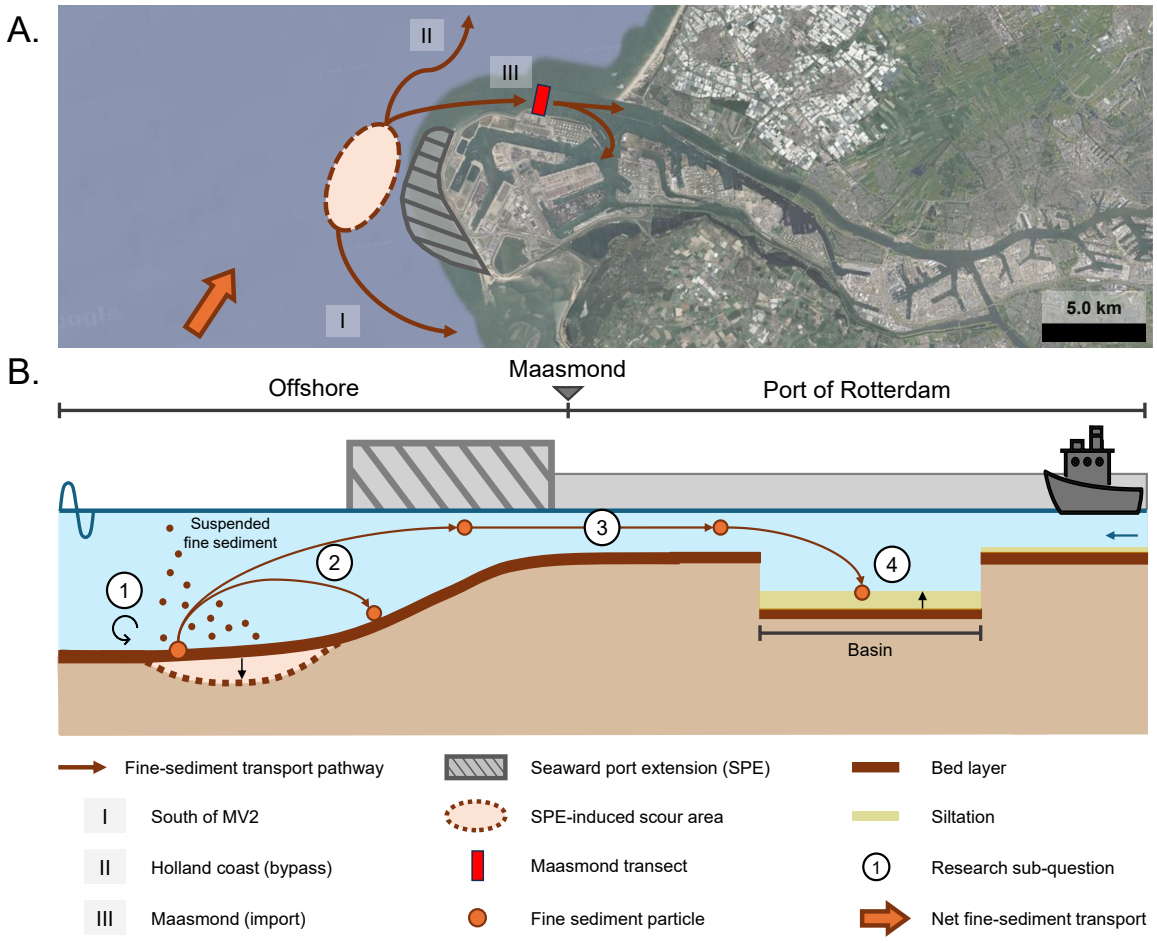

Figure 1.4: Conceptual overview of the research domain and hypothesis. The upper panel shows a satellite image of the Port of Rotterdam, including a schematization of the SPE design, the potential SPE-induced scour area, and the potential fine sediment transport pathways: transport towards the area south of MV2 (I), bypassing of fine sediment entering the Holland coast (II), and transport through the Maasmond into the port (III). The lower panel presents a schematized longitudinal section of the port system, tracing fine sediment from the offshore zone towards the port basins and illustrating the hypothesised chain of SPE-induced effects: hydrodynamic modification (1), offshore fine sediment redistribution (2), transport through the Maasmond (3), and accumulation within the port system (4). These four components also form the basis of the research sub-questions.

long-term shift, short-term fine sediment sources include the release of fines during the construction of the reclamation and the formation of a new scour hole.

This uncertainty is directly relevant for decision-making within the Port of Rotterdam. The SPE team requires early-stage insight into the hydrodynamic and sediment transport response to alternative lay-outs in order to evaluate design performance and identify potential system impacts. The Asset Management department, responsible for maintenance dredging of port basins, requires reliable estimates of changes in fine sediment accumulation, as dredging volumes are a key driver of long-term operational costs. Rijkswaterstaat (RWS), responsible for maintaining navigability of the Rotterdam Waterway, holds an indirect interest, as system-scale changes in sediment dynamics may also influence siltation in the main navigation channel. The core problem is therefore whether, and to what extent, the SPE will alter fine sediment dynamics in a way that increases siltation and maintenance dredging demand in the PoR.

This research addresses that problem by quantifying the impact of the SPE on fine sediment dynamics. The central hypothesis, depicted in Figure 1.4, is that the SPE will contract the tidal flow domain, increase flow velocities, and alter flow patterns in a manner analogous to MV2. This would affect both fine sediment mobilisation through the induced scour area and the transport pathway along the structure towards the Maasmond, thereby increasing the import of marine fine sediment into the port system and raising siltation and dredging demand. Sediment release is expected to diminish over time as the system reaches a new dynamic equilibrium; however, if transport pathways are significantly altered, the shift in system dynamics may be structural. Critically, the magnitude and spatial distribution of these effects are expected to differ between SPE design alternatives, making this a key consideration in design evaluation.

1.3. Research questions

The research questions translate the hypothesis into a structured set of process-based questions. These questions assess how alternative SPE designs influence hydrodynamics, fine sediment transport, and maintenance dredging demand, following the analogy of Figure 1.4.

Research question

The main research question is:

How do alternative seaward port expansion (SPE) designs affect maintenance dredging demand in the Port of Rotterdam through changes in hydrodynamics and fine sediment transport?

To address the main research question, the following sub-questions are formulated:

1. How do SPE designs influence flow velocity fields and bed shear stress offshore?
2. How do SPE designs influence the spatial redistribution of fine sediment offshore, including the formation of an erosion pit?
3. How do the SPE designs change fine sediment transport through the Maasmond transect?
4. How do SPE designs alter fine sediment accumulation within the port waterways and basins, and what do these changes imply for maintenance dredging?

1.4. Scope

This research isolates the effect of the change in coastline geometry following the construction of an SPE. The SPE designs are expected to modify flow patterns, fine sediment transport, and sedimentation patterns relevant to maintenance dredging in the Port of Rotterdam. The scope is defined by the following conditions and limitations:

1. This research focuses on regular hydrodynamic conditions in the Dutch coastal zone over multiple spring–neap cycles. Although high-energy events, such as storms, can strongly affect fine sediment mobilisation and import (Verlaan et al. 2000), these events are not included in this study.
2. This analysis is limited to fine sediments (d < 63 μm) (Winterwerp et al. 2004; Bosboom et al. 2023), as these fractions primarily govern the dredged material in the port basins. Coarser sediments, such as sand, fall outside the scope of this study.
3. This research focuses on the short-term system response (<5 years) to the modified coastal geometry. The SPE is assumed to be implemented instantaneously; therefore, construction-phase effects and long-term morphodynamic adaptation of the coastline and seabed are not considered.

Additionally, the following aspects are considered outside the scope of this research: the effects of sand mining pits, long-term developments such as sea-level rise, and broader port impacts unrelated to maintenance dredging, including navigation, ecology, recreation, and logistics.

1.5. Research objectives

This research tracks fine sediment movement through the system using a process-based framework, building on Hendriks et al. (2020). Their conceptual framework characterises sediment dynamics in the Dutch coastal zone in terms of (1) sources, (2) transport pathways, and (3) accumulation potential, and their response to human interventions. In the present research, this structure is adapted to the research hyptohesis, progressing from (1) offshore hydrodynamics and sediment mobilisation, (2) transport through the Maasmond, to (3) accumulation within the port.

Furthermore, to quantitatively compare the SPE alternatives, a numerical modelling approach is applied in which only the coastal geometry is varied, while all hydrodynamic boundary conditions remain identical. This allows the impact of the seaward port expansion to be isolated and evaluated consistently.

Research objectives

To answer the research question, the following objectives are defined:

1. Establish a process-based framework describing the key hydrodynamic and fine sediment transport mechanisms governing (1) offshore fine sediment mobilisation, (2) transport through the Maasmond, and (3) accumulation within the Port of Rotterdam.

2. Apply and validate a numerical modelling sequence to simulate hydrodynamics and fine sediment transport for the reference scenario and the SPE designs.

1.6. Research structure

The structure of the thesis is illustrated in Figure 1.5. The three domains defined in the hypothesis, namely the offshore zone, transect, and port, are each addressed in a separate results chapter because they require distinct methodological approaches.

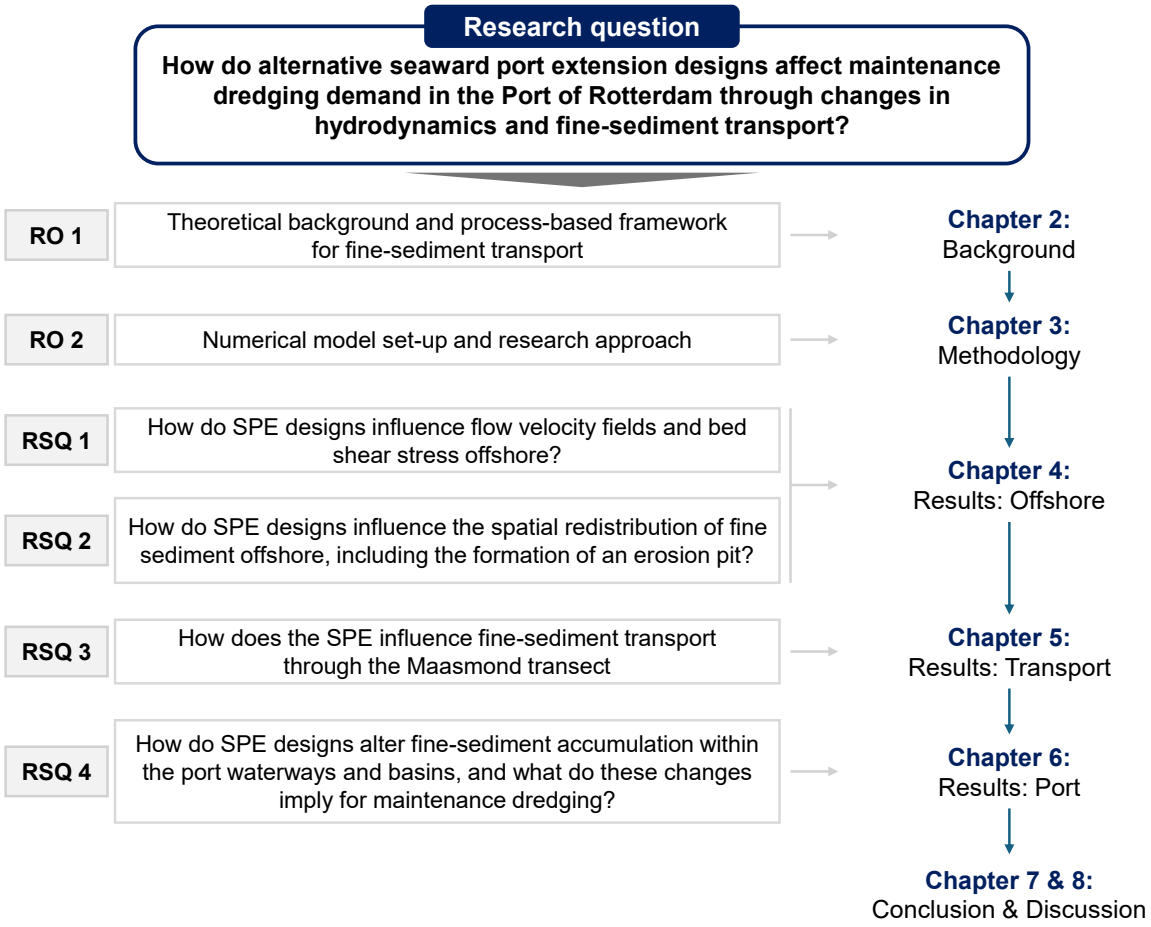

Figure 1.5: Structure of the thesis. The main research question is translated into research objectives (ROs) and research sub-questions (RSQs), which are addressed in the corresponding chapters of this report.

2
Background

This chapter establishes the theoretical foundation for this research, covering both fine sediment dynamics and the relevant characteristics of the Port of Rotterdam system. Section 2.1 characterises fine sediment properties. Section 2.2 addresses fine sediment behaviour in the Dutch coastal zone. Section 2.3 covers sediment transport through the port system, with the Maasmond as the primary exchange pathway between the offshore zone and the port. Section 2.4 discusses fine sediment accumulation within the Port of Rotterdam. Section 2.5 synthesises the key theoretical insights and identifies the implications most relevant to this research.

Figure 2.1 presents the conceptual framework underlying this research, derived from the hypothesis and sub-questions formulated in Chapter 1 and building on the framework developed by Hendriks et al. (2020). The conceptual framework structures the theoretical background by linking the research sub-questions to successive components of the sediment pathway: offshore dynamics, transport through the Maasmond, and accumulation within the port.

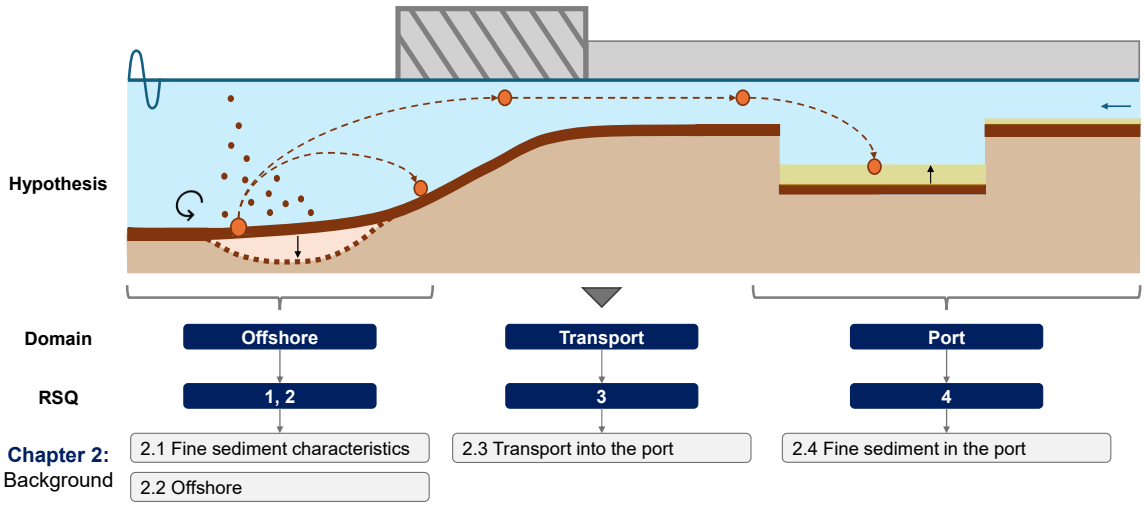

Figure 2.1: Conceptual framework for tracking fine sediment from the offshore domain towards the port, based on the hypothesis presented in Figure 1.4. The framework structures the analysis of the hypothesised fine sediment pathway across three domains: offshore, transport, and port. These domains form the basis for the sections in Chapter 2.

2.1. Fine sediment characteristics

Fine sediments are defined as particles smaller than 63 μm, encompassing silt (2–63 μm) and clay (<2 μm) (Winterwerp et al. 2004; Bosboom et al. 2023). These sediments are subject to a range of interacting transport and depositional processes, the most important of which are schematised in Figure 2.2. Due to their low individual settling velocities (w_s), these particles are primarily transported in suspension through turbulence. In this state, commonly referred to as Suspended Particulate Matter (SPM), they can be transported over considerable distances (Bosboom et al. 2023).

Flocculation processes control the aggregation and effective grain size of fine sediments, thereby determining the settling velocity and the resulting sedimentation rate (Bruens 1999). Flocculation is a reversible process in which chemical forces and turbulent shear cause fine sediment particles to collide and aggregate into larger units known as flocs. These flocs can exhibit significantly higher settling velocities than individual grains (Partheniades 2009). The interplay of these processes makes the settling velocity of fine sediments inherently difficult to constrain, though a conservative upper bound is established at w_s < 1 cm/s (Dronkers 1986). Under low-energy hydrodynamic conditions, such as those found in sheltered basins, river beds, or inter-trough regions, fine sediments accumulate to form a fluid mud layer, also referred to as a fluff layer (Bruens 1999). This fluff layer of fresh fine-grained deposits is characterised by a low critical shear stress (τ_{cr}) for erosion, in the order of 0.1–0.2 Pa (Van Kessel et al. 2023). Given sufficient time, this layer gradually consolidates into the bed, which is more compact and has a critical bed shear stress in the order of 0.5–1 Pa (Van Kessel et al. 2023).

Conversely, erosion and resuspension occur when the applied bed shear stress (τ_b) from currents, waves, or ships exceeds the critical shear stress threshold, re-entraining fine sediment into the water column (Winterwerp et al. 2004). Land reclamations and hydraulic structures modify local flow velocities and thereby bed shear stress, and can induce localised scour (Waal 2025). Scour hole evolution follows four phases: initial, development, stabilisation, and equilibrium, with erosion rates highest in the initial phase and progressively declining as the scour hole approaches a stable geometry (Hoffmans et al. 2021). The extent and character of this scour area depend on bed composition, sediment class, grain size distribution, and physical properties of the substrate (Hoffmans et al. 2021). In poorly sorted beds, the preferential removal of finer particles progressively forms a coarse surface layer; once fines are depleted, this armour layer raises the local critical shear stress and limits further erosion (Bosboom et al. 2023). Beyond this point, fine sediment concentration becomes controlled by the regional availability of erodible material rather than transport capacity, indicating supply-limited behaviour (Van Kessel et al. 2023). The release of fines from SPE-induced scour will depend not only on hydrodynamic forcing, but also on the fines content of the local seabed.

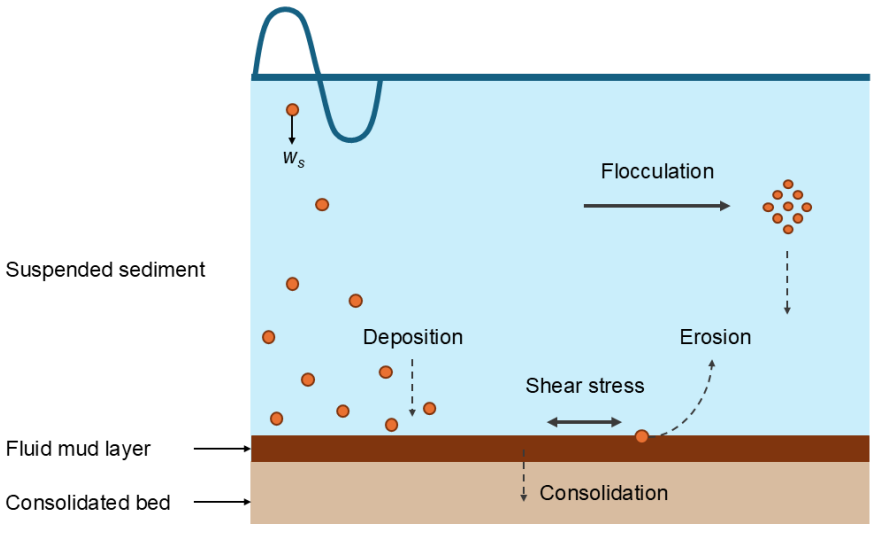

Figure 2.2: Conceptual figure of fine sediment dynamics (Van Kessel 1997).

2.2. Offshore

Marine suspended sediments in the Dutch coastal zone originate from the English Channel and the Flemish Banks and are transported within a narrow band of approximately 10 km, with a flux of around 20 Mton/year (Suijlen et al. 2002; Van Kessel et al. 2023). Along the Dutch coast, this transport is directed northward and is largely governed by tidal currents, including their interaction with the Rhine ROFI (Region of Freshwater Influence) (Souza et al. 1996; Pietrzak et al. 2011). Freshwater discharge from the Rhine-Meuse estuary generates a cross-shore salinity gradient (Souza et al. 1996), which drives a net shoreward transport of fine material in the near-bed layer and can lead to the formation of high-turbidity zones (Jay et al. 2007; De Boer et al. 2009). These high-concentration zones influence a wide range of ecological processes and environmental challenges, while their accumulation in waterways and basins leads to the need for dredging (Jay et al. 2007).

The resulting SPM concentrations in the Dutch coastal zone are characterized by strong spatial and temporal variability. In general, concentrations are highest in the nearshore zone, where they may exceed 30 mg/L, and decrease further offshore to below 5 mg/L (Suijlen et al. 2002). In the coastal zone north of the port entrance, local SPM concentrations are substantially higher, with peak concentrations of more than 500 mg/L occurring around 1.25–1.5 km from the shoreline (Van Der Hout et al. 2015; Flores et al. 2020). This coastal turbidity maximum zone (TMZ) forms when tidal straining induces asymmetries in vertical mixing, resulting in cross-shore sediment convergence and trapping of SPM in a zone detached from the shoreline (Flores et al. 2020). The TMZ extends at least 80 km north of the Rhine-Meuse estuary mouth (Van Der Hout et al. 2015). Due to vertical stratification, these high concentrations are generally confined to the lower half of the water column (Pietrzak et al. 2011). In addition to the spatial variability, SPM concentrations also vary strongly in time, with storm events increasing nearshore SPM concentrations to more than 100 mg/L (Suijlen et al. 2002).

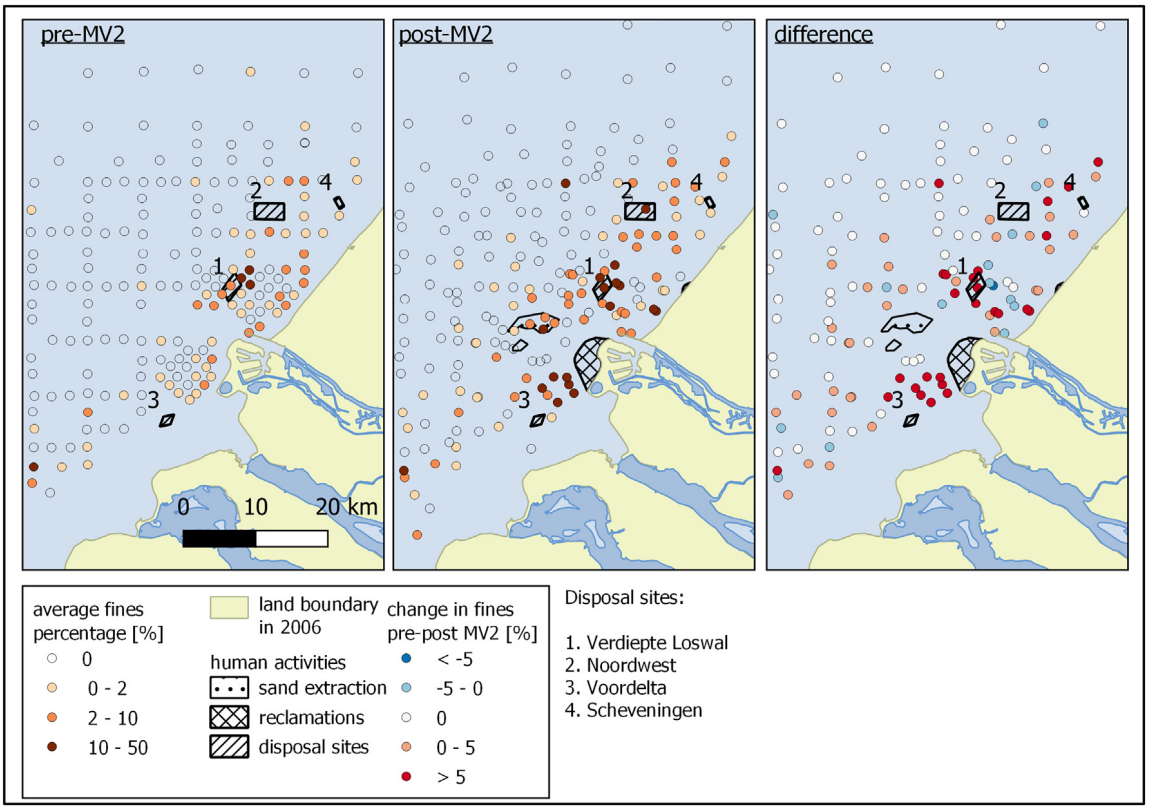

Figure 2.3: Measurement campaign of the content of fines in the Dutch coastal zone by Hendriks et al. (2020). Measurement locations are indicated by circles, with the colour scale representing the fines content. The left and middle panels show the fines content before and after the construction of Maasvlakte 2, respectively, while the right panel shows the corresponding difference.

The seabed of the southern North Sea is characterised as predominantly sandy, with a relatively low fine sediment content (Rijn et al. 2007; Van Alphen 1990). A study by Hendriks et al. (2020) used seabed samples to analyse the spatial distribution of fines across the Dutch coastal zone and the seabed response to large-scale human interventions. As depicted in Figure 2.3, fines are largely absent beyond 20 km offshore. Closer to shore, spatial variability occurs at both small (tens of metres) and medium (kilometres) scales, with local fines percentages exceeding 10–20%. Consistent with the TMZ, the highest content of fines occurs within 2–3 km of the shoreline, particularly north and south of the Rhine outflow and in former tidal channels fronting closed estuaries. Large-scale human interventions can cause local changes of 10% or more in seabed fines content, as illustrated in Figure 2.3. The construction of MV2 altered the local fines distribution through two mechanisms: additional supply of fines from overflow during sand mining, and changes in local accumulation potential; most notably in the deep mining pit and the sheltered zone to the south of MV2 (Hendriks et al. 2020).

At a smaller scale, the MV2 reclamation caused a contraction of the tidal flow around the structure, increasing local flow velocities and driving the formation of a scour area (Berkenbosch et al. 2006; Boer et al. 2007). Progressive slope steepening of the scour area poses a threat to the stability of the reclamation, potentially necessitating scour protection measures. The scour area has been monitored annually by PUMA since the completion of MV2 in 2013. The scour area currently covers an area of 282 ha, reaching depths of up to -20 m NAP, as depicted in Figure 2.4. Over the 12-year monitoring period, the pit has deepened at an average rate of 15–22 cm/year (Waal 2025). Erosion rates were highest in the years immediately following completion of MV2, peaking at 2 Mm^3/year in 2016, and have since declined to 0.8 Mm^3/year (Waal 2025). Over the full 2013–2025 period, total erosion below the initial survey bed level was estimated at 8.3 Mm^3, thus averaging 0.69 Mm^3/year (Waal 2025). These volumes represent total sediment erosion, without distinction between sand and fine fractions.

Kroon et al. (2025) recently assessed the expected growth of the scour area for different SPE design layouts using a FINEL2D model, with results summarised in Table 2.1. In general, larger designs produce greater increases in both scour volume and area. For Designs A1, A2, and B1, maximum scour depth is expected to decrease locally due to reduced flow velocities at the current positions of coastal curvature. Design C, by contrast, produces the strongest tidal flow contraction, concentrating scour at a single location. This results in the greatest projected increase in local scour depth, though over a smaller area than Design B2. These projections carry considerable uncertainty, with ranges spanning from -50% to +200%, and should be treated with caution pending further analysis.

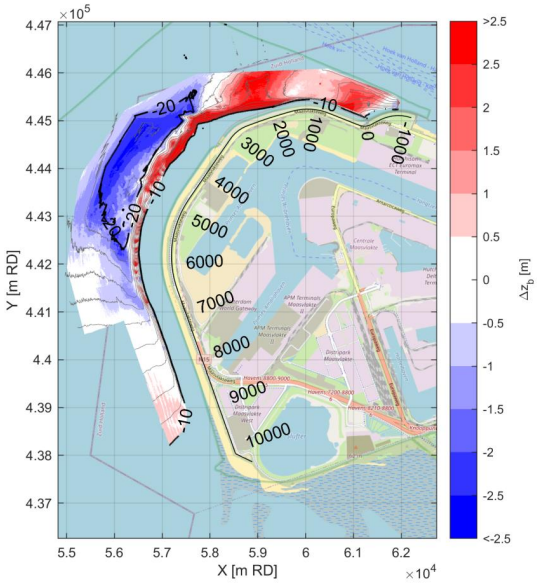

Figure 2.4: Observed bathymetry changes around Maasvlakte 2 between 2013 and 2024 (Kroon et al. 2025).

Design	ΔA (%)	Δh (%)	ΔV (%)
A1	20	−20	10
A2	30	−20	10
B1	50	−20	30
B2	70	0	60
C	50	50	90

Table 2.1: Projected changes in the dimensions of the Maasvlakte 2 scour area for the different SPE designs. Relative changes in dimensions are reported for the area (ΔA), depth (Δh), and volume (ΔV) (Kroon et al. 2025).

2.3. Transport into the port

Exchange of water and fine sediment between the North Sea and the Port of Rotterdam occurs through the Maasmond, located downstream of the Nieuwe Waterweg and Calandkanaal, as depicted in Figure 2.5. The net transport across this transect reflects the balance between landward import and seaward export of suspended sediment (Dronkers 1986).

Horizontal fine sediment transport through the Maasmond is primarily controlled by advection and turbulent mixing. In suspension, fine particles are advected by the mean flow, while turbulence redistributes sediment over the water column and counteracts gravitational settling (Winterwerp et al. 2004; Franca. et al. 2019). The resulting sediment flux depends on the joint variation of flow velocity and suspended sediment concentration (Fischer 1972; Partheniades 2009). Because both variables vary over depth, across the channel, and during the tidal cycle, fine sediment transport through the Maasmond is inherently spatially and temporally variable.

The flow structure at the Maasmond is controlled by the interaction between river discharge, tidal forcing, waves, and density-driven exchange. Due to salinity intrusion from the North Sea, the lower part of the water column contains dense saline water moving landward, while fresher river water flows seaward near the surface (Fischer 1972; Lerczak et al. 2006; De Nijs et al. 2010). This produces a two-layer exchange flow in which surface and near-bed velocities may be directed oppositely. Figure 2.6 shows the longitudinal velocity and salinity profile at the Maasmond during the tidal phase with maximum near-bed flow. The figure illustrates that high near-bed landward velocities coincide with saline water entering the Nieuwe Waterweg, while seaward flow occurs closer to the surface.

Near-bed landward flow drives fine sediment import because suspended sediment concentrations are elevated in the lower part of the water column (Hendriks et al. 2025). A persistent salt wedge in the Nieuwe Waterweg reinforces this mechanism by maintaining near-bed saline inflow into the port system, facilitating the landward transport of marine fines (De Nijs et al. 2009). The highest near-bed velocities at the Maasmond occur before or around high water and are associated with the intrusion of high-salinity water into the Nieuwe Waterweg (De Nijs et al. 2011).

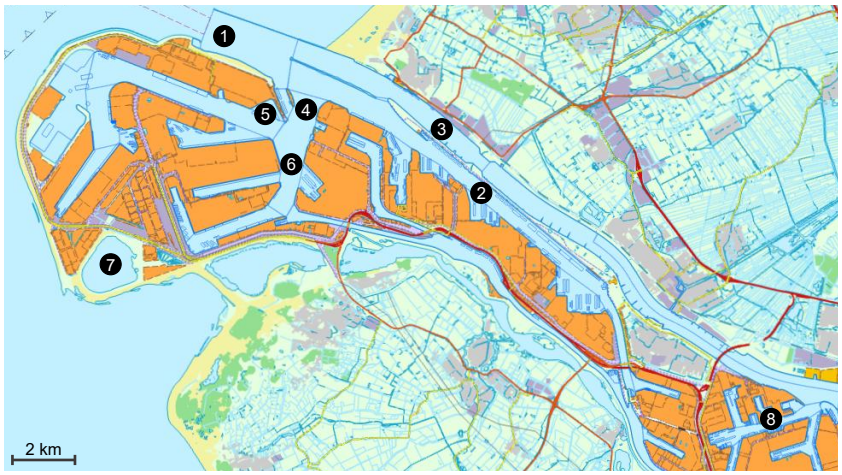

	Location
1	Maasmond
2	Calandkanaal
3	Nieuwe Waterweg
4	Westbocht
5	8th Petroleumhaven
6	Beerkanaal
7	Slufter
8	Botlek

Figure 2.5: Map of the western port area of the Port of Rotterdam, showing the main locations referred to in this study and listed in the accompanying table. Base map retrieved from the Port of Rotterdam.

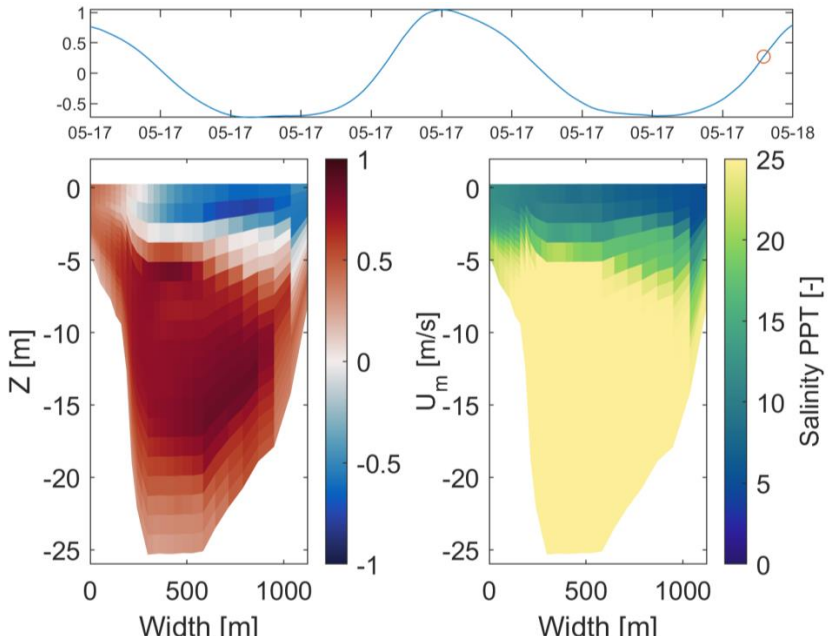

Figure 2.6: Prototypical two-dimensional vertical (2DV) velocity and salinity structure near the river mouth at the Maasmond during the tidal phase with maximum near-bed flow. The left panel shows the distribution of the longitudinal flow velocity over the depth and width, where red indicates landward flow and blue indicates seaward flow. The right panel shows salinity in parts per thousand. Figure obtained from De Wit et al. (2022).

The advective transport of suspended sediment can be described using the flux formulation (Clark 2009). The sediment flux vector expresses the local transport of suspended sediment as the product of flow velocity and suspended sediment concentration:

$$\mathbf{J} = c\,\mathbf{u} \tag{2.1}$$

Integration of the normal component of this flux over a control surface and over time yields the total transported sediment mass:

$$F = \int_{t_0}^{t_1} \int_{A} \mathbf{J} \cdot \mathbf{n}\, dA\, dt \tag{2.2}$$

where, in this research, $\mathbf{J}$ denotes the sediment flux vector [gDM/m^2/s], F is the transported sediment mass [gDM], c is the suspended sediment concentration [gDM/m^3], $\mathbf{u}$ is the flow velocity vector [m/s], A is the control surface [m^2], and $\mathbf{n}$ is the unit normal vector to the control surface.

2.4. Fine sediments in the port

Maintenance dredging in Rotterdam is divided between two authorities: the PoR is responsible for the port basins, while RWS manages the channels and waterways (Rijkswaterstaat 2026). The PoR dredges more than 10 Mm^3/year, consisting primarily of silt from marine and fluvial sources (Vellinga et al. 2005; De Nijs et al. 2010). Clean dredged material is relocated to the Verdiepte Loswal and Loswal Noord West disposal sites, indicated in Figure 2.3, whereas contaminated sediment is disposed of in the Slufter, shown in Figure 2.5 (Vellinga et al. 2005; Kirichek et al. 2018).

Mud accumulation in the port concentrates in the sheltered, low-energy areas of the system, where currents are weak and turbulent mixing is limited. Fluid mud therefore occurs mainly near the coastal basins, including the Calandkanaal, Beerkanaal, Westbocht, and 8th Petroleumhaven, as well as near quay walls and in sediment traps (Van Keulen et al. 2025). In contrast, the Rotterdam Waterway is characterized by a predominantly sandy bed, because its more energetic conditions limit persistent mud deposition (De Nijs et al. 2009).

Salinity-induced density circulation associated with the salt wedge is an important driver of fine sediment accumulation in the basins. The salt wedge oscillates tidally between the Rotterdam Waterway and, at maximum landward extent, the Botlek harbour (De Nijs et al. 2009). Near the salt-wedge tip, density stratification at the pycnocline suppresses vertical mixing, promoting SPM trapping and the formation of an Estuarine Turbidity Maximum (ETM) (Geyer 1993; De Nijs et al. 2011). This ETM is advected landward during flood and retreats seaward during ebb, controlling the supply of fine sediment available for exchange with harbour basins (De Nijs et al. 2012). Multiple stable ETMs may develop at respective saltwater intrusion heads.

This density-driven exchange drives high siltation rates in basins such as MV2, Calandkanaal, and Botlek harbour (De Nijs et al. 2012). During flood, a lock-exchange mechanism can develop at basin entrances, whereby dense saline water with elevated SPM intrudes through the lower water column while fresher water exits through the upper layer. Once inside the basin, weak currents and suppressed mixing strongly favour deposition; in the Botlek harbour, this yields a siltation efficiency approaching 100% (De Nijs et al. 2009).

2.5. Synthesis

Fine sediment dynamics are governed by a range of interacting processes, of which erosion and deposition are most relevant for analysing sediment release and siltation. Erosion is controlled by bed shear stress relative to the critical threshold, while deposition depends on SPM availability and settling velocity. The latter is difficult to constrain, as fine sediments encompass a wide range of particle sizes up to 63 μm and flocculation causes particles to aggregate into flocs with a dynamic effective settling velocity (Partheniades 2009).

Sediment availability adds a further layer of complexity, as it is highly variable in both space and time. Offshore SPM concentrations are generally higher close to the coast and increase substantially during and after storm events (Verlaan et al. 2000; Van Der Hout et al. 2015). A similar spatial variability is observed in seabed fines content, though the area where SPE-induced scour is expected to develop is generally characterised by low fines content, typically less than 1% (Berkenbosch et al. 2006; Hendriks et al. 2020; Kroon et al. 2025).

SPE-induced changes in fine sediment dynamics are expected to propagate into the port primarily through the near-bed layer at the Maasmond, where the salt wedge drives landward transport of marine fines and links offshore sediment availability offshore to accumulation within the port (De Nijs et al. 2012). Given this complexity, assessing the impact of the SPE requires a consistent modelling approach focused on quantifiable metrics, enabling systematic evaluation of changes in hydrodynamics, sediment transport, and accumulation potential across design alternatives.

3
Methodology

This chapter presents the methodology used in this research. It describes the numerical model set-up used to simulate hydrodynamics and fine sediment transport for the Reference scenario and the SPE design alternatives. Section 3.1 introduces the modelling framework, Section 3.2 describes the model configuration, and Section 3.3 evaluates the Reference simulation against PoR data.

Figure 3.1 translates the conceptual framework shown in Figure 2.1 into the methodological structure of this research. After the model set-up and validation, Section 3.4 defines the research approach for the three analysis domains: the offshore zone, transport through the Maasmond, and the port. These domains are analysed using the same model simulations, but differ in their dominant processes, output variables, and spatial scales.

Each results chapter follows the same structure. The Reference scenario is first analysed to establish the baseline model behaviour within the domain. The SPE designs are then compared against this baseline to identify changes in hydrodynamics or fine sediment dynamics. Finally, the results are synthesised for that domain. Because the analysis follows the sediment pathway from offshore to the port, each domain synthesis supports the interpretation of the next.

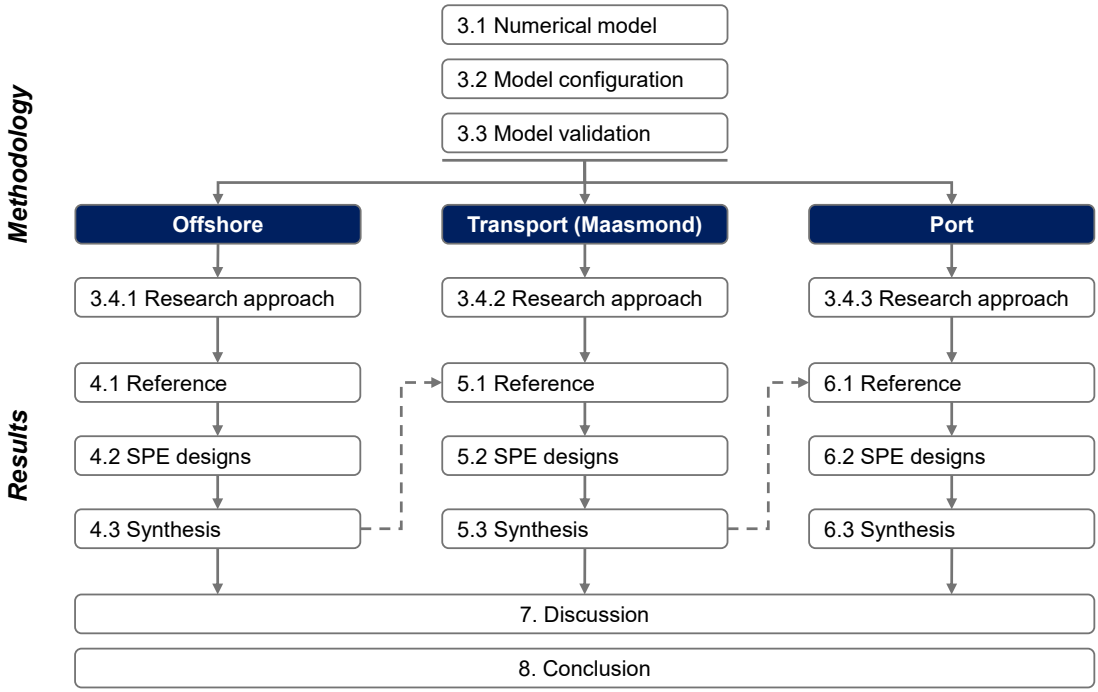

Figure 3.1: Overview of the methodological structure and corresponding results chapters, linking the numerical model set-up to the offshore, Maasmond transport, and port analyses, which are subsequently synthesised in the discussion and conclusion.

3.1. Numerical model

The modelling sequence consists of a hydrodynamic simulation, followed by a fine sediment transport simulation using the resulting flow fields as input. The model set-up focuses on fine sediment transport and excludes morphodynamic feedback on bed levels, consistent with the scope defined in Section 1.4. The model scenarios differ solely in the used bathymetry, representing the different SPE geometries. The full modelling sequence is shown in Figure 3.2.

The OSR-NSC model (*Operationeel Stromingsmodel Rijnmond-Noordzeekust*) is used to simulate hydrodynamic conditions in the greater Port of Rotterdam and adjacent coastal zone. These hydrodynamics form the basis for the fine sediment transport simulations. The NSC grid extends 15–20 km offshore and includes the Rhine-Meuse estuarine system up to Krimpen aan de Lek, the Beneden Merwede, Dordtsche Kil, and the Spui (Kranenburg 2015a). Hydrodynamic boundary conditions are obtained from Deltares. The OSR-NSC model has been applied and validated in previous studies of the Port of Rotterdam, including within the PRISMA research programme, where the modelling framework was used to analyse sediment import driven by advection, settling, and bed exchange processes (Kranenburg 2015a; Kranenburg 2015b; Van Keulen et al. 2025).

Hydrodynamics are simulated using the Delft3D-FLOW module, a three-dimensional process-based model that solves the non-linear shallow water equations derived from the Navier–-Stokes equations for incompressible free-surface flow (Deltares 2025b). The model resolves key coastal and estuarine processes, including tidal propagation, wind-driven circulation, and density-driven flow resulting from salinity and temperature gradients (Deltares 2025b). Through online coupling with Delft3D-WAVE (i.e. simultaneous two-way interaction within a single simulation), wave–-current interactions are resolved, enabling consistent representation of wave-induced forces, flow velocities, water levels, and turbulence characteristics relevant for sediment transport (Deltares 2025b).

Fine sediment transport is simulated using DELWAQ, a multi-dimensional water quality model that solves the advection–diffusion–reaction equation for transported substances. In the model, fine sediment is represented as Inorganic Matter (IM) fractions (Deltares 2025a). DELWAQ is one-way coupled to Delft3D-FLOW, which provides the flow field, including velocities, water levels, density, vertical eddy viscosity, and vertical eddy diffusivity, used to compute the transport and redistribution of fine sediment (Deltares 2025a). The DELWAQ model includes the sediment buffer formulation developed by Van Kessel et al. (2010), which represents temporary storage of fine sediment in the bed and accounts for remobilisation of previously deposited material under changing hydrodynamic conditions (Van Kessel et al. 2010; Van Keulen et al. 2025).

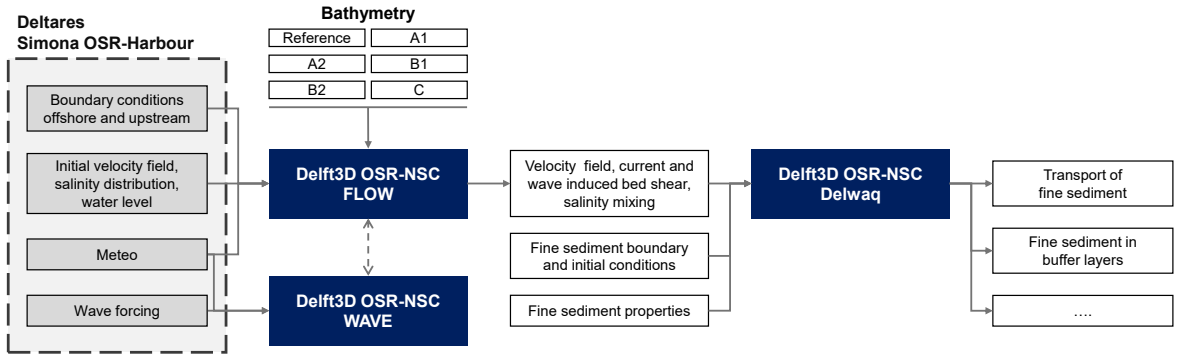

Figure 3.2: Overview of the modelling approach. Hydrodynamics are simulated with the coupled Delft3D OSR-NSC FLOW–WAVE model. The resulting flow field is used in DELWAQ to simulate fine sediment transport. SPE alternatives are represented through bathymetric modifications.

Buffer model

In DELWAQ, the seabed is conceptualised as a temporary storage reservoir for fine suspended sediment, developed by Van Kessel et al. (2010). The seabed is schematised as a two-layer system as depicted in Figure 3.3, consisting of a thin upper fluff layer (S_1) and an underlying sandy buffer layer (S_2).

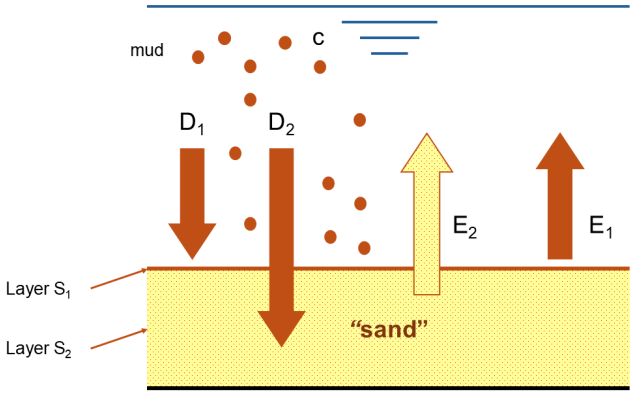

Figure 3.3: Schematisation of the buffer-layer model in DELWAQ (Van Kessel et al. 2010).

The upper layer S_1 represents recently deposited, weakly consolidated fine sediment. This mobile material typically accumulates locally in the troughs of small-scale bedforms, such as sand ripples and sand waves, and in sheltered port basins. As a result, the sediment in this layer is readily available for exchange with the water column and responds rapidly to changes in hydrodynamic forcing. The second layer S_2 represents a sandy seabed containing fine sediment within the pore space of the bed. Exchange with the water column is more limited, but the storage capacity of this layer is significantly larger. Fine sediment stored in the sandy bed layer can remain present for extended periods (Van Kessel et al. 2010).

Exchange of sediment between the water column and the bed layers is governed by deposition and resuspension fluxes. Deposition from the water column depends on the settling velocity (w_s) and the near-bed suspended sediment concentration (c):

$$D_1 = (1-\alpha) w_s c \tag{3.1}$$

$$D_2 = \alpha w_s c \tag{3.2}$$

The parameter α determines the fraction of deposited sediment that infiltrates into the sandy buffer layer S_2. As the fraction of fines in the sandy matrix approaches saturation, the infiltration capacity decreases and deposition increasingly contributes to the fluff layer ($\alpha \to 0$). Resuspension from the bed layers depends on the excess bed shear stress:

$$E_1 = m_1 M_1 \left(\frac{\tau}{\tau_{cr,S1}} - 1 \right) \tag{3.3}$$

$$E_2 = p_2 M_2 \left(\frac{\tau}{\tau_{cr,S2}} - 1 \right)^{1.5} \tag{3.4}$$

Resuspension from the fluff layer S_1 follows a first-order formulation, scaling linearly with the available sediment mass per unit area m_1. Because the sediment in this layer is weakly consolidated, mobilisation occurs relatively easily when the bed shear stress exceeds the critical threshold $\tau_{cr,S1}$. The critical shear stress for the sandy buffer layer is higher ($\tau_{cr,S2} > \tau_{cr,S1}$), reflecting the stronger resistance to erosion of fines embedded within the sandy bed matrix. Consequently, significant mobilisation of fines from S_2 typically occurs only during energetic conditions such as spring tides or storm events.

The resuspension formulation for the fluff layer S_1 deviates from the classical Partheniades erosion law by introducing a first-order dependency on the sediment mass per unit area m_1. The Partheniades formulation assumes erosion of a fully cohesive mud bed, resulting in a zero-order erosion rate that is independent of the amount of sediment present. However, along the Dutch coast, the fluff layer is unlikely to form a continuous cohesive bed, but instead accumulates locally in the troughs of sand ripples and sand waves. Under these conditions, the availability of erodible sediment varies spatially and temporally, and the erosion rate is therefore expected to scale with the locally available sediment mass. Introducing the parameter m_1 transforms the zero-order Partheniades formulation into a first-order erosion relation, allowing the resuspension flux to scale linearly with the amount of sediment present in the fluff layer (Van Kessel et al. 2010).

An additional advantage of the first-order erosion formulation is that sediment fractions originating from different sources can be treated independently, enabling linear scalability of sediment transport simulations. This allows the dispersion of individual sediment sources to be analysed without requiring explicit representation of background concentration levels, while still maintaining a physically consistent representation of sediment availability in the bed (Van Kessel et al. 2010).

3.2. Model configuration

This section describes the configuration of Delft3D-FLOW and DELWAQ used to simulate hydrodynamics and fine sediment transport. The hydrodynamic model set-up is described in Subsection 3.2.1, while the DELWAQ fine sediment transport set-up is described in Subsection 3.2.2. Both Delft3D-FLOW and DELWAQ use the same computational grid, corresponding to the OSR-NSC model domain shown in red in Figure 3.4. This domain is nested within the larger OSR-Harbour domain, shown in blue. Figure 3.5 shows the bathymetry of the OSR-NSC model domain.

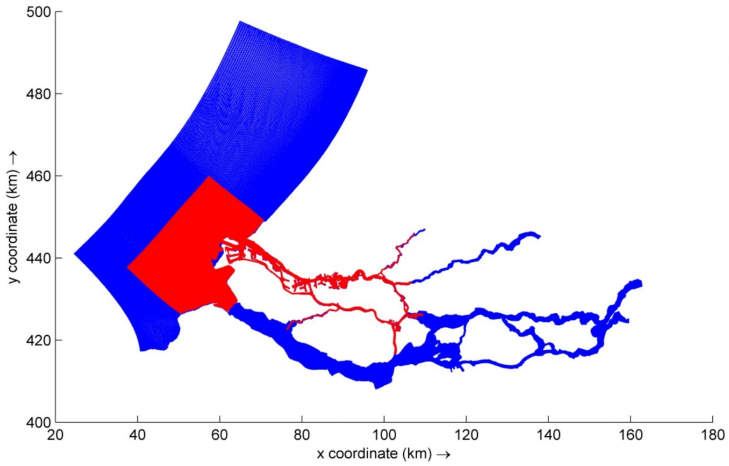

Figure 3.4: Computational grids of the OSR modelling system. Blue: OSR-Harbour grid. Red: nested OSR-NSC grid. Image retrieved from Kranenburg (2015a).

σ-layer	Thickness
1	12%
2	12%
3	11%
4	11%
5	11%
6	11%
7	11%
8	9%
9	6%
10	6%

Table 3.1: Relative thickness distribution of the σ-layers in the OSR-NSC model, ordered from surface to bed (Kranenburg 2015a).

The horizontal grid resolution ranges from approximately $200\ \mathrm{m} \times 400\ \mathrm{m}$ in the offshore region, to $20\ \mathrm{m} \times 20\ \mathrm{m}$ in the port basins. This provides sufficient spatial detail to resolve the local effects of the SPE designs. Vertically, the OSR-NSC model applies 10 σ-layers with non-equidistant thickness, as listed in Table 3.1. Layer thickness decreases towards the bed ($\sigma = 10$), increasing vertical resolution in the near-bed region where velocity gradients, turbulence production, and sediment exchange processes are strongest (Kranenburg 2015a).

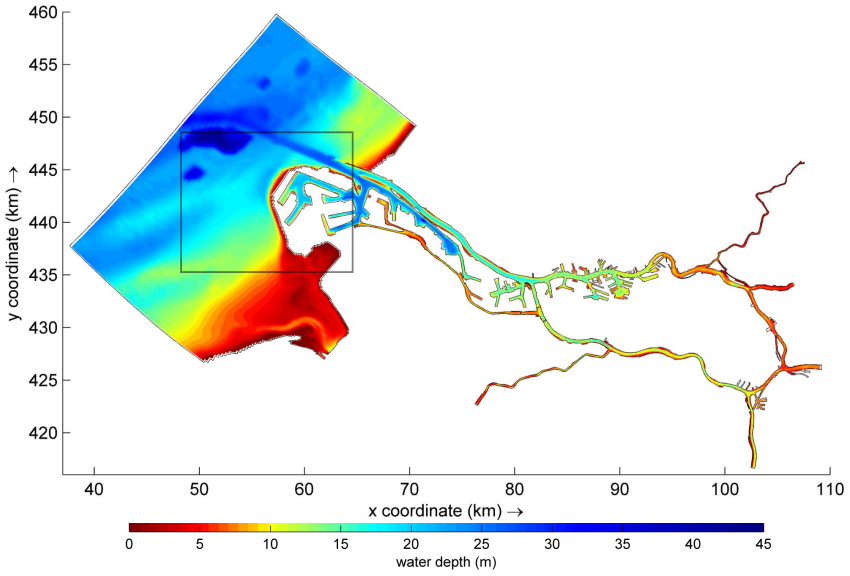

Figure 3.5: Reference bathymetry of the OSR-NSC grid. The black box indicates the area of bathymetric modification for the SPE designs.

3.2.1. Delft3D-FLOW

This subsection describes the Delft3D-FLOW and WAVE model settings relevant to this study. A complete overview of all model settings is provided in Appendix A.

Model physics and numerical settings

The Delft3D-FLOW configuration includes wind forcing, wave forcing, and salinity-driven density effects. Bottom friction is represented using a spatially varying Manning roughness formulation retrieved from PRISMA, while turbulence is resolved with the κ–ϵ second-order closure model. Initial hydrodynamic conditions are obtained from a spin-up simulation covering one full spring–neap cycle, after which the final model state is used to initialise the representative-cycle simulation. The Delft3D-FLOW time step is set to $dt = 3\ \mathrm{s}$, which is comparable to previous applications within PRISMA ($dt = 6\ \mathrm{s}$) and Kranenburg (2015a) ($dt = 7.5\ \mathrm{s}$). This relatively small time step supports numerical stability in the Delft3D simulations and was selected because larger time steps exceeded the practical limits of the computational set-up. The coupling interval between Delft3D-FLOW and Delft3D-WAVE is set to $30\ \mathrm{min}$.

Forcing

Hydrodynamic boundary conditions are obtained from a SIMONA OSR-Harbour simulation used in PRISMA, covering the period 01-05-2024 00:00:00 to 01-08-2024 00:00:00. At the offshore open boundaries, Riemann time series are prescribed for flow velocity, while river boundaries are defined using discharge time series.

From this dataset, a representative 14.5-day spring–neap cycle is selected to provide consistent hydrodynamic forcing. This ensures that differences between scenarios can be attributed to the SPE configurations rather than to variations in the imposed forcing. The selected window is intended to represent regular conditions and therefore excludes high-energy events such as storms. To ensure continuity when repeating the cycle, the start and end of the period are selected to minimise discontinuities in water level and flow velocity. A Python-based analysis is used to identify a period that minimises discontinuities between the start and end points while representing regular hydrodynamic conditions (Appendix B). This results in the selected window from 02-05-2024 01:00:00 to 16-05-2024 13:00:00. The time-frame selection is illustrated in Figure 3.6.

The selected spring–neap cycle is characterised by moderate conditions, with an average wind speed at Hoek van Holland of approximately $5\ \mathrm{m/s}$ (applied uniformly over the domain), significant wave heights ranging from $0.2\ \mathrm{m}$ to $2.24\ \mathrm{m}$, a tidal amplitude of approximately $1.20\ \mathrm{m}$, and an average Rhine discharge at Lobith of $2500\ \mathrm{m^3/s}$.

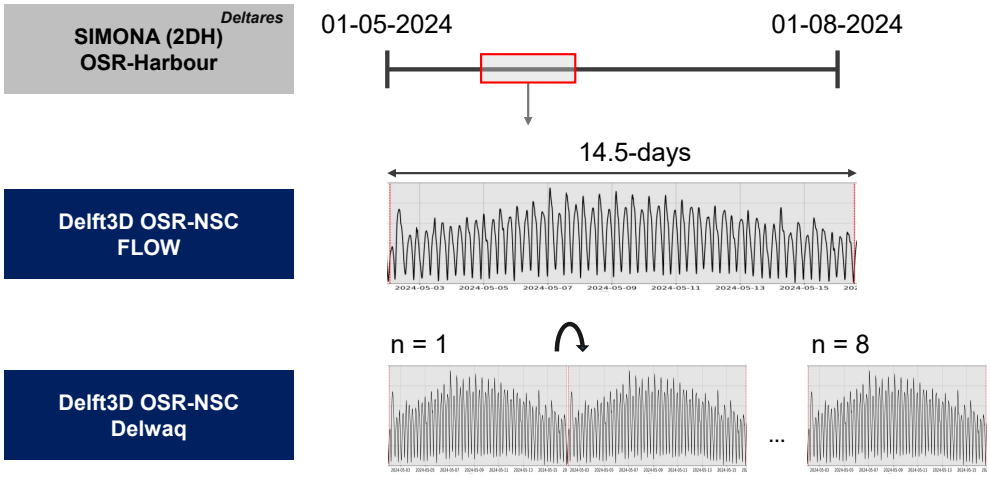

Figure 3.6: Schematization of the selected simulation period and repeated spring–neap forcing cycle. The upper panel shows the boundary forcing retrieved from SIMONA OSR-Harbour used in Delft3D-FLOW, representing a 14.5-day spring–neap cycle. This cycle is repeated to simulate eight consecutive spring–neap cycles in DELWAQ.

3.2.2. DELWAQ

This subsection summarises the key DELWAQ model settings applied in this study. A complete overview of model parameters is provided in Appendix A.

Substances and buffer model

Fine sediment is represented in DELWAQ using three Inorganic Matter (IM) fractions. These fractions are selected to represent different fine sediment characteristics, ranging from slowly settling clay to faster-settling silt and micro floc. Each fraction is distinguished by its prescribed settling velocity w_s, as shown in Table 3.2. IM1 represents clay, IM2 fine silt, and IM3 coarse silt or micro floc (Mariotti et al. 2025; Kirichek et al. 2021; Zijl et al. 2021). The settling velocity of the fractions can be determined through the diameter of individual particles or to the floc diameter, as applied by Kirichek et al. (2021). The two-layer buffer schematisation described in Section 3.1 is applied, with critical shear stresses of $\tau_{cr,S1} = 0.2\ \mathrm{N/m^2}$ for the fluff layer (S_1) and $\tau_{cr,S2} = 0.8\ \mathrm{N/m^2}$ for the sandy buffer layer (S_2).

In this model set-up, flocculation is represented implicitly through the assigned w_s for IM3. However, the IM fractions are modelled as separate sediment classes, meaning that no interplay occurs between fractions and that aggregation and break-up processes are not dynamically resolved.

Fraction	w_s [m/day]	Class	B.C. [gDM/m^3]	IC:susp. [gDM/m^3]	IC: S_1 [gDM/m^3]	IC: S_2 [gDM/m^3]
IM1	0.1	Clay	1	0	1	1
IM2	10.8	Fine silt	5	0	5	5
IM3	86.4	Coarse silt/micro floc	20	0	20	20

Table 3.2: DELWAQ settings for the Inorganic Matter (IM) fractions, including settling velocity (w_s), sediment classification, constant boundary conditions (B.C.), and initial conditions (IC) in suspension, Layer S_1, and Layer S_2.

Boundary conditions

Constant boundary concentrations are prescribed, as spatially and temporally resolved fine sediment forcing data are unavailable. Van Kessel et al. (2010) showed that the first-order resuspension formulation used in the DELWAQ Buffer module results in linear SPM transport behaviour in the model. Under this assumption, sediment fractions and sources act independently and their contributions can be superimposed without altering transport dynamics. Because hydrodynamic forcing is identical for all simulations and only bathymetry differs between scenarios, differences in model results can be attributed to bathymetry-induced changes in hydrodynamic conditions such as flow velocity. Due to the use of constant boundary concentrations, SPM concentrations and sediment fluxes are not interpreted in absolute terms, but comparatively in a relative (semi-quantitative) sense.

No empirical information is available on the relative abundance of the three IM fractions, and representing the full spectrum of natural fine sediments using only three fractions constitutes a simplification. Therefore, Total Inorganic Matter (TIM = IM1 + IM2 + IM3) is not interpreted quantitatively, and the analysis focuses on relative changes within the individual fractions.

Initial conditions and time-frame

The objective of this study is to assess short-term differences between the Reference and Design scenarios, rather than absolute equilibrium concentrations. Long simulations would allow the system to adjust to the modified bathymetry, thereby reducing the contrast in initial fine sediment mobilisation between scenarios.

To preserve sensitivity to the initial system response to bathymetric changes, the simulation period is limited and no extended spin-up is applied. Eight spring–neap cycles are simulated, providing sufficient time for sediment redistribution while maintaining focus on short-term system adjustments. The first two cycles are treated as spin-up time for DELWAQ and excluded from the analysis. This spin-up period allows the initially prescribed fine sediment to disperse through the model domain. The DELWAQ simulation runs from 02-05-2024 01:00:00 to 26-08-2024 01:00:00. The analysis period starts on 31-05-2024 01:00:00, after a spin-up period of two spring–neap cycles, and is denoted as t_0. The analysis period ends on 26-08-2024 01:00:00, denoted as t_1. A time step of 30 minutes is applied in DELWAQ.

3.2.3. Simulation scenarios

The model sequence is applied to the Reference scenario and the design alternatives (A1, A2, B1, B2, C), with bathymetry as the only varying parameter. The bathymetry of the Maasvlakte 2 area for each scenario is shown in Figure 3.7. The Reference bathymetry was obtained from the Port of Rotterdam.

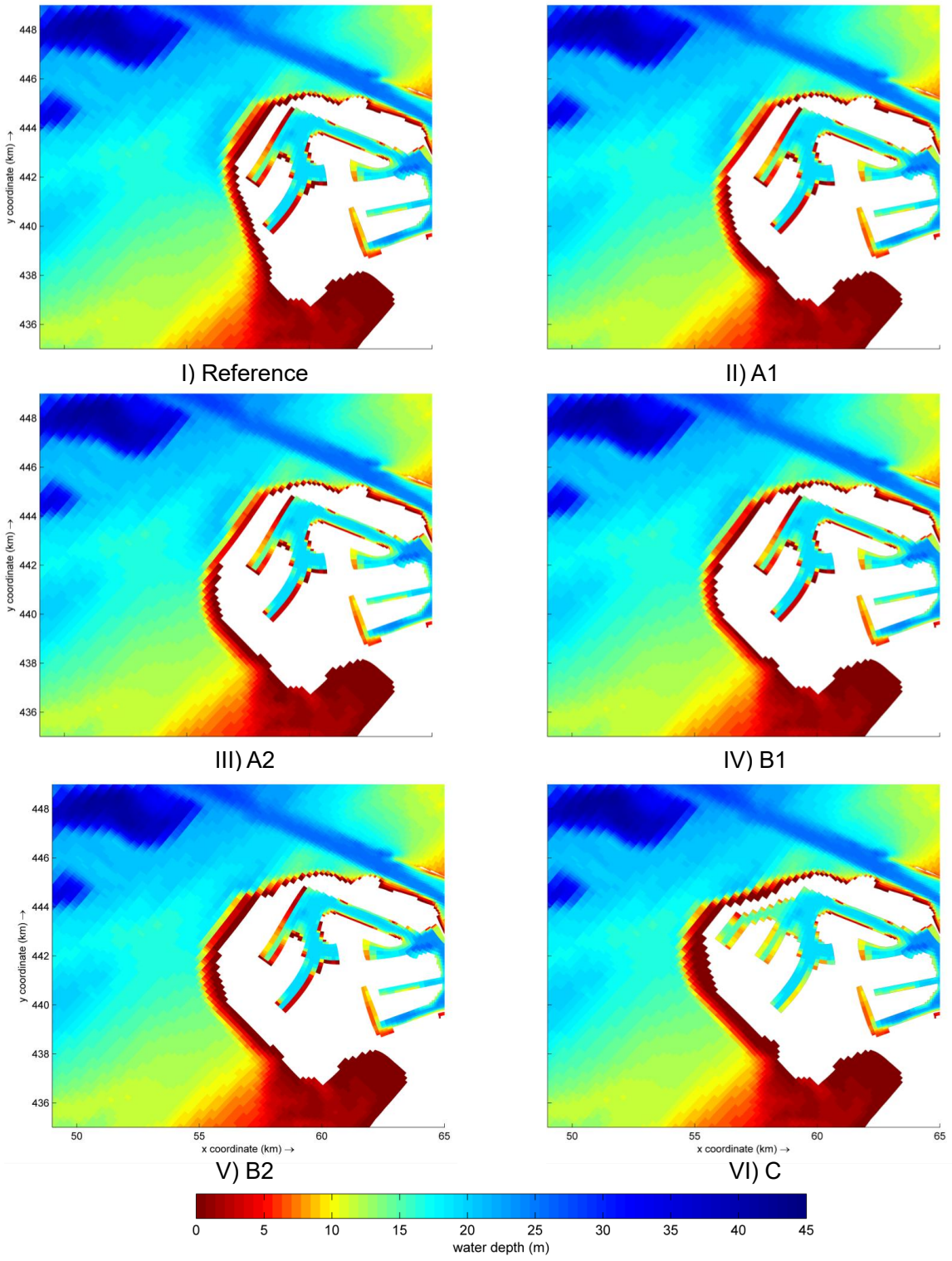

Figure 3.7: Bathymetry of the MV2 area for the Reference scenario and SPE design alternatives A1, A2, B1, B2, and C. The bathymetry data were retrieved from the Port of Rotterdam (2025).

3.3. Model validation

This section evaluates whether the hydrodynamic model set-up provides a suitable basis for comparing the Reference and Design scenarios. The DELWAQ Reference simulation itself cannot be validated directly, because constant boundary conditions are used. Instead, the Reference DELWAQ simulation is used to verify the linear response of the DELWAQ Buffer module.

Delft3D-FLOW results are validated against Hydrometeo observations at Hoek van Holland, Vlaardingen, and Lekhaven. The full validation results are provided in Appendix B, while the water-level and salinity validation at Hoek van Holland is shown in Figures 3.8a and Figure 3.8b. Water levels and salinity agree well with the observations in terms of tidal phase and amplitude. Salinity variability is also reproduced well, although salinity is slightly overestimated in the lower water column, which is a known model limitation (Kranenburg 2015b). Overall, the hydrodynamic conditions are represented with sufficient accuracy for scenario comparison, and no additional calibration is required.

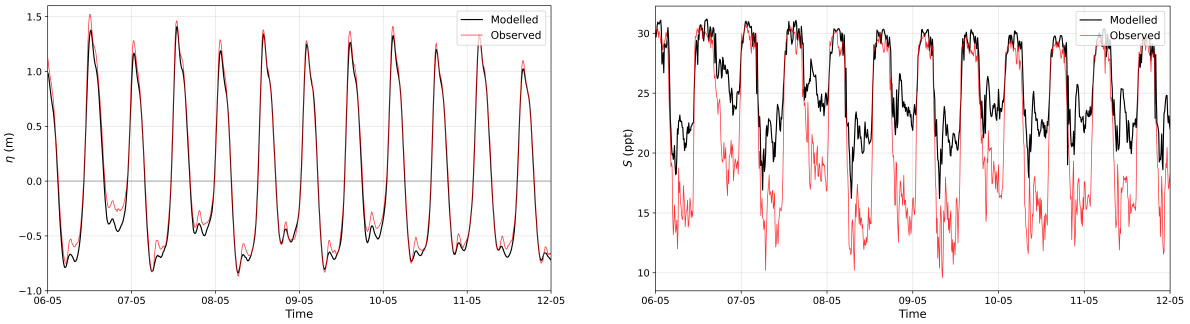

(a) Water level (η) at Hoek van Holland

(b) Near-bed salinity (S) at Hoek van Holland

Figure 3.8: Validation of the Delft3D-FLOW Reference simulation against observed Hydrometeo data obtained from the PoR.

As discussed in Section 3.2.2, the analysis assumes linear scaling of SPM within the DELWAQ Buffer module. This assumption was tested using three simulations with constant imposed boundary concentrations. The response of all IM fractions was evaluated at three observation points: offshore, nearshore, and inside the port basin. The analysis considered both water-column concentrations and mass development in bed layers S_1 and S_2. The upper panel of Figure 3.9 shows the response of fraction IM3 at an offshore observation point. After normalisation by the imposed boundary concentration, the time series collapse onto a single curve in the lower panel, demonstrating a linear scaling of the model response. This scaling behaviour was consistent across all IM fractions, observation points, and evaluated variables. Relative differences between scenarios can therefore be interpreted independently of the absolute magnitude of the prescribed boundary forcing.

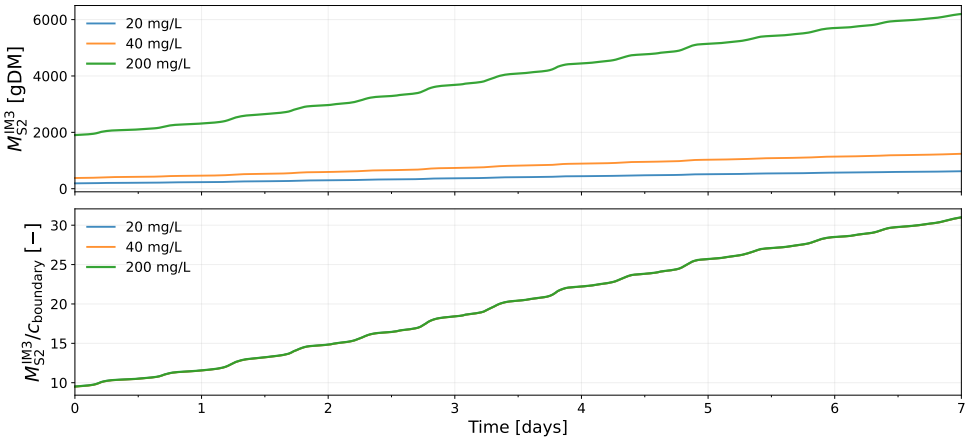

Figure 3.9: Temporal development of the IM3 mass in Layer S_2 ($M_{S2}(t)$) at an offshore observation point located approximately 7 km offshore of MV2. Results are shown for boundary concentrations of 20 mg/L, 40 mg/L, and 200 mg/L. The upper panel shows the absolute IM3 mass, while the lower panel shows the mass normalised by the corresponding boundary concentration.

3.4. Research approach

This section presents the domain-specific methods used to analyse the model results within the framework shown in Figure 3.1. The analysis is structured around three domains: the offshore zone, transport through the Maasmond, and accumulation within the port, addressed in Subsections 3.4.1, 3.4.2, and 3.4.3, respectively.

Before introducing these domain-specific methods, the key implications of the model configuration and research approach are summarised. These implications define the interpretative boundaries of the study and establish the basis on which model results should be evaluated.

1. This study provides a first-order, exploratory analysis of the system response to the SPE design alternatives. As no prior work exists on fine sediment dynamics for these designs, the results cannot be directly validated against existing studies. The analysis constitutes an initial application of this modelling set-up to assess the potential impact of the SPE design alternatives on hydrodynamics and fine sediment dynamics. Results are interpreted in a semi-quantitative sense, with emphasis on spatial patterns, relative differences between alternatives, and the general system response, rather than on deterministic predictions of sediment transport, sedimentation, or scour development.
2. The model set-up excludes morphodynamic feedback. Fine sediment deposition and erosion therefore do not update the bed level during the simulation, and bathymetric changes resulting from sediment redistribution are not coupled back to the hydrodynamic or sediment-transport calculations. Furthermore, the IM fractions behave independently within the DELWAQ simulation, each being transported, deposited, and resuspended without interaction between fractions or competition for bed storage capacity. Consequently, co-located deposition of multiple fractions can occur without modifying the local bed composition. Together, these constitute simplifications of natural sediment–bed interaction.
3. Constant fine sediment boundary concentrations are prescribed to focus the analysis on relative differences in fine sediment behaviour between scenarios. Since the DELWAQ Buffer module exhibits a linear response to the imposed boundary concentration, suspended sediment concentrations and bed layer masses can be compared between the Reference scenario and the SPE designs. Scenario responses are evaluated as relative differences (ΔX) with respect to the Reference scenario, forming the basis for the comparative assessment of the SPE design alternatives.
4. Model-derived quantities extracted at selected observation points and within predefined spatial domains are used to compare the Reference scenario and the SPE design alternatives. Each observation point is assumed to be representative of the local response of its surrounding area and is used to characterise regional differences between scenarios. This approach reduces spatially and temporally variable model output to a set of comparable metrics.
5. Mass of fine sediment in bed layers S_1 and S_2 at the end of the simulation ($M_{S1}(t_1)$, $M_{S2}(t_1)$) serve as an initial visual diagnostic of the bed mass response to the modified bathymetries. Differences to the Reference scenario indicate how each SPE geometry affects fine sediment storage across the bed layers. These quantities provide a compact, first-order representation of spatial redistribution over the simulation period and are used throughout the research to identify dominant accumulation and erosion patterns.

3.4.1. Offshore

The objective of the offshore analysis is to assess how the SPE design alternatives modify hydrodynamics, fine sediment redistribution, and scour-area development in the offshore domain, addressing research sub-questions 1 and 2. The construction of an SPE alters the local flow field, which increases bed shear stress near the structure and promotes scour development. This affects the mobilisation, deposition, and redistribution of fine sediment.

To isolate and quantify the offshore response, the analysis is structured around three components. First, the hydrodynamic response is evaluated to identify changes in offshore forcing and flow patterns. Second, the redistribution analysis evaluates whether these hydrodynamic changes result in offshore source and sink patterns. Third, the scour-area analysis quantifies the potential fine sediment release associated with newly induced erosion around the designs. Table 3.3 summarises the variables and diagnostics used for each component, which are subsequently discussed in detail.

Table 3.3: Variables used to analyse the offshore response of the SPE design alternatives, with the diagnostic basis indicating whether the analysis uses spatial model fields or observation-point time series.

Analysis component	Variables	Diagnostic basis
1) Hydrodynamic response	$\overline{u}$, τ_b	Spatial fields
2) Fine sediment redistribution	ΔM_{bed}, $\overline{\tau}_b$, $\overline{c}_{IMi}$	Observation points
3) Scour-area development	$A_{\mathrm{SPE,new}}$, R_A, $\overline{R}_A$, $\Delta E_{\mathrm{fines,SPE}}$	Spatial fields

1. **Hydrodynamic response**: changes in depth-averaged flow velocity ($\overline{u}$) and bed shear stress (τ_b) are evaluated to determine how the SPE design alternatives modify the offshore flow field.
2. **Fine sediment redistribution**: changes in net bed mass development (ΔM_{bed}), bed shear stress ($\overline{\tau}_b$), and suspended sediment concentration ($\overline{c}_{IMi}$) are used to identify and quantify source and sink areas.
3. **Scour-area development**: the SPE-induced increase in potential scour area is derived from the bed shear stress fields. These estimates are compared with scour-area projections from SVASEK to assess consistency between the two approaches. The SVASEK-projected increase in scour volume is then used to estimate the additional fine sediment release from the SPE-induced scour area ($\Delta E_{\mathrm{fines,SPE}}$).

1) Hydrodynamic response

The hydrodynamic response provides the basis for interpreting offshore fine sediment dynamics. SPE-induced changes in sediment transport towards the Maasmond may occur through two mechanisms: increased bed shear stress can enhance fine sediment mobilisation, while changes in the flow field can modify transport pathways and transport magnitude.

The depth-averaged velocity field ($\overline{u}$) and bed shear stress field (τ_b) are evaluated during peak flood and peak ebb for the Reference scenario and design alternatives. These tidal phases represent high-forcing conditions in both transport directions and are used to identify the main SPE-induced changes in flow behaviour and sediment mobilisation potential.

This approach is subject to three main limitations. First, peak flood and peak ebb represent high-forcing hydrodynamic conditions, but do not resolve variability over the full tidal cycle. Second, $\overline{u}$ provides a first-order visualisation of horizontal transport pathways, but does not capture vertical variations in u or stratification effects. Third, τ_b is used to assess sediment mobilisation potential, while the frequency, duration, and magnitude of exceedance relative to τ_{cr} are not explicitly quantified. Despite these limitations, the combined analysis of $\overline{u}$ and τ_b provides a robust first-order assessment of the SPE-induced hydrodynamic response.

2) Fine sediment redistribution
This analysis assesses how fine sediment is redistributed across the offshore domain and identifies potential source and sink areas. Based on the initial DELWAQ results, nine observation points were selected in areas where clear changes in mass in layer S_2 (M_{S2}) occur relative to the Reference scenario (Figure 3.10). For each observation point and IM fraction, the net bed mass change over the analysis period (ΔM_{bed}) is computed.

To interpret the drivers of these bed mass changes, $\overline{\tau}_b$ is used as a proxy for erosion potential, while $\overline{c}_{IMi}$ is used as a proxy for sediment availability and deposition. Relative differences in ΔM_{bed}, $\overline{\tau}_b$, and $\overline{c}_{IMi}$ between the SPE designs and the Reference scenario are used to identify and quantify the offshore redistribution patterns. These patterns provide the basis for assessing whether offshore redistribution affects fine sediment intake through the Maasmond, as well as the mechanisms through which this occurs.

The same observation-point approach is used in the port accumulation analysis (Section 3.4.3), where the computation of these variables and the associated assumptions are described in more detail.

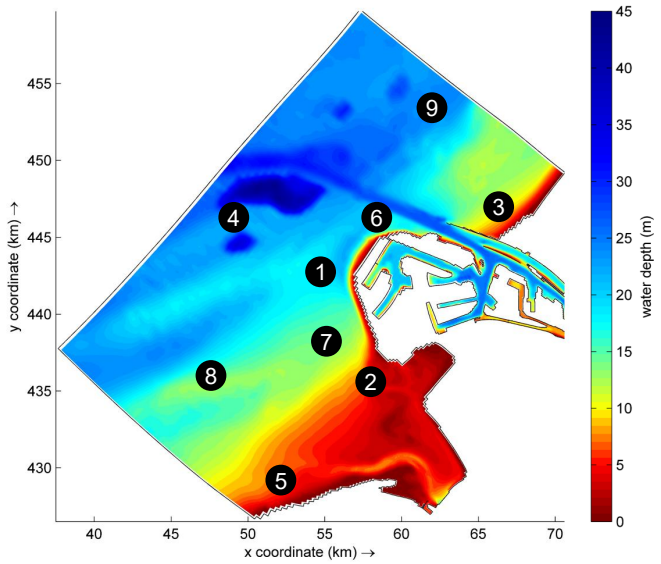

Obs. point	Location
1	Scour area
2	MV2 south
3	Hoek van Holland
4	Offshore western boundary
5	Ouddorp
6	MV2 north
7	MV2 southwest
8	Offshore southern boundary
9	Offshore northern boundary

Figure 3.10: Offshore bathymetry of the Reference scenario, with observation points indicated in the offshore domain. The accompanying table describes the corresponding observation point locations.

3) Scour-area development
This analysis estimates the SPE-induced increase in potential scour area around MV2 and the associated fine sediment release to the system. As discussed in Section 2.2, SVASEK used FINEL2D to project erosion-pit development for the different SPE layouts. These projections, summarised in Table 2.1, provide estimates of scour area, maximum scour depth, and scour volume. However, they are subject to substantial uncertainty, with reported ranges of -50% to +200% (Kroon et al. 2025).

The Delft3D-based model set-up used in this study also excludes morphodynamic feedback and therefore cannot directly predict scour depth, scour volume, or development over time. Instead, maximum bed shear stress fields are used to identify areas of elevated scour potential. These areas are interpreted as diagnostic estimates of potential scour extent, rather than as morphologically computed scour areas.

The Delft3D-based estimates of potential scour area are then compared with the SVASEK scour-area projections to assess consistency between the two approaches. If the Delft3D-based estimates show the same order of magnitude and design-scale trend as the SVASEK projections, the SVASEK scour-volume estimates are adopted for the fine sediment release calculation.

Three diagnostic bed shear stress thresholds are applied: $\tau_{b,cr} = 0.8\ \mathrm{N/m^2}$, $1.2\ \mathrm{N/m^2}$, and $1.6\ \mathrm{N/m^2}$. These thresholds are used as indicators of elevated hydrodynamic forcing. For each threshold, the area where $\tau_b > \tau_{b,\mathrm{cr}}$ is identified for both the Reference scenario (A_{Ref}) and each SPE design scenario (A_{SPE}).

To isolate the SPE-induced contribution, the overlap between the Reference and design exceedance areas (A_{overlap}) is excluded. This overlap represents the existing scour area of MV2 and is therefore not attributed to release new fines to the system. The newly induced potential scour area is defined as:

$$A_{\mathrm{SPE,new}}(\tau_{b,\mathrm{cr}}) = A_{\mathrm{SPE}}(\tau_{b,\mathrm{cr}}) - A_{\mathrm{overlap}}(\tau_{b,\mathrm{cr}}) \tag{3.5}$$

The relative increase in potential scour area is then computed as:

$$R_A(\tau_{b,\mathrm{cr}}) = \frac{A_{\mathrm{SPE,new}}(\tau_{b,\mathrm{cr}})}{A_{\mathrm{ref}}(\tau_{b,\mathrm{cr}})} \tag{3.6}$$

To reduce sensitivity to the selected thresholds, the final Delft3D-based estimate of the relative increase in SPE-induced scour area ($\overline{R}_A$) is obtained by averaging R_A over the three diagnostic thresholds:

$$\overline{R}_A = \frac{1}{3} \sum_{\tau_{b,\mathrm{cr}} \in \{0.8,\, 1.2,\, 1.6\}} R_A(\tau_{b,\mathrm{cr}}) \tag{3.7}$$

This estimate is compared with the SVASEK scour-area projections to assess whether both approaches indicate a similar order of magnitude and design-scale trend. Because the Delft3D-based approach does not resolve scour depth or scour volume, the normalised SVASEK scour-volume projections, ΔV, given in Table 2.1, are used in the subsequent fine sediment release calculation.

To translate the projected scour development into a potential fine sediment release, the erosion rate observed for the existing Maasvlakte 2 scour area (E_{MV2}) is used as a reference for the newly induced SPE scour area. The release of fines is then estimated by combining this reference rate with ΔV and the fine sediment content of the eroded volume, C_{fines}. This approach assumes that the existing Maasvlakte 2 scour area and the SPE-induced scour area have comparable bed composition, consolidation state, and hydrodynamic exposure. Under this assumption, the SPE-induced scour area releases fine sediment at the same characteristic fine sediment release rate as the existing Maasvlakte 2 scour pit.

3.4.2. Transport

The Maasmond transect is used as the control section because it captures the exchange of water and fine sediment between the North Sea and the Port of Rotterdam. As described in Section 2.3, SPE-induced changes may affect the sediment flux (J) and the resulting net transported mass (F) through changes in flow velocity, SPM concentration, or their combined effect.

Although F provides the integrated transport response, it does not identify the mechanisms driving that response. Changes may be temporally concentrated during specific hydrodynamic conditions, such as spring tides, or spatially structured across the transect through altered velocity and concentration profiles, including salt-wedge-related effects. The analysis therefore evaluates three components: total transport, temporal variability, and spatial variability.

Table 3.4 summarises the variables used to compare sediment transport through the Maasmond transect between the SPE designs and the Reference scenario. Differences are primarily evaluated as relative differences, ΔX.

Table 3.4: Variables used to compare sediment transport through the Maasmond transect between the SPE designs and the Reference scenario. The diagnostic scale indicates whether the analysis is based on transect-integrated quantities, time series, or grid-cell-level transport.

Analysis component	Variables	Diagnostic scale
1) Total transport	F^{IM}, F^{IM}_{import}, F^{IM}_{export}	Transect-integrated
2) Temporal variability	$u(t)$, $c^{IM}(t)$, $J^{IM}(t)$, $J^{IM}_{\text{GF}}(t)$	Time series
3) Spatial variability	$u_{m,\sigma}$, $c^{IM}_{m,\sigma}$, $F^{IM}_{m,\sigma}$, $\Delta F^{IM,\text{norm}}_{m,\sigma}$	Grid-cell level

Transport formulation and discretisation

In post-processing, Delft3D-FLOW and DELWAQ output are used to compute u, c, J, and F for each grid cell along the Maasmond transect using Python. Figure 3.11 shows the numerical discretisation of the transect and the adopted sign convention.

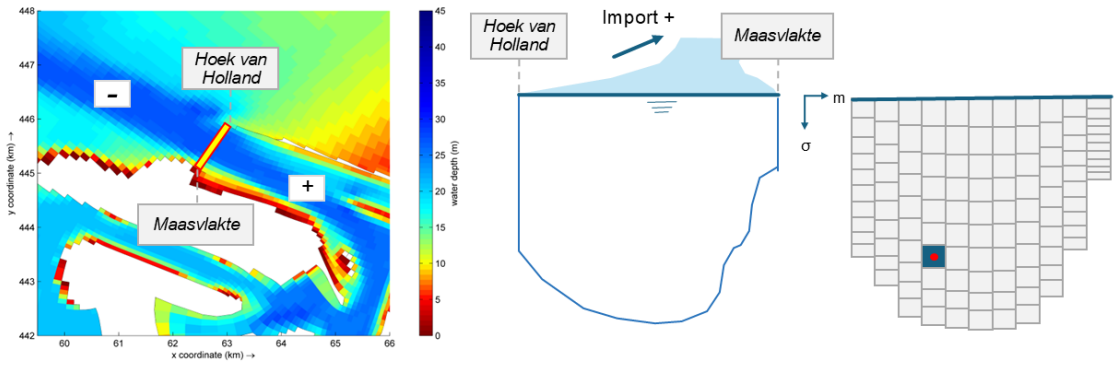

Figure 3.11: Maasmond transect. (a) Plan view of the Maasmond transect within the model domain, including the sign convention for sediment transport, where positive values (+) indicate landward flow into the port (import) and negative values (–) indicate seaward flow out of the port (export). (b) Cross-sectional view of the transect from the North Sea towards the port, with Maasvlakte on the right-hand side and Hoek van Holland on the left-hand side. (c) Schematic representation of the numerical discretisation of the Maasmond transect used for transport calculations.

For each grid cell, the following variables are extracted at the cell centre for each numerical time step t_k, using a temporal resolution of $\Delta t = 30$ min:

- $A_{m,\sigma}(t_k)$ [m^2]: cross-sectional area of the grid cell, defined as the product of the transect segment width, Δm, and the vertical sigma-layer thickness, $\Delta\sigma(t_k)$. The layer thickness varies in time due to changes in free-surface elevation.

- $u^n_{m,\sigma}(t_k)$ $[\mathrm{m/s}]$: horizontal flow velocity component normal to the transect. Delft3D computes velocities at cell faces, whereas the model output used in this analysis provides velocities at the cell centre (Deltares 2025b).
- $c^{IM}_{m,\sigma}(t_k)$ $[\mathrm{gDM/m^3}]$: suspended sediment concentration of fraction IM within the grid cell.

Using these variables, the advective sediment flux per grid cell is computed according to Eq. 3.8. The transported sediment mass per grid cell over the analysis period is obtained by time integration of the flux, implemented as a summation over all time steps (Eq. 3.9).

$$J^{IM}_{m,\sigma}(t_k) = c^{IM}_{m,\sigma}(t_k)\, u^n_{m,\sigma}(t_k)\, A_{m,\sigma}(t_k) \qquad (3.8)$$

$$F^{IM}_{m,\sigma} = \sum_{k=1}^{N} J^{IM}_{m,\sigma}(t_k)\, \Delta t \qquad (3.9)$$

Transport across the full Maasmond transect is obtained by summing over all grid cells in the lateral (m) and vertical (σ) directions, as defined in Eqs. 3.10 and 3.11.

$$J^{IM}(t_k) = \sum_m \sum_\sigma J^{IM}_{m,\sigma}(t_k) \qquad (3.10)$$

$$F^{IM} = \sum_m \sum_\sigma F^{IM}_{m,\sigma} \qquad (3.11)$$

This yields the cumulative suspended sediment transport per sediment fraction through the transect. The transect is treated as a control section, where net sediment exchange is governed by through-flow rather than local storage or vertical exchange processes. Diffusive and dispersive contributions are also neglected, as they are assumed to be secondary for the net exchange across the transect.

The sign convention defined in Figure 3.11 is applied throughout the analysis: positive values represent landward transport into the port, while negative values indicate seaward transport out of the port. Based on this convention, import (J_{import}, F_{import}) and export (J_{export}, F_{export}) are separated at grid-cell level and subsequently aggregated over the transect.

Based on these computed transport quantities, the analysis proceeds in three steps:

1) Total transport
The total transport analysis quantifies cumulative fine sediment exchange through the Maasmond over the analysis period. F_{net} represents the balance between landward import and seaward export. F_{import} and F_{export} are evaluated separately to determine whether changes in the net balance are caused by changes in import, export, or both. Comparing these quantities between the SPE designs and the Reference scenario shows how the designs affect the overall sediment exchange through the Maasmond.

2) Temporal variability
Temporal variability is analysed to assess changes in sediment transport over the spring–neap cycle. This is done using time series of transect-integrated $u(t)$, $c^{IM}(t)$, and $J^{IM}(t)$. To remove high-frequency tidal oscillations, a Godin filter is applied to the flux signal (Eq. 3.12). The Godin filter is a low-pass filter constructed through successive application of two 24-hour and one 25-hour moving averages, effectively removing diurnal and semidiurnal tidal variability (Thompson 1983; Shirahata et al. 2016).

$$J_{\mathrm{GF}}(t) = \mathrm{Godin}\,(J(t)) \qquad (3.12)$$

The filtered signal allows the residual transport response to be compared between the SPE designs and the Reference scenario. Comparing $u(t)$, $c^{IM}(t)$, and $J_{\mathrm{GF}}(t)$ allows transport changes to be attributed primarily to variations in flow velocity, suspended sediment concentration, or their combined effect.

3) Spatial variability
Spatial variability is assessed at the grid-cell level along the Maasmond transect to identify the dominant local contributions to changes in fine sediment transport. The time-integrated transport per grid cell is compared between the SPE designs and the Reference scenario using the normalised transport difference:

$$\Delta F^{IM}_{m,\sigma,\mathrm{norm}} = \frac{F^{IM}_{m,\sigma,\mathrm{design}} - F^{IM}_{m,\sigma,\mathrm{ref}}}{\sum_m \sum_\sigma \left| F^{IM}_{m,\sigma,\mathrm{ref}} \right|} \tag{3.13}$$

Normalisation by the total magnitude of the Reference transport ensures that spatial differences are evaluated relative to the overall transport through the transect. This enables consistent comparison between designs and identifies the lateral and vertical locations where sediment-transport changes occur relative to the Reference scenario.

3.4.3. Port

The objective of this analysis is to assess whether the SPE designs increase fine sediment accumulation in the port relative to the Reference scenario. The analysis focuses on the seaward port basins, primarily the Maasvlakte basins, where marine fine sediment predominantly accumulates (Section 2.4). These basins are expected to show the clearest response to SPE-induced changes in fine sediment transport.

The comparison is based on the net bed mass response (ΔM_{bed}) and its two main process controls: erosion and deposition. Bed shear stress ($\overline{\tau}_b$) is used as a proxy for erosion potential, while suspended sediment concentration ($\overline{c}_{IMi}$) is used as a proxy for sediment availability and potential deposition. Together, these variables are used to determine whether bed mass changes are primarily related to altered erosion conditions, changes in sediment supply, or their combined effect.

Observation points were selected based on preliminary DELWAQ results and in consultation with the PoR dredging department. The selected locations are shown in Figure 3.12. At each point, time series of τ_b, c_{IMi}, mass in layer S_1 (M_{S1}), and mass in layer S_2 (M_{S2}) were extracted at $\Delta t = 30$ min.

The use of discrete observation points assumes that the selected locations are representative of the surrounding basin conditions. This approach may not fully capture local spatial variability, particularly in regions with strong gradients in flow velocity or SPM. Within the port basins, however, generally low flow velocities ($u < 0.5$ m/s) limit advective gradients and support this assumption.

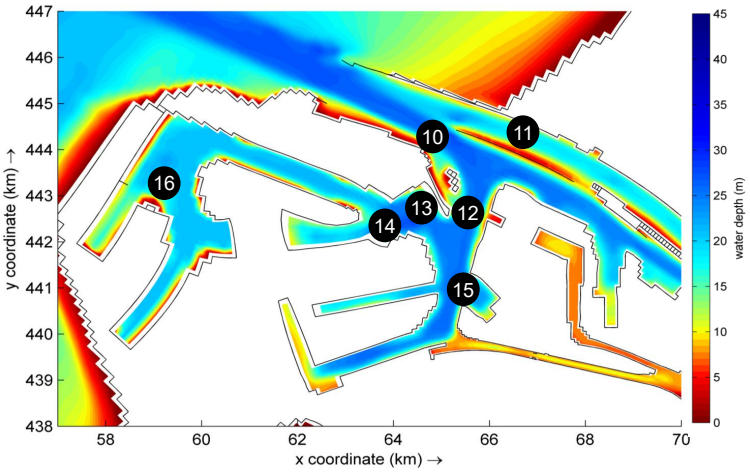

Obs. point	Location
10	Maasmond
11	Nieuwe Waterweg
12	Beerkanaal
13	8th Petroleumhaven
14	Europahaven
15	6th Petroleumhaven
16	Prinses Arianehaven

Figure 3.12: Bathymetry of the Reference scenario, with observation points indicated in the seaward port area. The accompanying table describes the corresponding observation point locations used to assess fine sediment accumulation.

Initial DELWAQ results showed that M_{S1} exhibits strong tidal oscillations, driven by repeated resuspension-deposition cycles as τ_b periodically exceeds $\tau_{cr,S1} = 0.2$ N/m^2. These high-frequency fluctuations can obscure the residual bed mass response, particularly when net bed mass change is evaluated between two individual time instances (t_0, t_1).

To isolate the subtidal evolution of M_{S1}, a Godin filter was applied before combining M_{S1} with M_{S2} in the total bed mass calculation, M_{bed} (Eq. 3.14). This filtering suppresses tidal-frequency variability, allowing net accumulation and erosion patterns to be identified more robustly. Without filtering, the net bed mass change computed between t_0 and t_1 would be sensitive to tidal phase, potentially causing short-term fluctuations in M_{S1} to be misinterpreted as long-term trends.

$$M_{\mathrm{bed}} = M_{S1,GF} + M_{S2} \tag{3.14}$$

Only M_{S1} is filtered; M_{S2} is left unfiltered because the deeper buffer layer responds more gradually and is less sensitive to tidal resuspension due to its higher critical shear stress, $\tau_{cr,S2} = 0.8$ N/m^2. Net bed mass change is then defined as:

$$\Delta M_{\mathrm{bed}} = M_{\mathrm{bed}}(t_1) - M_{\mathrm{bed}}(t_0) \tag{3.15}$$

Filtering the bed mass signal suppresses tidal-scale fluctuations, so ΔM_{bed} represents the residual subtidal bed mass change over the analysis period. This provides a robust basis for comparing the Reference and design scenarios by emphasising persistent bed mass changes rather than phase-dependent tidal fluctuations.

Each design scenario is evaluated relative to the Reference scenario. Changes in ΔM_{bed} describe the resulting net bed mass response, while changes in $\overline{\tau}_b$ and $\overline{c}_{IMi}$ are used as diagnostic indicators of erosion potential, sediment availability, and potential deposition. This provides a first-order framework for comparing fine sediment accumulation between the SPE designs and the Reference scenario.

This interpretation assumes that relative changes in these variables capture the dominant differences between scenarios. Mean bed shear stress is used as a proxy for erosion potential, although exceedance of the critical bed shear stress thresholds ($\tau_{cr,S1}$ and $\tau_{cr,S2}$) are not evaluated explicitly.

Table 3.5: Variables used to compare fine sediment accumulation in the port between the SPE designs and the Reference scenario. The diagnostic basis indicates that the analysis is based on observation-point time series.

Analysis component	Variables	Diagnostic basis
1) Change in bed mass	ΔM_{bed}, $\overline{\tau}_b$, $\overline{c}_{IMi}$	Observation points

3.4.4. Overview

Table 3.6 summarises the variables used to compare the SPE design alternatives with the Reference scenario across the three analysis domains. The offshore analysis evaluates changes in hydrodynamic forcing, fine sediment redistribution, and potential scour development. The transport analysis quantifies changes in sediment exchange through the Maasmond, while the port analysis assesses changes in fine sediment accumulation within the seaward basins. These variables form the basis for the results analysis, where the SPE design alternatives are evaluated primarily through relative differences with respect to the Reference scenario.

Table 3.6: Overview of variables and diagnostic basis used to compare the SPE design alternatives with the Reference scenario across the offshore domain, Maasmond transect, and port area.

Domain	Analysis component	Variables	Diagnostic basis
Offshore	Hydrodynamic response	$\overline{u}$, τ_b	Spatial fields
	Fine sediment redistribution	ΔM_{bed}, $\overline{\tau}_b$, $\overline{c}_{IMi}$	Observation points
	Scour-area development	$A_{\mathrm{SPE,new}}$, R_A, $\overline{R}_A$, $\Delta E_{\mathrm{fines,SPE}}$	Spatial fields
Transport	Total transport	F^{IM}, F^{IM}_{import}, F^{IM}_{export}	Transect-integrated
	Temporal variability	$u(t)$, $c^{IM}(t)$, $J^{IM}(t)$, $J^{IM}_{\mathrm{GF}}(t)$	Time series
	Spatial variability	$u_{m,\sigma}$, $c^{IM}_{m,\sigma}$, $F^{IM}_{m,\sigma}$, $\Delta F^{IM,\mathrm{norm}}_{m,\sigma}$	Grid-cell level
Port	Change in bed mass	ΔM_{bed}, $\overline{\tau}_b$, $\overline{c}_{IMi}$	Observation points

4
Results: Offshore

This section presents the offshore-domain results, following the methodology described in Section 3.4.1. The objective of the offshore analysis is to quantify the impact of the SPE design alternatives on the hydrodynamic conditions, fine sediment redistribution, and development of the SPE-induced scour area.

The offshore results are presented in three steps. Section 4.1 first characterises the Reference scenario, providing the baseline against which the design alternatives are evaluated. Section 4.2 then analyses the response of the SPE design scenarios relative to the Reference. Finally, Section 4.3 synthesises the main findings.

4.1. Reference scenario

The Reference simulation shows that maximum depth-averaged velocities ($\overline{u}$) in the offshore domain occur near Maasvlakte 2 (MV2), coinciding with the present-day MV2 scour area (Kroon et al. 2025).

During flood, tidal forcing drives the flow around the curvature of MV2, causing flow contraction and locally increased flow velocities, as depicted in Figure 4.1. Maximum $\overline{u}$ occurs near the western kink points of MV2, where $\overline{u} > 1.4\ \mathrm{m/s}$ within the scour area. Downstream of the erosion area, along the northern side of MV2, the flow decelerates towards the Maasmond, with $\overline{u} \approx 1.0\ \mathrm{m/s}$.

During ebb, the flow reverses relative to the flood phase, with generally lower $\overline{u}$. Flow from the Holland Coast and the Maasmond accelerates along the western side of MV2, with $\overline{u} > 1.0\ \mathrm{m/s}$. This acceleration zone overlaps with the MV2 scour area. After passing the western side of MV2, the flow decelerates. South of MV2, flow velocities remain low during ebb, with $\overline{u} < 0.3\ \mathrm{m/s}$, compared with $\overline{u} > 0.6\ \mathrm{m/s}$ during flood.

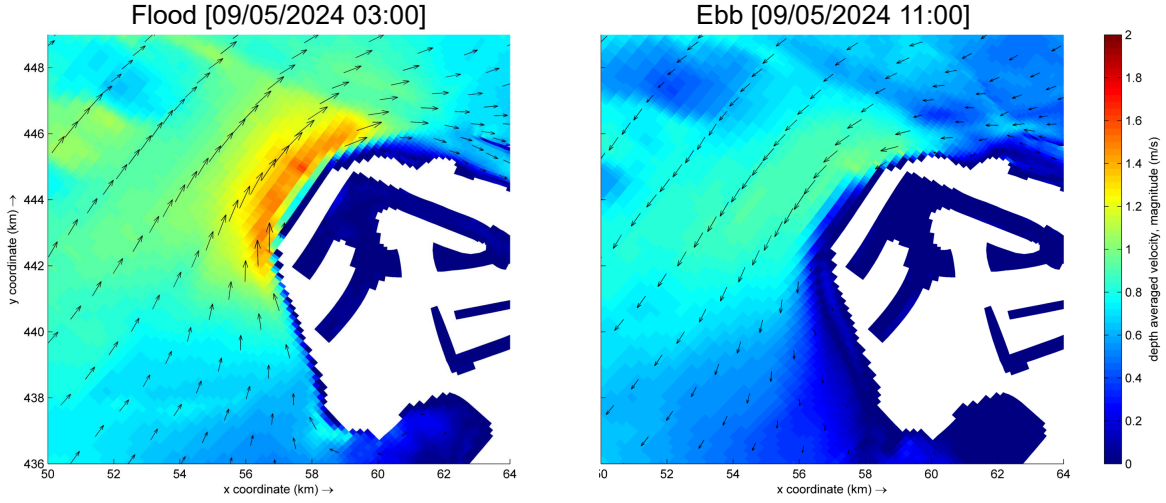

Figure 4.1: Depth-averaged velocity field ($\overline{u}$) near Maasvlakte 2 for the Reference scenario during peak flood (left) and peak ebb (right) under spring-tide conditions.

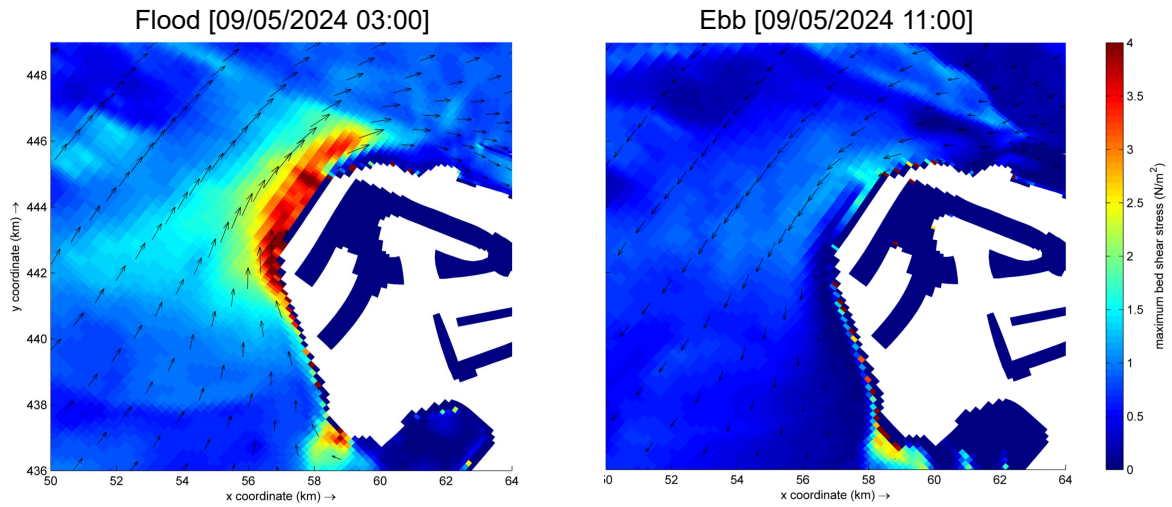

Figure 4.2: Bed shear stress field (τ_b) near Maasvlakte 2 for the Reference scenario during peak flood (left) and peak ebb (right) under spring-tide conditions.

The bed shear stress field (τ_b) is consistent with the depth-averaged velocity field, with peak τ_b occurring around MV2, as shown in Figure 4.2. During peak flood, the high flow velocities around MV2 result in $\tau_b > 3.0\ \mathrm{N/m^2}$. During ebb, bed shear stresses are lower, with $\tau_b < 1.5\ \mathrm{N/m^2}$. Since the largest and most spatially extensive bed shear stresses occur during flood, the subsequent analysis focuses on this tidal phase. Additional checks across offshore observation points show that bed shear stress exceeds the critical bed shear stress of layer S_1 ($\tau_{cr,S1}$) almost continuously, except during slack tide. The buffer-layer threshold ($\tau_{cr,S2}$) is exceeded during the flood phase of each tidal cycle, with exceedance durations and intensity increasing under spring-tide conditions.

The DELWAQ results in Figure 4.3 show that the IM fractions are distributed differently across the model domain. The finer fractions, IM1 and IM2, remain largely suspended in the offshore region and waterways, with deposition primarily confined to sheltered zones. In contrast, the higher settling velocity (w_s) of IM3 increases near-bed concentrations and promotes offshore deposition.

Supporting checks at selected offshore observation points show that the suspended sediment concentration of IM1 (c_{IM1}) remains close to its imposed boundary concentration throughout the domain. This indicates that IM1 behaves as a wash-load fraction, remaining well mixed over the water column with limited settling. As shown in Panel I of Figure 4.3, offshore bed mass of IM1 in layer S_1 ($M_{S1,IM1}$) remains below $10\ \mathrm{gDM/m^2}$, which is substantially lower than the accumulation observed in the port, where $M_{S1,IM1} > 70\ \mathrm{gDM/m^2}$. Deposition of IM1 is therefore mainly confined to harbour basins and nearshore zones, where flow velocities are lower and residence times are longer.

For IM2, supporting checks at selected offshore observation points show that the fraction remains present throughout the water column, with $c_{IM2} = 7\ \mathrm{gDM/m^3}$ near the bed and $c_{IM2} = 3\ \mathrm{gDM/m^3}$ near the surface, compared with the imposed boundary concentration of $c_{IM2} = 5\ \mathrm{gDM/m^3}$. This vertical concentration gradient indicates partial settling: IM2 remains largely suspended, while its higher w_s enhances near-bed concentrations. The final bed mass distribution in Figure 4.3 shows a spatial distribution of $M_{S1,IM2}$ that is similar to IM1, with little offshore deposition and accumulation within the Port of Rotterdam basins.

For IM3, selected offshore observation points show that $c_{IM3} = 0\ \mathrm{gDM/m^3}$ near the surface, while near-bed concentrations $c_{IM3} > 60\ \mathrm{gDM/m^3}$. This exceeds the imposed boundary concentration of $c_{IM3} = 20\ \mathrm{gDM/m^3}$ and indicates pronounced settling. Unlike the finer fractions, IM3 shows bed accumulation in the offshore region and in the main waterway, as shown in Figure 4.3. This suggests that IM3 deposits before reaching the lower-energy areas deeper inside the port and nearshore zones. Around the MV2 scour area, bed mass of IM3 is locally reduced, indicating that the hydrodynamic conditions limit IM3 deposition or promote remobilisation. South of MV2, bed mass also remains low, which is attributed to limited IM3 supply into this region.

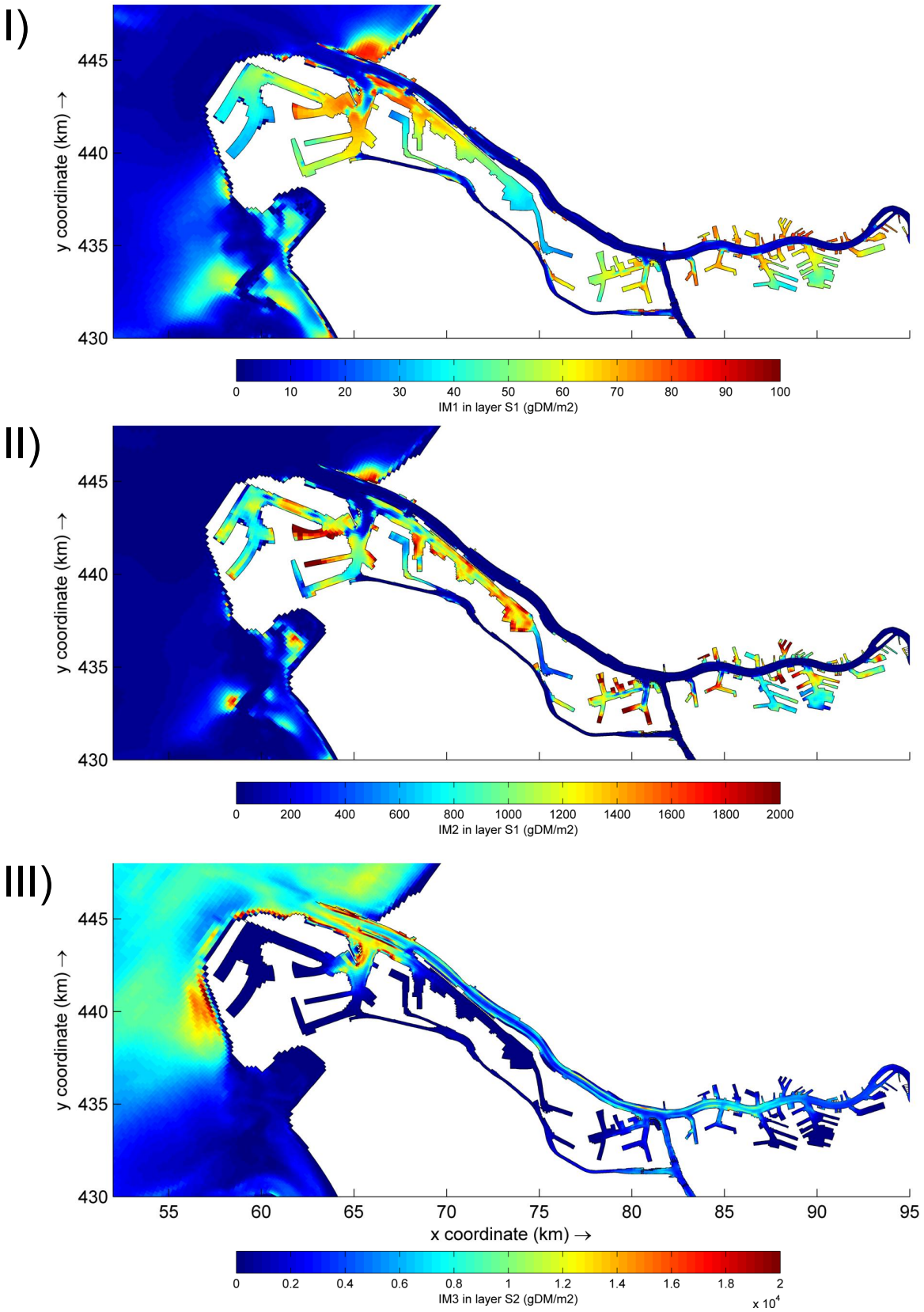

Figure 4.3: Bed mass distribution of the IM fractions in the Reference scenario at the end of the DELWAQ simulation ($M(t_1)$). Panels I, II, and III show IM1, IM2, and IM3, respectively.

4.2. SPE designs

Section 4.2.1 first presents the hydrodynamic response of the system to the SPE designs. Section 4.2.2 then identifies the main source and sink areas governing fine sediment redistribution relative to the Reference scenario. Finally, Section 4.2.3 analyses the SPE-induced scour area in detail.

4.2.1. Hydrodynamics

Larger SPE designs impose stronger contraction of the tidal flow, increasing flow velocities and bed shear stresses near MV2 and across the offshore domain. Depth-averaged velocity fields for flood are provided in Appendix C.1. Here, the bed shear stress response is emphasised, for τ_b directly governs the mobilisation potential of fine sediment. Figure 4.4 shows the bed shear stress magnitude field during peak flood for the Reference and SPE design scenarios.

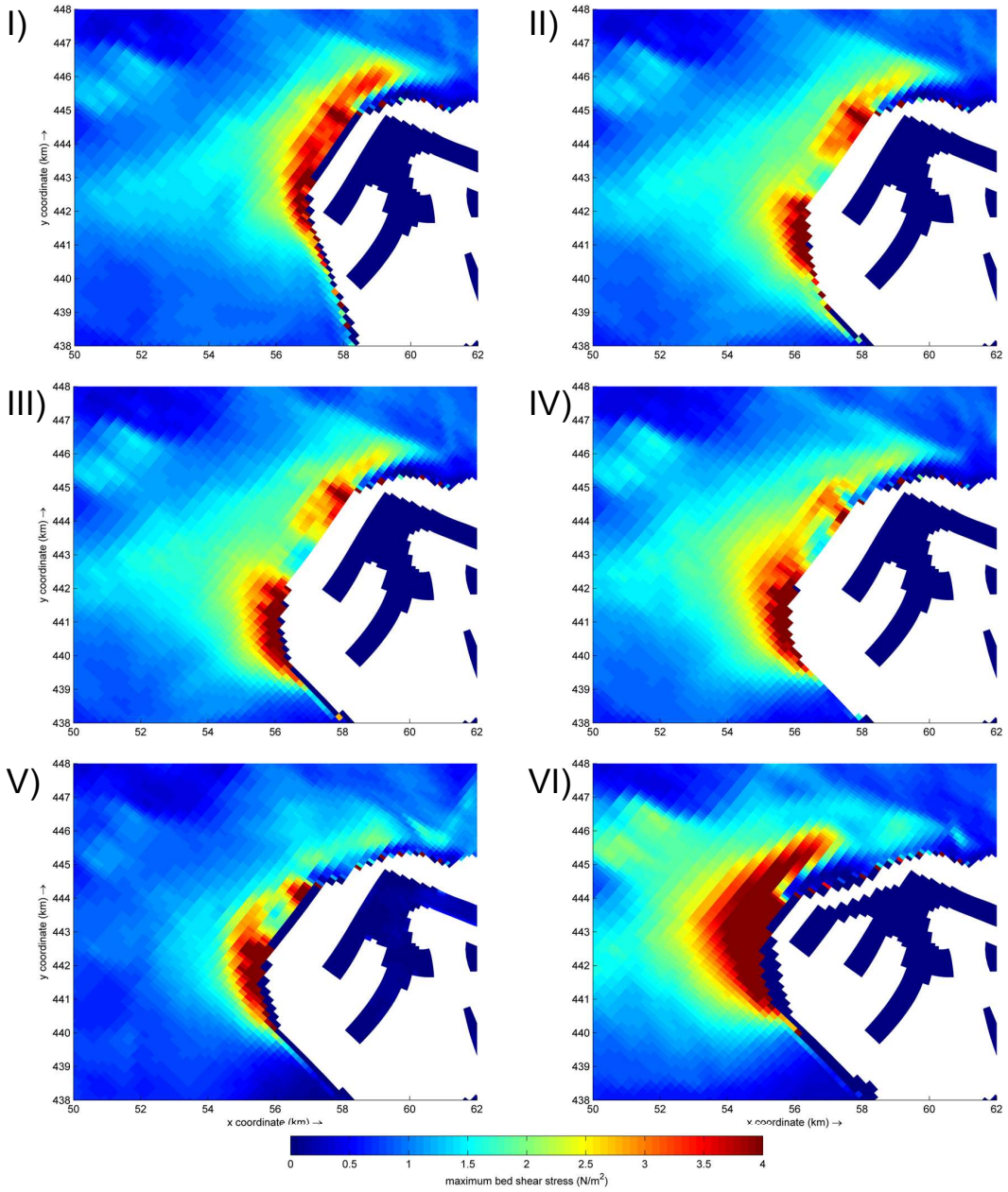

Figure 4.4: Maximum bed shear stress field during peak flood in the MV2—SPE region for (I) Reference, (II) A1, (III) A2, (IV) B1, (V) B2, and (VI) C.

Based on Figure 4.4, the following bed shear stress responses are identified:

- **A1 & A2:** For A1, local τ_b maxima occur at the two geometric corner points of the design. A2 shows a similar pattern, with a stronger τ_b maximum at the southern corner point. This indicates local strengthening of the hydrodynamic forcing due to increased flow contraction.
- **B1 & B2:** For B1, two primary τ_b maxima are present. Compared with A1 and A2, the northern maximum is weaker, while the southern maximum is stronger around the main curvature of the design. This pattern becomes more pronounced for B2: the northern maximum is further reduced and shifts southwestward towards the curvature feature, where τ_b becomes more concentrated and increases in magnitude. Relative to the Reference scenario, the zone of high τ_b north of MV2 is reduced in both B1 and B2, indicating local flow deceleration in the lee of the design.
- **C:** The pronounced geometric kink produces a single, concentrated zone of high τ_b, indicating a local erosion hotspot. The area where $\tau_b > 3\ \mathrm{N/m^2}$ is also larger than in the other SPE scenarios. Relative to the Reference scenario, the zone of high τ_b north of MV2 is further reduced, indicating flow deceleration in the lee of the geometric kink.

Overall, larger SPE designs strengthen the hydrodynamic forcing around MV2 by increasing both the magnitude of τ_b and the area over which high τ_b occurs. As the geometry expands, the zone where $\tau_b > \tau_{cr,S2}$ increases, and the primary scour-prone area shifts southwestward towards the seaward tips of the designs. This increases the potential for fine sediment mobilisation from the buffer layer S_2.

The absolute bed shear stress difference fields ($\Delta\tau_b$) show that this response is not confined to the immediate SPE geometry or the existing MV2 scour area. High $\Delta\tau_b$ values extend up to $8\ \mathrm{km}$ offshore beyond the SPE, with local increases exceeding $0.3\ \mathrm{N/m^2}$. This implies that the larger designs affect hydrodynamic conditions farther offshore, increasing the potential for fine sediment mobilisation over a broader domain. The corresponding $\Delta\tau_b$ fields are provided in Appendix C.1.

4.2.2. Fine sediment redistribution

Nine observation points were selected from the initial DELWAQ results to evaluate offshore bed mass redistribution between the SPE designs and the Reference scenario, as depicted in Figure 4.5.

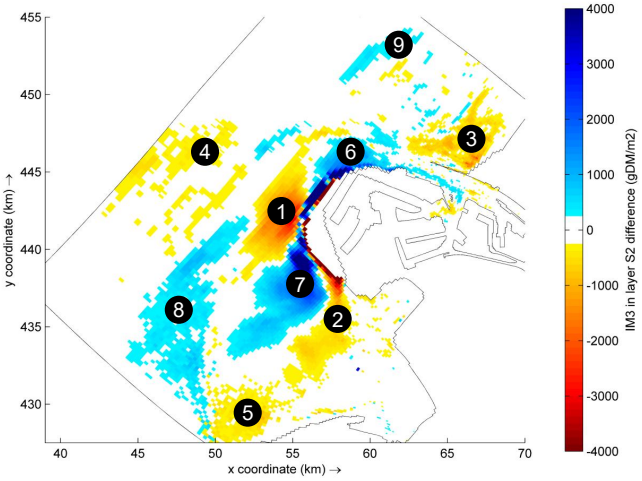

Obs. point	Location
1	Scour area
2	MV2 (South)
3	Hoek van Holland
4	Offshore (left boundary)
5	Ouddorp
6	MV2 (North)
7	MV2 (Southwest)
8	Offshore (lower boundary)
9	Offshore (upper boundary)

Figure 4.5: Difference in IM3 bed mass in Layer S_2 at the end of the DELWAQ simulation ($\Delta M_{S2}(t_1)$) between Design B1 and the Reference scenario, with selected observation points indicated. Positive values, shown in blue, indicate increased bed mass, while negative values, shown in red, indicate decreased bed mass relative to the Reference scenario. The table lists the corresponding observation point locations.

As shown in Section 4.1, IM1 and IM2 exhibit limited offshore deposition. This is confirmed by the analysis of the observation points. The SPE designs have only a limited effect on IM1 and IM2 because these fractions remain predominantly in suspension in the offshore domain. The observation point

results for all designs and IM fractions are provided in Appendix C.2. The offshore redistribution analysis focuses primarily on IM3.

As described in Section 3.4.1, this analysis uses the average bed shear stress ($\overline{\tau}_b$) as a proxy for erosion potential, while the average suspended IM3 concentration ($\overline{c}_{IM3}$) represents sediment availability and deposition potential. These metrics are used to interpret the drivers of net bed mass change (ΔM_{bed}) over the analysis period. Figure 4.6 illustrates the derivation of ΔM_{bed} for the Reference scenario and Design B1, where ΔM_{bed} is defined as the net bed mass change between the start (t_0) and the end (t_1) of the analysis period. Relative differences in ΔM_{bed}, $\overline{\tau}_b$, and $\overline{c}_{IM3}$ between each SPE design and the Reference scenario are then used to quantify the impact of the designs on offshore fine sediment dynamics.

A lower net bed mass development for an SPE simulation, for example $\Delta M_{\mathrm{bed,B1}} < \Delta M_{\mathrm{bed,Ref}}$, indicates reduced local bed mass accumulation and is interpreted as relative erosion, whereas $\Delta M_{\mathrm{bed,B1}} > \Delta M_{\mathrm{bed,Ref}}$ indicates relative accumulation. Changes in $\overline{\tau}_b$ and $\overline{c}_{IM3}$ are then used to assess whether the redistribution is driven by altered hydrodynamic forcing, altered sediment availability, or both.

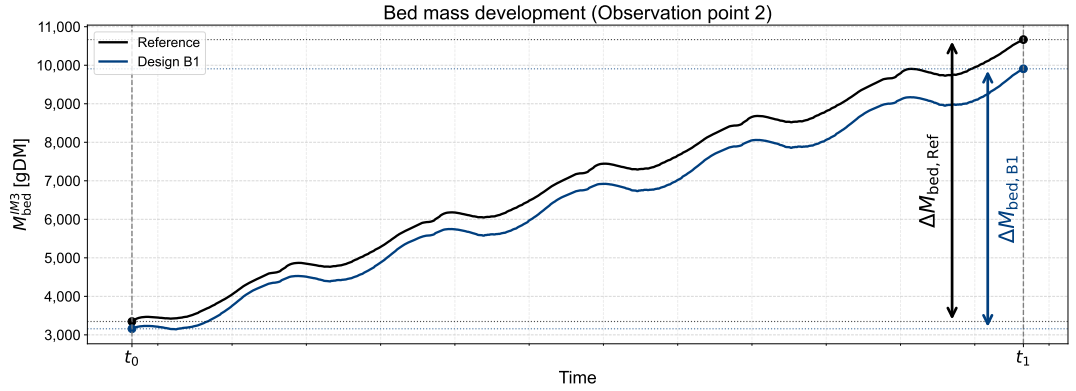

Figure 4.6: Derivation of the net bed mass change (ΔM_{bed}) between the start (t_0) and end (t_1) of the analysis period for the Reference scenario and Design B1 in Area 2. The analysis period spans six spring–neap cycles.

Table 4.1 presents the absolute Reference magnitudes of the offshore redistribution variables, together with the relative differences for Design B1. The largest bed mass changes occur near the SPE geometry, particularly at observation points 1, 2, 6, and 7.

At observation point 1, located near the seaward curvature of the SPE design, IM3 bed mass decreases in response to a strong increase in $\Delta\overline{\tau}_b = +50.8\ \%$. This corresponds to the expected southwestward shift of the scour zone, as observed in Section 4.2.1. Adjacent to this zone, bed mass increases at observation points 6 and 7. This increase is attributed to reduced flow velocities in the lee of the SPE, where lower hydrodynamic forcing favours deposition and local IM3 retention.

Table 4.1: Absolute Reference values of the offshore redistribution metrics (Ref), together with the relative differences for Design B1 (Δ). Areas in Design B1 are classified based on their relative changes in bed mass (ΔM_{bed}), mean bed shear stress ($\Delta\overline{\tau}_b$), and mean IM3 concentration ($\Delta\overline{c}_{\mathrm{IM3}}$).

Area	ΔM_{bed}		$\overline{\tau}_b$		$\overline{c}_{IM3}$		Classification
	Ref. [gDM]	Δ	Ref. [N/m^2]	Δ	Ref. [gDM/m^3]	Δ	
1	9,314	-23.3%	0.50	+50.8%	27.8	+8.4%	Erosion pit
2	4,639	-23.7%	0.16	-3.4%	5.5	-26.4%	Lower supply
3	11,128	-4.1%	0.27	-2.4%	23.7	-5.1%	Lower supply
4	5,684	-4.8%	0.59	+11.5%	16.8	+1.1%	Flow-induced scour
5	9,927	-12.4%	0.17	-5.7%	6.8	-17.0%	Lower supply
6	4,663	+28.0%	1.18	-14.2%	31.0	+2.2%	Lower flow velocity
7	12,185	+114.9%	0.23	-33.6%	15.6	+14.8%	Lower velocity and higher supply
8	8,677	+3.0%	0.41	+2.5%	20.7	+10.4%	Higher supply
9	7,069	+1.2%	0.43	-2.7%	20.6	+0.0%	Lower flow velocity

Towards Ouddorp (Area 5), bed mass decreases by $-12.4\ \%$. This response is attributed to reduced IM3 availability, as indicated by $\Delta c_{IM3} = -17.0\ \%$. Bed mass decrease is also observed south of MV2, in Area 2, driven by $\Delta c_{IM3} = -26.8\ \%$. Increased retention near MV2, particularly in Area 7, likely limits the southward IM3 supply towards Area 2.

Bed mass changes also occur at observation points 3, 4, 8, and 9, but these responses remain relatively small (less than 5%) compared with the changes near MV2. In addition, these points are located farther from the main area of interest around the Maasmond and the SPE. Therefore, the subsequent analysis focuses on observation points 1, 2, 6, and 7. These areas show the most pronounced bed mass changes, with potential implications for sediment transport towards the Maasmond.

For the selected areas of interest, Table 4.2 presents the fine sediment redistribution variables for all SPE designs. Figure 4.7 shows the corresponding spatial fields of IM3 bed mass in layer S_2 ($M_{S2}(t_1)$) for the Reference scenario and the bed mass differences for all SPE designs.

Table 4.2: Absolute values of the offshore redistribution variables for the SPE designs in the selected areas of interest: net bed mass change (ΔM_{bed}), mean bed shear stress ($\overline{\tau}_b$), and mean suspended IM3 concentration ($\overline{c}_{\mathrm{IM3}}$).

Area	Variable	Unit	Reference	A1	A2	B1	B2	C
1	ΔM_{bed}	gDM	9,314	8,132	7,766	7,146	6,306	6,122
	$\overline{\tau}_b$	N/m^2	0.50	0.62	0.67	0.75	0.86	1.03
	$\overline{c}_{IM3}$	gDM/m^3	27.8	29.9	30.2	30.2	31.0	30.6
2	ΔM_{bed}	gDM	4,639	3,709	3,182	3,540	2,958	1,784
	$\overline{\tau}_b$	N/m^2	0.16	0.16	0.17	0.16	0.15	0.15
	$\overline{c}_{IM3}$	gDM/m^3	5.5	4.6	4.0	4.0	3.3	1.8
6	ΔM_{bed}	gDM	4,663	5,105	5,328	5,966	6,339	6,758
	$\overline{\tau}_b$	N/m^2	1.18	1.14	1.13	1.01	0.91	0.78
	$\overline{c}_{IM3}$	gDM/m^3	31.0	31.9	32.4	31.7	30.3	28.6
7	ΔM_{bed}	gDM	12,185	21,476	24,647	26,191	25,829	21,072
	$\overline{\tau}_b$	N/m^2	0.23	0.18	0.17	0.15	0.14	0.12
	$\overline{c}_{IM3}$	gDM/m^3	15.6	18.0	18.6	17.9	16.3	11.1

Area 1 captures the primary scour response near the seaward curvature of the SPE geometry. Figure 4.7 and Table 4.2 show that $\overline{\tau}_b$ increases with design scale, reaching approximately twice the Reference value for Design C, from $\overline{\tau}_{b,\mathrm{Ref}} = 0.50\ \mathrm{N/m^2}$ to $\overline{\tau}_{b,\mathrm{C}} = 1.03\ \mathrm{N/m^2}$. This stronger hydrodynamic forcing reduces IM3 bed mass within Area 1. Figure 4.7 also shows that the spatial extent of this bed mass reduction increases for the larger SPE designs.

Area 2, located south of MV2 near the Slufter, shows a reduction in IM3 bed mass that increases with design scale. Since $\overline{\tau}_b$ changes only marginally in this area, the response is attributed to the decrease in $\overline{c}_{\mathrm{IM3}}$. This lower sediment availability is caused by reduced southward IM3 supply, as observed by Table 4.1.

Areas 6 and 7 respond as low-energy zones adjacent to the SPE-induced scour area. In these lee zones, reduced flow velocities promote IM3 accumulation relative to the Reference scenario. This accumulation can be the result of IM3 supplied from Area 1, from reduced local transport capacity, or from a combination of both. Under reduced flow velocities, IM3 particles that would otherwise be advected through these areas can instead settle locally in Areas 6 and 7.

In Area 6, located north of MV2, $\overline{\tau}_b$ decreases progressively with increasing design scale, from $1.18\ \mathrm{N/m^2}$ in the Reference scenario to $0.78\ \mathrm{N/m^2}$ for Design C. This decrease corresponds to a gradual increase in ΔM_{bed}, from $4{,}663\ \mathrm{gDM}$ in the Reference scenario to $6{,}758\ \mathrm{gDM}$ for Design C. For Design C, $\overline{\tau}_b$ decreases below the critical shear stress of layer S_2, $\tau_{cr,S2} = 0.8\ \mathrm{N/m^2}$, indicating reduced potential for erosion from this layer.

Area 7 shows a similar reduction in hydrodynamic forcing, with $\overline{\tau}_b$ decreasing from $0.23\ \mathrm{N/m^2}$ in the Reference scenario to $0.12\ \mathrm{N/m^2}$ for Design C. This brings $\overline{\tau}_b$ below $\tau_{cr,S1} = 0.2\ \mathrm{N/m^2}$, creating more favourable conditions for deposition and local IM3 retention. The bed mass response in Area 7 is less gradual than in Area 6: ΔM_{bed} nearly doubles for Design A1 and reaches its maximum for Design B1.

The lower ΔM_{bed} values in observation point 7 for Designs B2 and C are attributed to the spatial expansion of the reduced bed mass area associated with Area 2 into this region, as shown in Figure 4.7.

Overall, these results indicate that the SPE designs modify the offshore bed distribution of IM3. IM3 is mobilised from the SPE-induced scour area, while accumulation increases in the adjacent lee zones. The key remaining question is whether this offshore redistribution increases fine sediment transport towards and into the port. This transport response is analysed in Chapter 5. The next section examines Area 1 in more detail by analysing scour-area development and quantifying the additional volume of fine sediment released from this zone.

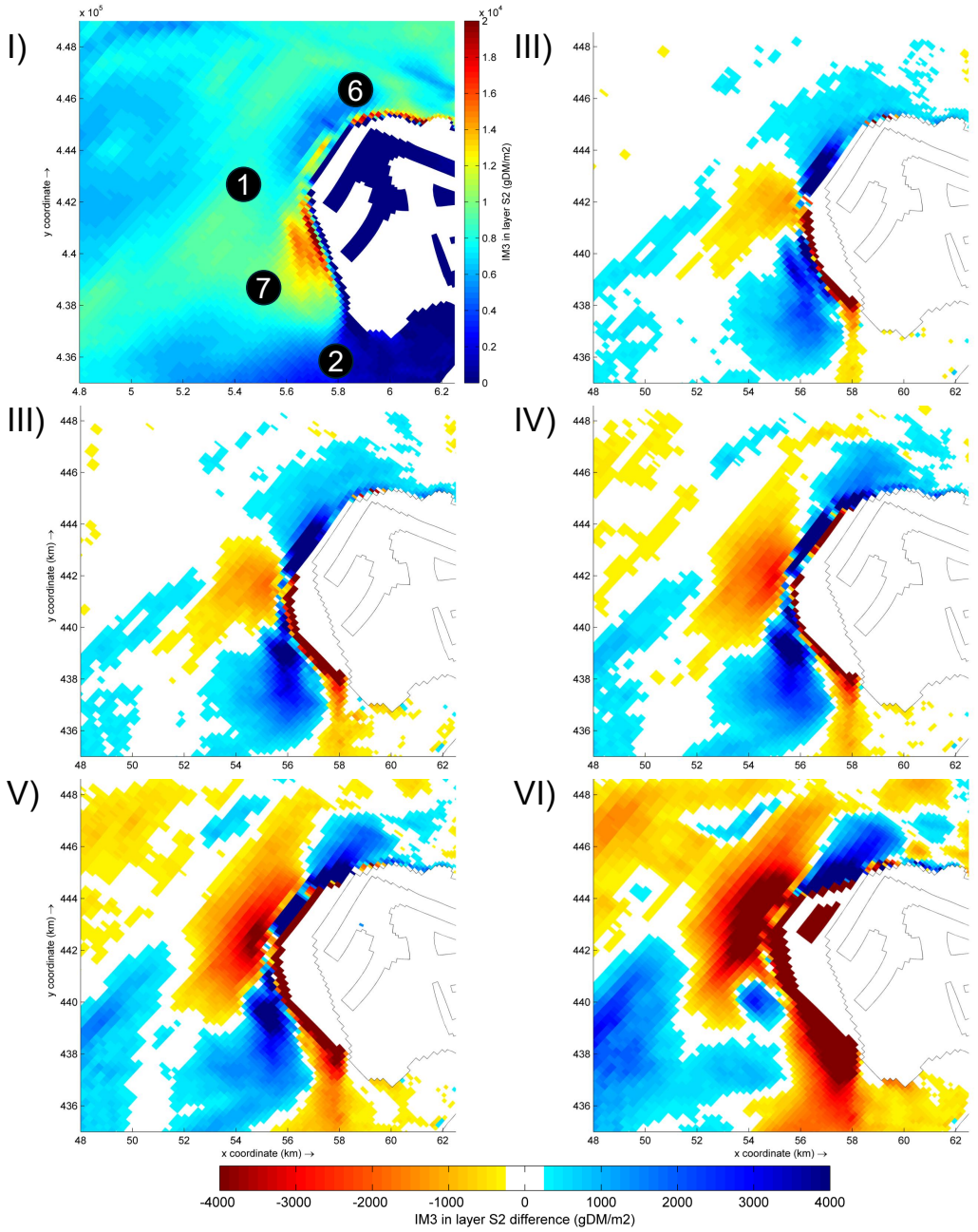

Figure 4.7: IM3 bed mass in layer S_2 at the end of the DELWAQ simulation, $M_{S2}(t_1)$. Panel I shows the Reference scenario, while panels II–VI show absolute bed mass differences relative to the Reference scenario for designs A1, A2, B1, B2, and C, respectively. Positive values (blue) indicate increased bed mass, while negative values (red) indicate decreased bed mass.

4.2.3. Quantification of scour area

This section quantifies the SPE-induced increase of the existing MV2 scour area and the associated release of fine sediment to the system. As discussed in Section 3.4.1, the Delft3D-based estimate of the relative increase in potential scour area ($\overline{R}_A$) is compared with the SVASEK estimates to assess consistency between the two approaches. The derivation of $\overline{R}_A$ is provided in Appendix C.3. If both approaches show a similar order of magnitude and design-scale trend, the SVASEK estimates of increased scour volume are used in the subsequent fine sediment release calculation. The results are shown in Figure 4.8.

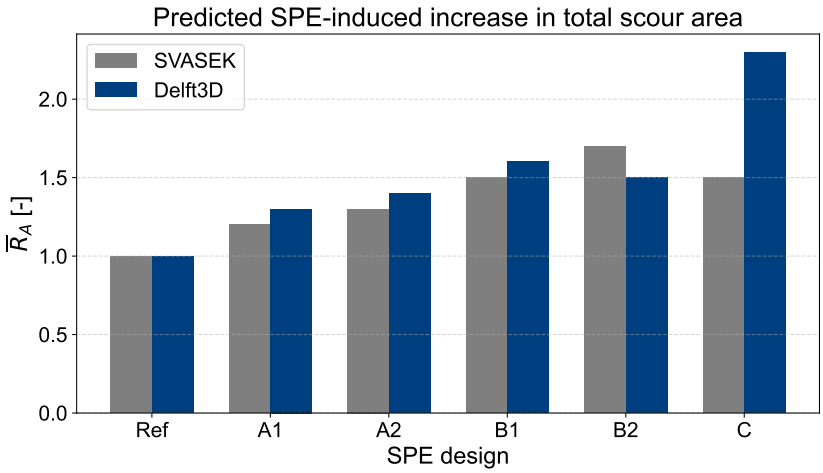

Figure 4.8: Comparison of the relative increase in scour area ($\overline{R}_A$) for each SPE design relative to the existing MV2-induced scour area in the Reference scenario. Values are shown for the SVASEK projections and the Delft3D-based estimates from this research (Kroon et al. 2025).

The SVASEK estimates and the Delft3D-based estimates show comparable trends across the SPE designs, except for Design C, for which the Delft3D-based approach indicates a substantially larger increase in potential scour area. This discrepancy is likely related to the sensitivity of the more extreme design geometry and to the uncertainty inherent to both estimation methods, as neither approach includes morphodynamic feedback.

Given the uncertainty range reported by SVASEK, approximately -50% to +200%, the results should be interpreted as first-order estimates of relative change rather than precise predictions of the final erosion geometry. The overall consistency between the two approaches supports the use of the SVASEK projections of the SPE-induced increase in scour volume (ΔV_{SPE}) in the subsequent fine sediment release calculation.

To translate the projected scour development into potential fine sediment release, the erosion rate observed for the existing MV2 scour pit is used as a reference erosion rate. This rate is scaled by the SVASEK-projected relative increase in erosion-pit volume induced by the SPE designs. This scaling assumes that the existing MV2 scour area and the SPE-induced scour area have comparable bed composition and follow similar scour–development over time.

The additional fine sediment release attributed to the SPE ($\Delta E_{fines,SPE}$) is then calculated by:

$$\Delta E_{\mathrm{fines,SPE}} = E_{\mathrm{MV2}} \cdot C_{\mathrm{fines}} \cdot \Delta V_{\mathrm{SPE}} \tag{4.1}$$

Here, E_{MV2} denotes the erosion rate of the MV2 scour pit $[\mathrm{Mm}^3/\mathrm{year}]$, C_{fines} the fine sediment content of the bed and therefore of the eroded volume $[-]$, and ΔV_{SPE} the dimensionless SVASEK-projected relative increase in erosion-pit volume induced by the SPE designs $[-]$.

Figure 4.9 shows the PUMA monitoring measurements of the annual erosion rate in the MV2 scour area. The observed rates decrease over time, which is consistent with the expected morphological adjustment of a scour pit towards a stable geometry. Scour-hole evolution progresses through initial,

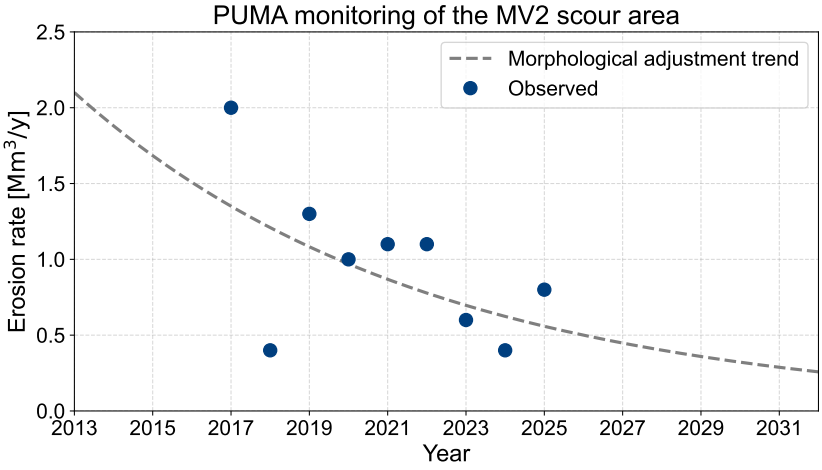

Figure 4.9: PUMA monitoring measurements of the annual erosion rate in the MV2 scour area over 2017–2025, shown in blue (Waal 2025). The erosion rate represents the total annual erosion, including both coarse and fine sediment. The dashed curve illustrates the morphological adjustment of the scour area towards dynamic equilibrium and is not a statistically calibrated fit.

development, stabilisation, and equilibrium phases, with the highest erosion rates occurring shortly after the initial bed disturbance and progressively declining as the system approaches dynamic equilibrium (Hoffmans et al. 2021). The dashed curve is included as an indicative morphological adjustment trend, not as a statistically calibrated prediction of future erosion volumes, because the number of monitoring measurements is too limited to support a robust statistical fit.

From Figure 4.9, two erosion rates are selected for the fine sediment release calculation: (i) the time-averaged erosion rate over 2013–2025, $E_{\mathrm{MV2,avg}}$, and (ii) the 2017 erosion rate, $E_{\mathrm{MV2,high}}$. The 2017 value is used as a proxy for early post-construction conditions. As discussed in Section 2.5, the fine sediment content in the high-energy scour zone is expected to be low, in the order of 1% (Berkenbosch et al. 2006). However, to obtain a conservative estimate, $C_{\mathrm{fines}} = 4\ \%$ is applied. In addition, a conservative assumption is made that all fine sediment released from the SPE-induced scour area enters the port through the Maasmond.

Table 4.3 summarises the assumptions and constants used to estimate the SPE-induced fine sediment release from the additional potential scour area. The resulting fine sediment release is shown in Table 4.4, together with the corresponding increase in maintenance dredging demand (ΔD), expressed relative to the yearly dredged volume of the Port of Rotterdam.

Table 4.3: Assumptions and constants used to estimate the relative increase in maintenance dredging demand associated with fine sediment released from the SPE-induced scour area.

Parameter	Value
C_{fines} [%]	4
Port-bound fraction of released fines [%]	100
$E_{\mathrm{MV2,avg}}$ [10^3 m^3/yr]	690
$E_{\mathrm{MV2,high}}$ [10^3 m^3/yr]	2,000
Annual maintenance dredging volume PoR [Mm^3/yr]	10

The estimated SPE-induced fine sediment release increases with design scale, reflecting the SVASEK-projected increase in erosion-pit volume. However, the absolute contribution remains small because the content of fines in the eroded volume is limited. For Design C, the maximum fine sediment release is $\Delta E_{fines,SPE,high} = 72.0 \times 10^3\ \mathrm{m}^3/\mathrm{yr}$, corresponding to a maximum increase in maintenance dredging demand of $\Delta D = 0.72\ \%$. For Design B1, the average release estimate corresponds to an increase in maintenance dredging demand of $\Delta D = 0.08\ \%$.

Table 4.4: Estimated fine sediment release ($\Delta E_{\mathrm{fines,SPE}}$) and corresponding relative increase in maintenance dredging demand (ΔD), based on the SPE-induced increase in scour volume (ΔV_{SPE}) from SVASEK, the assumptions listed in Table 4.3, and Equation 4.1. Results are reported for both the average and high-value erosion projections.

Parameter	A1	A2	B1	B2	C
ΔV_{SPE} [%]	10	10	30	60	90
$\Delta E_{\mathrm{fines,SPE,avg}}$ [10^3 m^3/yr]	2.8	2.8	8.3	16.6	24.8
$\Delta E_{\mathrm{fines,SPE,high}}$ [10^3 m^3/yr]	8.0	8.0	24.0	48.0	72.0
ΔD_{avg} [%]	0.03	0.03	0.08	0.17	0.25
ΔD_{high} [%]	0.08	0.08	0.24	0.48	0.72

Even under the applied conservative assumptions, the projected increase in dredging demand due to newly released fines remains small relative to the annual dredged volume of the Port of Rotterdam. This conclusion also holds under even more conservative erosion-rate assumptions. For example, an MV2 erosion rate of $4\ \mathrm{Mm^3/yr}$ would increase the estimated fine sediment release, but the resulting volume would still be too small to explain the increase in maintenance dredging demand observed after the construction of MV2, as shown in Figure 1.1. Fine sediment release from the SPE-induced scour area is therefore expected to have limited impact on maintenance dredging demand.

4.3. Synthesis

In the Reference scenario, tidal flow contraction around MV2 generates high flow velocities along the western side of MV2, reaching $\overline{u} > 1.4\ \mathrm{m/s}$, with correspondingly high bed shear stresses. These energetic offshore conditions keep IM1 and IM2 largely in suspension, with deposition of these fractions being mainly confined to sheltered port basins. IM3 settles more readily in the offshore domain, making it the dominant fraction for offshore bed mass redistribution.

The SPE designs strengthen flow contraction around MV2 and increase local hydrodynamic forcing. With increasing design scale, $\overline{\tau}_b$ increases and the zone of maximum forcing shifts southwestward towards the seaward curvature and kink points of the designs.

Offshore redistribution of fines is mainly expressed through IM3, because IM1 and IM2 show limited offshore deposition. Changes in IM3 bed mass occur primarily near the SPE geometry. Bed mass decreases near the seaward curvature of the designs, where the SPE-induced scour area develops, while IM3 accumulation increases in the adjacent lee zones. This redistribution pattern becomes more pronounced with increasing design scale. Accumulation of IM3 in the lee zones can result from IM3 supplied from the newly induced scour area, reduced local transport capacity, or a combination of both. Reduced flow velocities would allow IM3 particles that would otherwise be advected through these areas to settle locally in these low-energy zones.

However, the first-order estimate indicates that SPE-induced fine sediment release from the scour area is small. Even for Design C, the maximum estimated release corresponds to an upper-bound increase of < 1% relative to the annual dredging volume, assuming that all released fines are transported into the Port of Rotterdam basins. The contribution of newly released fines is therefore negligible at the scale of annual maintenance dredging. Changes in transport through the Maasmond are expected to result mainly from altered offshore fine sediment redistribution patterns, rather than from direct fine sediment release from the SPE-induced scour area. The next chapter evaluates whether and how this offshore redistribution affects fine sediment transport through the Maasmond.

5
Results: Transport

This section analyses fine sediment transport through the Maasmond transect following the methodology described in Section 3.4.2. Section 5.1 first characterises the Reference simulation to establish the baseline transport behaviour. Section 5.2 then compares the SPE design scenarios with the Reference scenario in terms of total transport, temporal variability over a spring–neap cycle, and spatial variability across the transect. Section 5.3 synthesises the main findings.

5.1. Reference scenario

Consistency checks were performed for the Reference scenario to verify the transport calculations. First, the residual error in the transport balance, $\epsilon = F_{\text{net}} - (F_{\text{import}} - F_{\text{export}}) < 2 \times 10^{-4}$ gDM, which confirms consistency of the transport decomposition. Second, the water-volume balance was evaluated using the net discharge. The modelled net discharge through the Maasmond is directed seaward, with $Q_{\text{model}} = 1.6 \times 10^3$ m^3/s. This is close to the reported annual mean discharge through the Maasmond, $Q_{\text{obs}} = 1.7 \times 10^3$ m^3/s (Cox et al. 2021). The slightly lower modelled discharge is attributed to the hydrodynamic forcing imposed on the model, which does not include high-discharge events that contribute to the observed annual mean. These checks confirm the hydrodynamic consistency of the model and the validity of the Maasmond transport post-processing.

The horizontal flow velocity normal to the Maasmond transect (u_n) is shown in Figure 5.1. The profile shows seaward flow near the surface, driven by freshwater discharge from the Rhine-Meuse delta, and landward flow in the lower water column, corresponding to saline inflow into the port system. This two-layer structure is consistent with the stratified estuarine exchange described in Section 2.3.

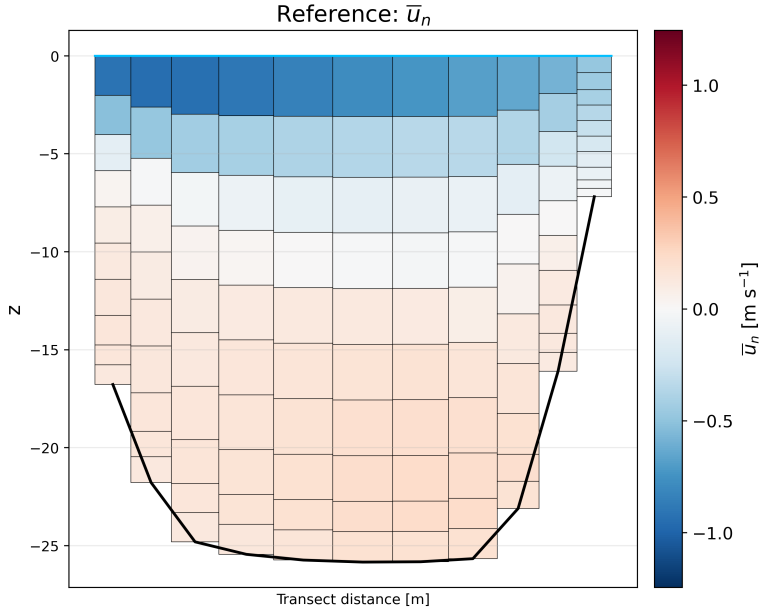

Figure 5.1: Mean horizontal flow velocity profile ($\overline{u}_n$) along the Maasmond transect for the Reference scenario. Positive values, shown in red, indicate landward flow into the port, while negative values, shown in blue, indicate seaward flow towards the North Sea. The transect is oriented from Hoek van Holland (left) to Maasvlakte (right).

The total fine sediment transport (F) through the Maasmond differs between sediment fractions, as shown in Tables 5.1–5.3. Fractions IM1 and IM2 both show net export from the port system, indicated by $F_{\mathrm{net}} < 0$. This is consistent with their respective low settling velocities (w_s), which keep these fractions in suspension over longer timescales. As the net water discharge through the Maasmond is directed seaward, IM1 and IM2 are primarily transported with the residual outflow, resulting in net export.

In contrast, IM3 shows net import into the port system. For this fraction, $F_{\mathrm{import}} = 2.7 \times |F_{\mathrm{export}}|$, indicating that landward transport by stratified exchange flow exceeds seaward export by residual river discharge. After entering the port system, the higher w_s of IM3 promotes deposition under the weaker hydrodynamic forcing in the waterway and basins. Subsequent resuspension in the port and export towards the sea remain limited because local bed shear stresses (τ_b) are generally insufficient to remobilise this fraction.

Table 5.1: Transport IM1, Reference scenario.

IM1	[tonDM]
F_{net}	-8,916
F_{import}	28,579
F_{export}	37,495

Table 5.2: Transport IM2, Reference scenario.

IM2	[tonDM]
F_{net}	-9,662
F_{import}	182,064
F_{export}	191,726

Table 5.3: Transport IM3, Reference scenario.

IM3	[tonDM]
F_{net}	526,331
F_{import}	840,246
F_{export}	313,915

The temporal variability of the variables for IM3 over a full spring–neap cycle is shown in Figure 5.2. The corresponding plots for IM1 and IM2 are provided in Appendix D.2.

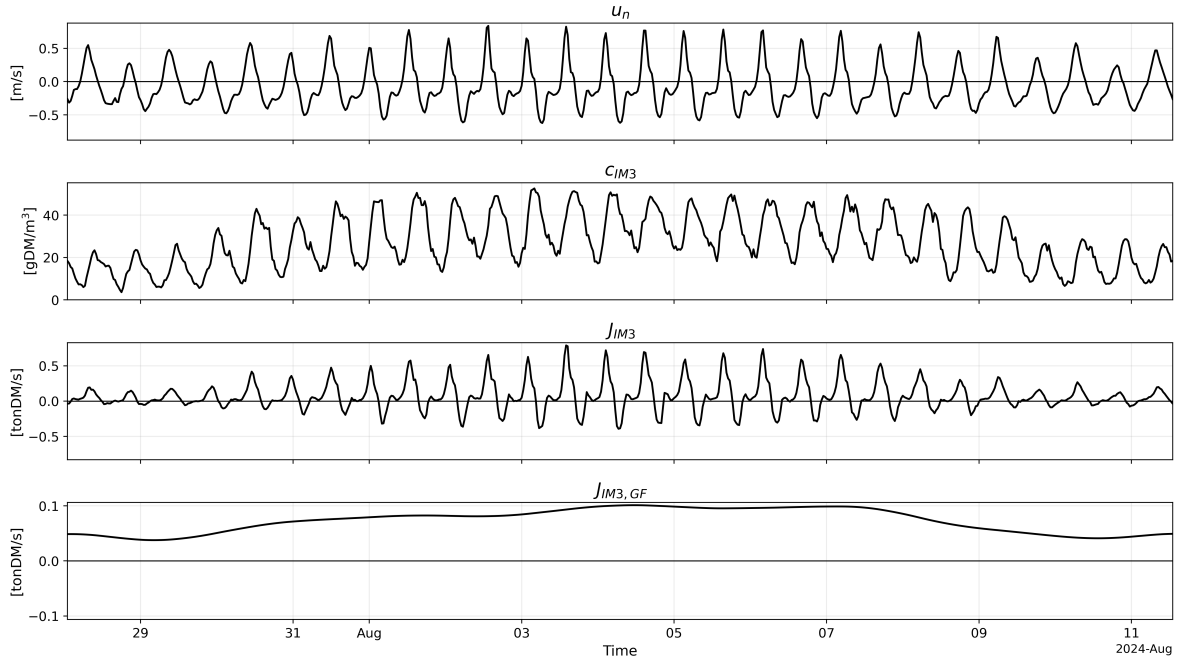

Figure 5.2: Time series of transect-integrated variables along the Maasmond transect over a spring–neap cycle for the Reference scenario. The panels show horizontal velocity (u_n), IM3 concentration (c_{IM3}), advective IM3 flux (J_{IM3}), and the corresponding Godin-filtered IM3 flux ($J_{\mathrm{IM3,GF}}$).

The upper panel shows the transect-integrated normal velocity component ($u_n(t)$). The amplitude of u_n increases towards the middle of the spring–neap cycle, corresponding to spring-tide conditions.

The suspended concentration of IM3 ($c_{\mathrm{IM3}}(t)$) varies over the tidal cycle, with higher concentrations during spring tide. This response is attributed to stronger tidal forcing offshore, which enhances offshore resuspension. Spring–neap variability in suspended sediment concentration is less pronounced for IM1

and IM2. These fractions remain largely in suspension throughout the tidal cycle, so increased tidal forcing produces only limited relative changes in concentrations.

The advective flux ($J_{\mathrm{IM3}}(t)$) shown in the third panel reflects the combined variability in $u_n(t)$ and $c_{\mathrm{IM3}}(t)$. Towards spring-tide, larger velocity and concentration amplitudes produce stronger oscillations in $J_{\mathrm{IM3}}(t)$. The fourth panel shows the Godin-filtered flux of IM3 ($J_{\mathrm{IM3,GF}}(t)$). This subtidal signal remains positive throughout the spring-neap cycle, indicating persistent import into the port, consistent with the net import reported in Table 5.3.

Figure 5.3 shows the concentration and transport fields over the Maasmond transect for IM1–IM3. For IM1, the concentration field is nearly uniform over the water column (Panel I). Across the entire

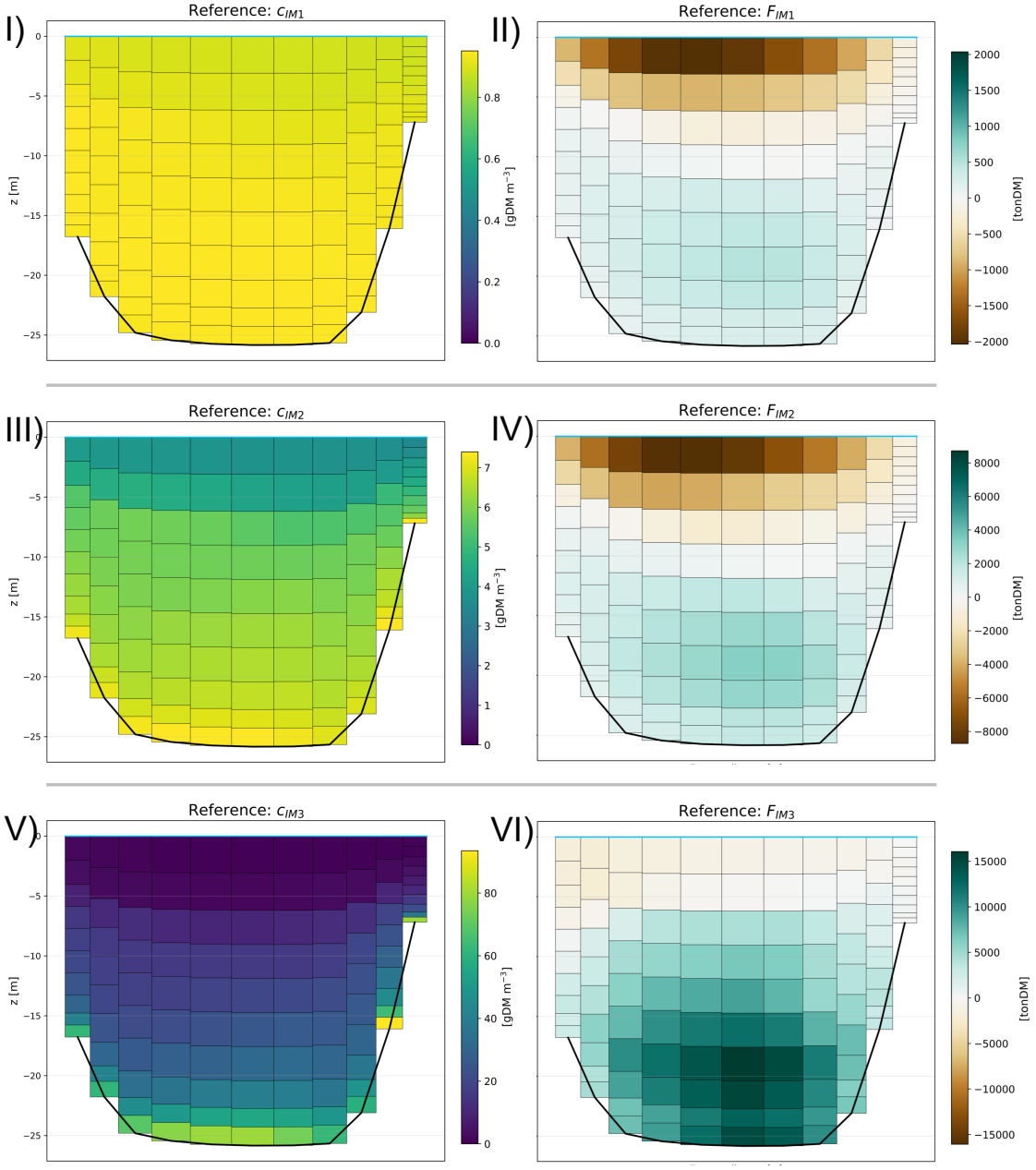

Figure 5.3: Time-averaged suspended sediment concentration and advective transport along the Maasmond transect for the Reference scenario. The left panels show suspended sediment concentration ($\bar{c}_{\mathrm{IMi}}$), while the right panels show transport (F_{IMi}) per grid cell. Panels I–II, III–IV, and V–VI correspond to IM1, IM2, and IM3, respectively. Positive transport values indicate landward transport into the port. The transect is oriented from Hoek van Holland (left) to Maasvlakte (right).

transect, $c_{\mathrm{IM1}} > 0.95\ \mathrm{gDM/m^3}$, which is close to the imposed offshore boundary concentration of $c_{\mathrm{IM1}} = 1.0\ \mathrm{gDM/m^3}$. The corresponding transport field, F_{IM1} (Panel II), follows the vertical velocity profile shown in Figure 5.1: landward transport occurs in the lower water column, while seaward transport dominates near the surface.

For IM2, the concentration field shows a vertical gradient, with c_{IM2} increasing with depth from 4 gDM/m^3 near the surface to 7 gDM/m^3 near the bed. This indicates that IM2 is present throughout the water column, with enhanced concentrations near the bed. The corresponding transport field, F_{IM2} (Panel IV), is similar to IM1, with dominant seaward transport near the surface and weaker landward transport in the lower water column.

For IM3, suspended concentrations are strongly confined to the lower water column (Panel V), with near-bed $c_{\mathrm{IM3}} > 60\ \mathrm{gDM/m^3}$. The corresponding transport field, F_{IM3} (Panel VI), shows dominant landward transport, especially in the deeper central part of the transect. Transport in the upper water column is negligible due to the absence of IM3. This vertical structure indicates that net IM3 import is primarily controlled by near-bed landward transport associated with saline inflow.

The Reference simulation shows clear fraction-dependent transport behaviour across the Maasmond transect. IM1 and IM2 remain distributed over most of the water column, so both near-bed landward transport and upper-water-column seaward transport contribute to the total exchange. In contrast, IM3 is concentrated near the bed, where residual transport is predominantly landward.

5.2. SPE designs

The SPE designs are evaluated relative to the Reference scenario to assess their effect on fine sediment exchange through the Maasmond. The comparison follows the Reference analysis and considers total transport, temporal variability, and spatial distribution of transport across the transect.

5.2.1. Total transport

Table 5.4 shows the differences in F_{net}, F_{import}, and F_{export} for each SPE design relative to the Reference scenario. The corresponding absolute transport values for each sediment fraction and scenario are provided in Appendix D.1.

For interpretation, relative transport changes are grouped into three response classes. Changes with $|\Delta F| < 1\%$ are classified as negligible, as they are assumed to fall within the uncertainty of the model set-up and post-processing procedure. Changes with $1\% \leq |\Delta F| \leq 3\%$ are classified as moderate, indicating a measurable but limited scenario response. Changes with $|\Delta F| > 3\%$ are classified as pronounced, indicating a clear change in transport behaviour relative to the Reference scenario.

Table 5.4: Sediment transport through the Maasmond transect for fractions IM1, IM2, and IM3, decomposed into net transport (F_{net}), import (F_{import}), and export (F_{export}). Absolute transport magnitudes are reported for the Reference scenario, while relative changes for the SPE scenarios are reported under Δ with respect to the Reference scenario.

Fraction	Transport	Reference	Δ				
		[tonDM]	A1	A2	B1	B2	C
IM1	F_{net}	-8,916	-0.17%	-0.15%	-0.32%	-0.37%	-0.75%
	F_{import}	28,579	-0.07%	-0.29%	-0.32%	-0.72%	+0.35%
	F_{export}	37,495	-0.09%	-0.25%	-0.32%	-0.64%	+0.09%
IM2	F_{net}	-9,662	-1.94%	-0.05%	-1.22%	-2.44%	-10.43%
	F_{import}	182,064	+0.39%	-0.17%	-0.12%	-1.06%	-0.09%
	F_{export}	191,726	+0.27%	-0.17%	-0.18%	-1.12%	-0.61%
IM3	F_{net}	526,331	+0.52%	+0.35%	-0.91%	-4.17%	-9.00%
	F_{import}	840,246	+0.81%	+0.70%	-0.56%	-3.68%	-7.71%
	F_{export}	313,915	+1.30%	+1.27%	+0.03%	-2.86%	-5.56%

Note: Cells are coloured when $|\Delta| \geq 1\%$. Blue denotes a decrease, red denotes an increase, and darker shades indicate changes exceeding 3%.

Transport of IM1 shows negligible sensitivity to the SPE designs. For all designs, relative changes in F_{net}, F_{import}, and F_{export} are less than 1%, with no systematic trend across design scale. This indicates that IM1 exchange through the Maasmond is largely unaffected by the SPE designs.

For IM2, all SPE designs reduce the magnitude of F_{net}. Since $F_{\mathrm{net}} < 0$ in the Reference scenario, this reduction corresponds to weaker net export and therefore increased retention of IM2 within the port system. For Design C, the pronounced relative change in net IM2 transport, $\Delta F_{\mathrm{net}} = -10.43\ \%$, is not driven by substantial changes in F_{import} or F_{export}, which are both less than 1%. Instead, it results from the near-balance between import and export of IM2 in the Reference scenario, where small absolute changes in either component can produce a large relative change in F_{net}.

Transport of IM3 through the Maasmond shows the strongest response to the SPE designs. Although Designs A1, A2, and B1 produce negligible changes in F_{net}, Designs B2 and C reduce F_{net} by 4.17% and 9.00%, respectively. For these larger designs, the reduction in F_{net} is mainly driven by a decrease in F_{import}, which dominates the IM3 transport balance. Although enhanced offshore mobilisation of IM3 could be expected to increase landward transport through the Maasmond, the larger SPE designs instead reduce IM3 import into the port system.

Overall, the SPE designs have limited effects on the transport of IM1 and IM2. This is attributed to their low w_s, which keeps both fractions largely in suspension and reduces their sensitivity to SPE-induced hydrodynamic changes. IM3 shows the strongest response, particularly for Designs B2 and C, where F_{import} decreases.

5.2.2. Temporal variability of transport

The temporal analysis quantifies SPE-induced changes over the spring–neap using the transect-integrated variables: horizontal flow velocity, $u_n(t)$; suspended sediment concentration, $c(t)$; instantaneous flux, $J(t)$; and Godin-filtered flux, $J_{\mathrm{GF}}(t)$.

The full time series of u_n, c, J, and J_{GF} for IM1–IM3 and all SPE configurations are provided in Appendix D.2. The u_n time series show no visible deviations between the Reference scenario and the SPE designs. This indicates that cross-sectional flow variability remains largely unchanged. Changes in J and J_{GF} are therefore primarily attributed to changes in concentration, reflecting SPE-induced differences in sediment supply.

For IM1 and IM2, the time series of c, J, and J_{GF} show minor to no deviations from the Reference scenario. The advective flux signal remains largely unchanged over the spring–neap cycle, consistent with the negligible to small changes in net transport reported in Table 5.4. The temporal analysis therefore focuses on IM3, for which the SPE-induced differences are more pronounced.

Figure 5.4 shows the temporal response of IM3 transport for the SPE designs relative to the Reference scenario. The upper panel compares c_{IM3} for the Reference scenario and Design C. Both signals remain in phase with the tidal cycle, but Design C shows lower peaks in concentration, particularly during flood. This indicates reduced suspended IM3 availability during landward transport phases. This reduction is reflected in the middle panel, where the Godin-filtered flux ($J_{\mathrm{IM3,GF}}$) is lower for Design C than for the Reference scenario. Since $J_{\mathrm{IM3,GF}} > 0$ denotes landward transport, this corresponds to reduced IM3 import through the Maasmond.

The lower panel shows the SPE-induced absolute flux difference for all designs, defined as $\Delta J_{\mathrm{IM3,GF}} = J_{\mathrm{IM3,GF,SPE}} - J_{\mathrm{IM3,GF,Ref}}\ [\mathrm{gDM/s}]$. Designs A1, A2, and B1 remain close to $\Delta J_{\mathrm{IM3,GF}} = 0$, indicating minor changes in the filtered IM3 transport signal. In contrast, Designs B2 and C show persistently $\Delta J_{\mathrm{IM3,GF}} < 0$ over most of the spring–neap cycle, indicating reduced landward IM3 flux. Since differences in u_n are negligible, this reduction is attributed to lower suspended concentrations rather than changes in flow. The temporal analysis therefore confirms that the reduced net import for Designs B2 and C is primarily concentration-driven.

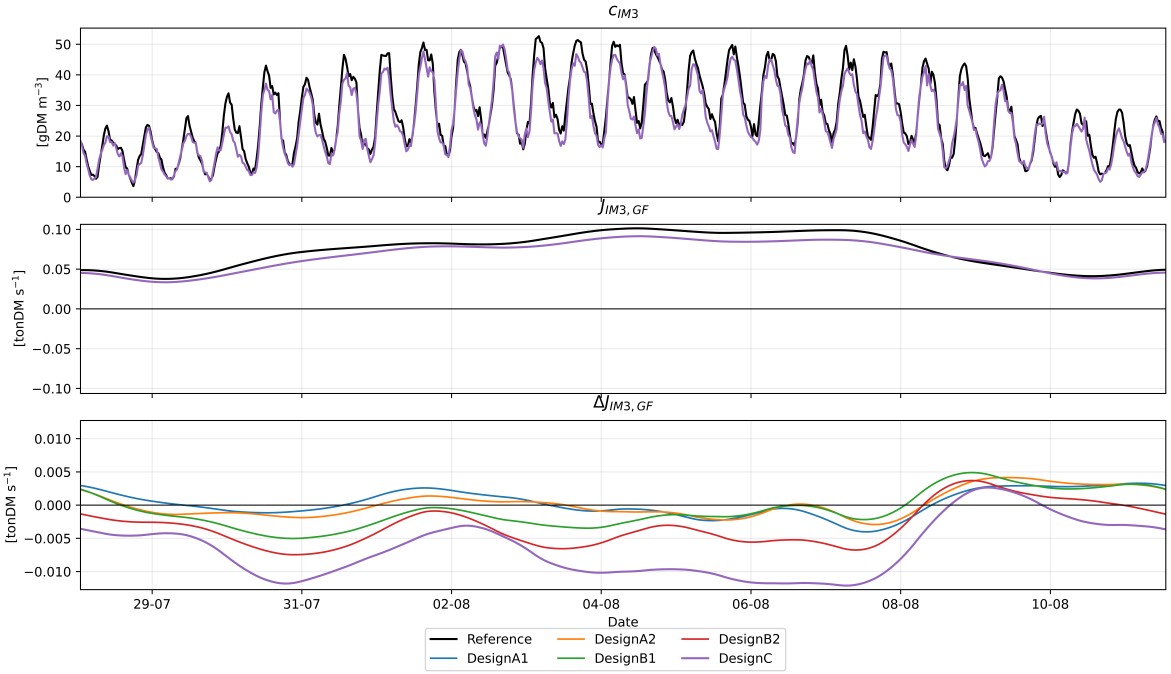

Figure 5.4: Time series of transect-integrated variables along the Maasmond transect over a spring–neap cycle for the Reference scenario and SPE designs. The upper panel shows IM3 concentration (c_{IM3}) for the Reference scenario and Design C, while the middle panel shows the corresponding Godin-filtered advective IM3 flux ($J_{\mathrm{IM3,GF}}$). The lower panel shows the design-induced flux difference for all SPE designs, defined as $\Delta J_{\mathrm{IM3,GF}} = J_{\mathrm{IM3,GF,SPE}} - J_{\mathrm{IM3,GF,Ref}}$. Negative values indicate reduced advective flux relative to the Reference scenario, while positive values indicate increased advective flux.

5.2.3. Spatial variability of transport

In the spatial analysis, u, c, and F are evaluated for each grid cell across the Maasmond transect. Consistent with the temporal analysis, the SPE designs have a negligible effect on the horizontal velocity structure across the transect. Grid-cell differences in horizontal velocity remain below $0.01\ \mathrm{m/s}$ for all designs, and they show no coherent spatial pattern. Transport differences are therefore primarily concentration-driven, so the spatial analysis focuses on changes in c and F.

The normalised grid-cell transport differences, $\Delta F_{\mathrm{IM}i,\mathrm{norm}}$, are negligible for IM1 and IM2. Values remain within $\pm 0.05\ \%$ for IM1 and within $\pm 0.10\ \%$ for IM2. Neither fraction shows a systematic spatial response over the transect. This is consistent with the total transport and temporal analyses. Therefore, the spatial analysis focuses on IM3, for which the transport response is more pronounced, particularly for Designs B2 and C.

Figure 5.5 shows the grid-cell concentration difference for IM3 across the Maasmond transect, defined as $\Delta c_{\mathrm{IM3}} = \overline{c}_{\mathrm{IM3,SPE}} - \overline{c}_{\mathrm{IM3,Ref}}$. The response separates into two design groups: A1, A2, and B1 show similar concentration-difference patterns, whereas B2 and C show a stronger and more spatially coherent reduction.

For Designs A1, A2, and B1, Δc_{IM3} increases by 2–$4\ \mathrm{gDM/m^3}$ near the bed on the MV2 side of the transect. This local increase is consistent with enhanced IM3 mobilisation near the SPE and MV2, which increases sediment availability for landward transport through the Maasmond. However, the corresponding changes in F_{import} remain limited (Table 5.4), indicating that the local concentration increase does not substantially affect total IM3 import.

For Designs B2 and C, the concentration field shows an overall reduction in c_{IM3}, especially in the lower water column where IM3 is primarily transported. In Design C, $\Delta c_{\mathrm{IM3}} \approx -8\ \mathrm{gDM/m^3}$ near the bed. This decrease is consistent with the temporal analysis, which also showed lower IM3 concentrations for the larger SPE designs. The spatial concentration field therefore indicates reduced IM3 availability in the lower water column at the Maasmond transect for Designs B2 and C.

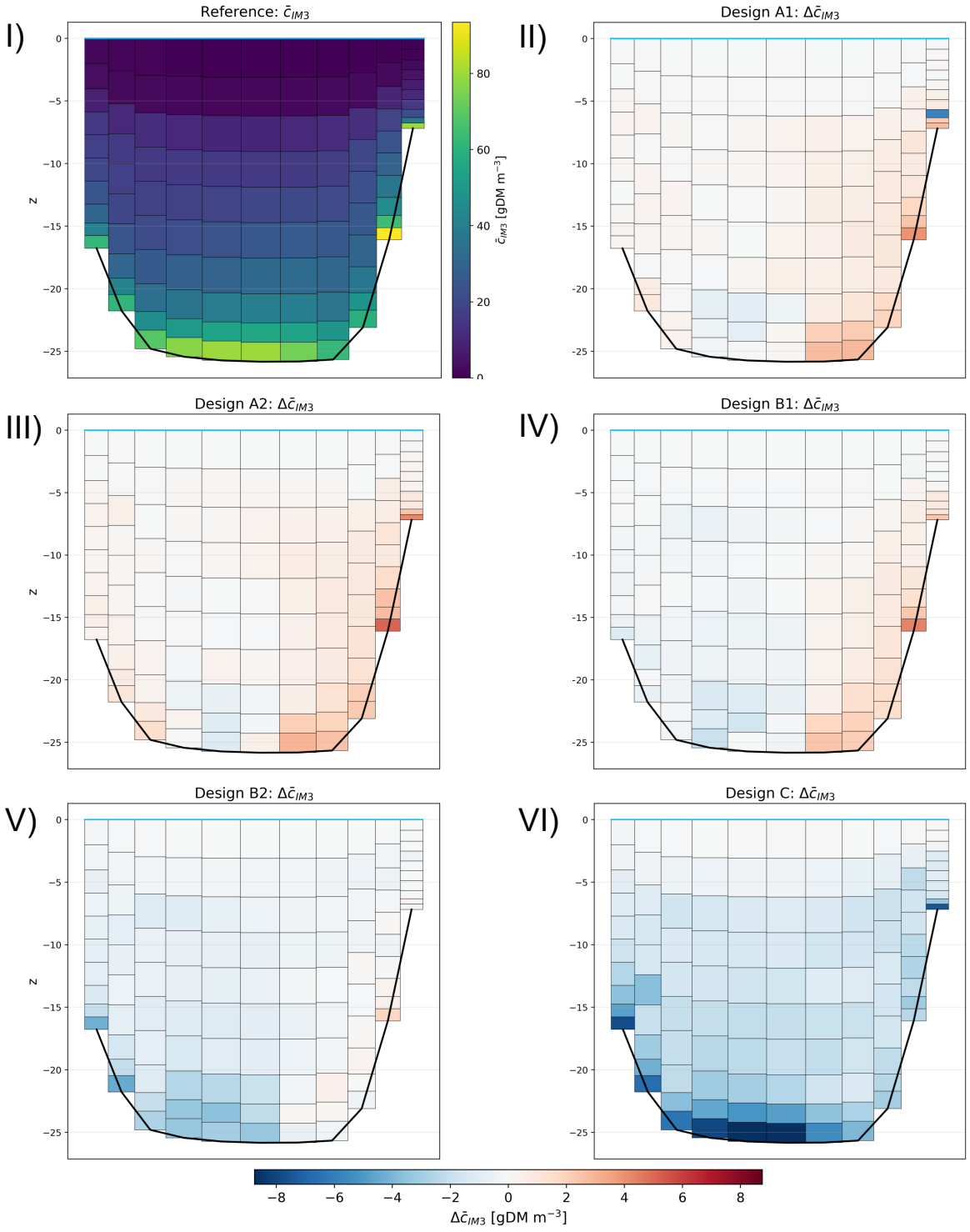

Figure 5.5: Time-averaged suspended IM3 concentration along the Maasmond transect, resolved per grid cell. Panel I shows the Reference scenario ($\bar{c}_{\mathrm{IM3}}$), while Panels II–III show concentration differences relative to the Reference scenario ($\Delta\bar{c}_{\mathrm{IM3}}$) for Designs B1 and C, respectively. The transect is oriented from Hoek van Holland (left) to Maasvlakte (right).

Figure 5.6 shows the corresponding spatial distribution of time-integrated transport (F) and the normalised transport difference, $\Delta F_{\mathrm{IM3,norm}}$. The transport response follows the concentration patterns shown in Figure 5.5. Designs A1, A2, and B1 show only limited local changes, with $\Delta F_{\mathrm{IM3,norm}}$ generally remaining between -0.1% and +0.1%. These differences are too small to identify a clear spatial pattern.

For Designs B2 and C, $\Delta F_{\mathrm{IM3,norm}}$ shows a stronger reduction in the lower water column, indicating reduced transport relative to the Reference scenario. This reduction is strongest for Design C and is concentrated near the bed, where IM3 transport is dominant.

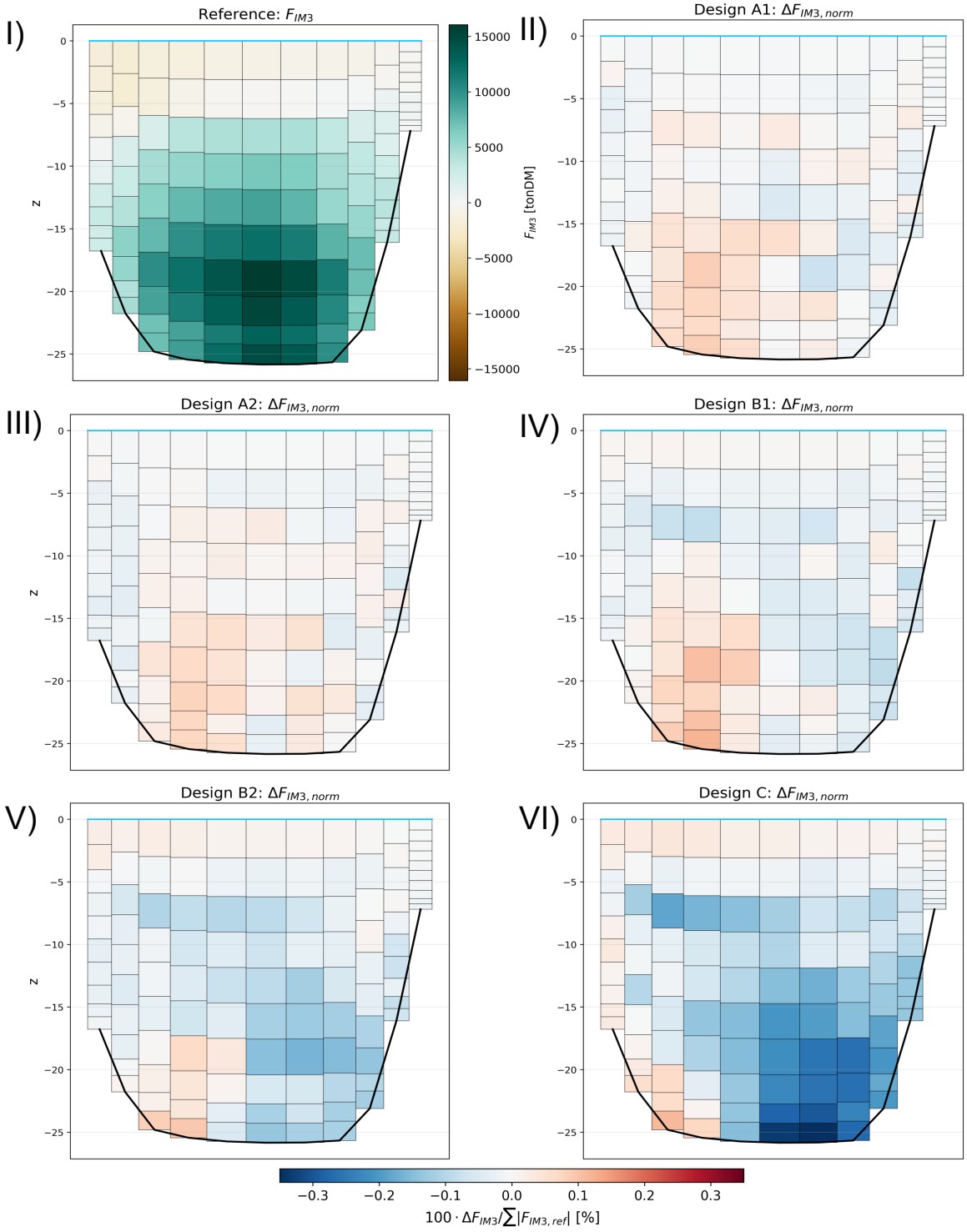

Figure 5.6: Advective IM3 transport along the Maasmond transect, resolved per grid cell. Panel I shows the Reference transport field (F_{IM3}), while Panels II–III show normalised transport differences relative to the Reference scenario ($\Delta F_{\mathrm{IM3,norm}}$) for Designs B1 and C, respectively, as defined in Equation 3.13. The transect is oriented from Hoek van Holland (left) to Maasvlakte (right).

5.3. Synthesis

The transport analysis shows that the SPE designs have limited impact on the transport of IM1 and IM2 through the Maasmond. Relative changes in F_{net}, F_{import}, and F_{export} remain small for these fractions. This is attributed to their low w_s, which limits settling of IM1 and IM2 in the offshore domain and makes their transport less sensitive to local SPE-induced hydrodynamic changes.

IM3 shows the strongest response, particularly for Designs B2 and C, as summarised in Table 5.5. This response contrasts with the initial expectation from the offshore analysis, where increased IM3 redistribution near MV2 was expected to enhance import through the Maasmond.

The temporal analysis shows that the SPE designs have almost no impact on the transect-integrated normal velocity signal, $u_n(t)$. Changes in advective flux are therefore controlled by changes in suspended sediment concentration. For IM3, reductions in suspended sediment concentrations are observed, particularly during flood phases.

The spatial analysis supports this interpretation. For Designs B2 and C, the reduction in IM3 concentration is mainly confined to the lower water column, where IM3 transport is concentrated. The corresponding decrease in $\Delta F_{\mathrm{IM3,norm}}$ occurs near the bed, confirming that reduced IM3 import is driven by lower near-bed sediment availability rather than changes in the flow structure. Designs A1, A2, and B1 show only local and limited concentration changes, which do not produce a substantial change in total IM3 import.

Overall, the SPE designs do not increase fine sediment import through the Maasmond. Instead, the larger designs reduce IM3 import by decreasing suspended IM3 availability at the transect. This indicates that the offshore redistribution identified in Chapter 4 does not translate into increased sediment intake through the Maasmond. The following chapter evaluates how these transport changes affect fine sediment accumulation patterns within the port system.

Table 5.5: Net IM3 transport through the Maasmond transect (F_{net}), with the absolute Reference value and relative SPE-induced changes (Δ).

Fraction	**Reference**	ΔF_{net} [%]				
	[tonDM]	**A1**	**A2**	**B1**	**B2**	**C**
IM3	526,331	+0.52%	+0.35%	-0.91%	-4.17%	-9.00%

6
Results: Port

This chapter presents the fine sediment accumulation response within the port basins. Accumulation is quantified as the change in bed mass, ΔM_{bed}, relative to the Reference scenario, following the methodology described in Section 3.4.3. The resulting bed mass changes are interpreted using changes in bed shear stress ($\overline{\tau}_b$) and suspended sediment concentration ($\overline{c}$), which are used as indicators of erosion and deposition potential.

6.1. Reference scenario

Flow velocities and bed shear stresses are substantially lower inside the port basins than in the offshore domain, as depicted in Figure 6.1. During peak flood, $\overline{u} > 1.0\ \mathrm{m/s}$ along the seaward side of Maasvlakte 2 (MV2) and in the Nieuwe Waterweg, whereas velocities in the Maasvlakte basins remain below $0.4\ \mathrm{m/s}$.

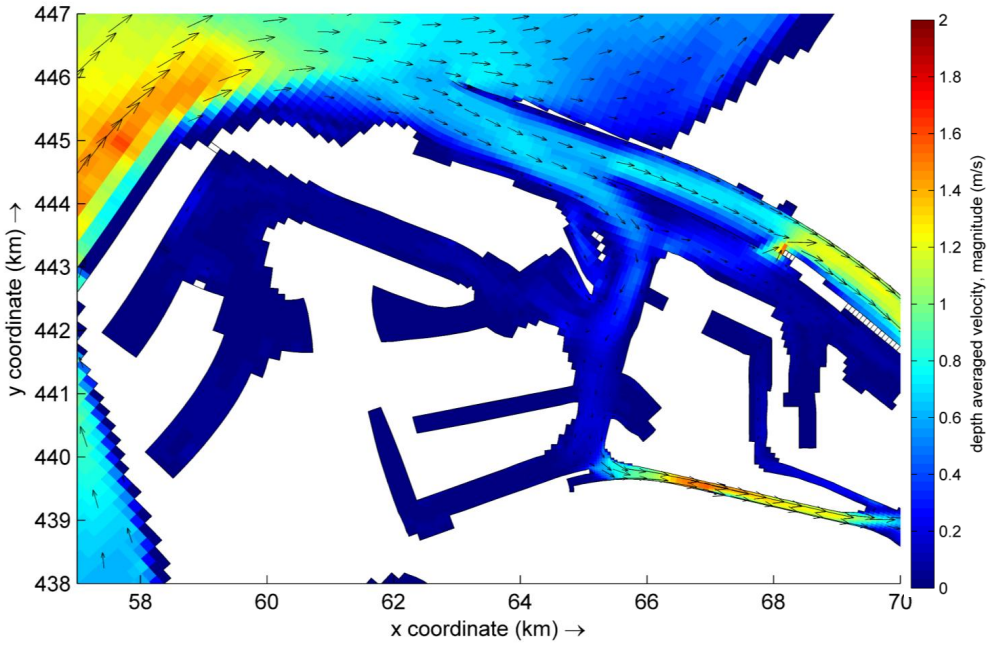

Figure 6.1: Depth-averaged velocity field ($\overline{u}$) in the port area during peak flood conditions.

In the Reference simulation, fractions IM1 and IM2 predominantly accumulate in the harbour basins, where they deposit into the bed (Figure 4.3). Deposition of these fractions mainly occurs in the Maasvlakte basins, the Calandkanaal, and more landward basins such as the Botlek. Due to their low settling velocities (w_s), these fractions accumulate where residence times are sufficiently long and τ_b is low. In the port basins, low flow velocities ($\overline{u} < 0.4\ \mathrm{m/s}$) promote these conditions.

Unlike the finer fractions, IM3 accumulates primarily in the offshore domain in the Reference simulation. Figure 6.2 provides a zoomed-in view of the seaward port basins and shows IM3 bed mass accumulation in layer S_2 at the end of the analysis period ($M_{S2}(t_1)$). Within the port, IM3 accumulation is mainly

confined to the Maasmond, Nieuwe Waterweg, Calandkanaal, and the entrances of the Maasvlakte basins and Beerkanaal.

These IM3 accumulation zones coincide with areas of flow deceleration (Figure 6.1). Further into the port basins, for example in the Prinses Arianehaven, IM3 accumulation remains limited compared to the Maasmond area. This indicates that the relatively high settling velocity of IM3, combined with the local reduction in flow velocity, promotes deposition in the Maasmond and at the entrance of the Beerkanaal.

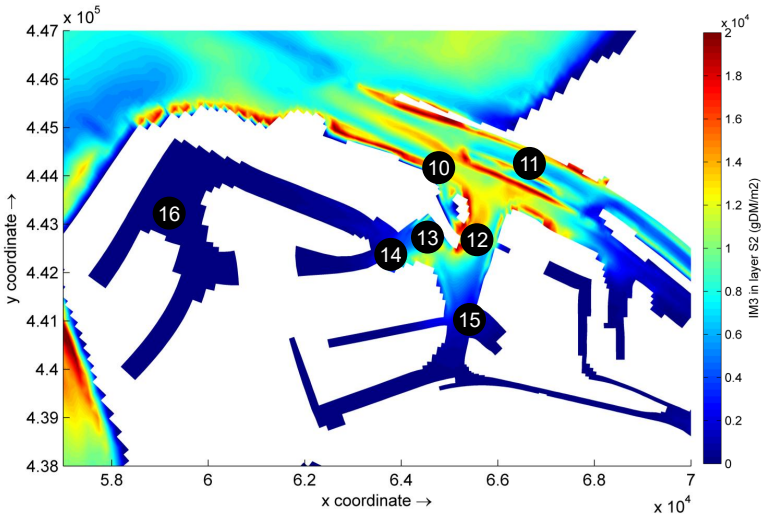

Obs. point	Location
10	Maasmond
11	Nieuwe Waterweg
12	Beerkanaal
13	8th Petroleumhaven
14	Europahaven
15	6th Petroleumhaven
16	Prinses Arianehaven

Figure 6.2: Zoomed-in view of the seaward port basins showing IM3 bed mass accumulation in Layer S_2 at the end of the analysis period ($M_{S2}(t_1)$). Observation points 10–16 are indicated on the map and listed in the accompanying table.

6.2. SPE designs

The observation points used to assess the impact of the SPE designs on sediment accumulation in the port are shown in Figure 6.2. These locations were selected based on initial DELWAQ results and in consultation with the PoR dredging department, with emphasis on areas of operational relevance. The selection excludes basins farther inland in the port system, such as the Botlek basin, where the initial DELWAQ results showed negligible bed mass changes for all IM fractions. Net bed mass change over the analysis period (ΔM_{bed}) is derived as illustrated in Figure 4.6. A complete overview of ΔM_{bed}, Δc, and $\Delta \tau_b$ for all observation points and IM1–IM3 is provided in Appendix E.

For the interpretation of the port accumulation results, relative changes are classified using the same response classes as in Section 5.2.1. Relative changes in a variable, ΔX, are classified as negligible for $|\Delta X| < 1\ \%$, moderate for $1\ \% \leq |\Delta X| \leq 3\ \%$, and pronounced for $|\Delta X| > 3\ \%$. These classes provide a first-order interpretation of the relative changes and are evaluated together with the corresponding absolute values for the Reference. This is particularly relevant for the port analysis, where low Reference values of $\bar{c}$, $\overline{\tau}_b$, and ΔM_{bed} increase the sensitivity of relative changes to small absolute differences. The interpretation therefore focuses on coherent spatial and temporal patterns rather than isolated relative responses.

Table 6.1 presents $\Delta \overline{\tau}_b$ for the SPE designs at the port observation points. From the Reference, it is observed that flow energy decreases towards the inner basins, from $\overline{\tau}_b = 0.33\ \mathrm{N/m^2}$ near the Maasmond to $\overline{\tau}_b = 0.00\ \mathrm{N/m^2}$ in the Prinses Arianehaven. At observation points 13–16, $\overline{\tau}_b \approx 0\ \mathrm{N/m^2}$, indicating negligible resuspension potential and favouring long-term retention of deposited sediment in the bed layers.

For Designs A1–B2, changes in $\overline{\tau}_b$ within the port remain small, ranging from -2.5% to $+1.6\%$. Since $\overline{\tau}_b \approx 0\ \mathrm{N/m^2}$ throughout the inner basins, these changes are expected to have only a minor impact on accumulation patterns. Design C deviates from this response and produces a stronger hydrodynamic change within the port. Here, $\overline{\tau}_b$ increases at observation points 10–15, from the Beerkanaal towards the MV2 basin. This increase is attributed to the additional port basin included in Design C, which

increases the basin volume and modifies the local flow field, resulting in higher local flow velocities. At observation point 16 in the Prinses Arianehaven, $\overline{\tau}_b$ decreases by 6.8%, likely due to modified local circulation patterns caused by the added basin volume. However, since $\overline{\tau}_b \approx 0\ \mathrm{N/m^2}$ at observation points 13–16, the absolute bed shear stress changes in these inner-basin locations remain very small.

Table 6.1: Mean bed shear stress ($\overline{\tau}_b$) for the Reference scenario and SPE-induced relative changes (Δ).

Obs. point	Ref. $\overline{\tau}_b$ [N/m^2]	$\Delta\overline{\tau}_b$ [%]				
		A1	A2	B1	B2	C
10	0.33	-0.5%	-0.6%	-0.8%	-1.1%	+3.9%
11	0.42	+0.2%	+0.4%	+0.5%	+0.9%	+1.2%
12	0.13	+0.0%	-0.2%	-2.1%	-0.6%	+14.9%
13	0.01	+1.1%	-0.3%	-2.5%	-1.1%	+23.0%
14	0.01	+1.5%	+1.6%	+0.0%	+1.3%	+10.1%
15	0.04	-1.4%	-1.9%	-1.1%	-1.0%	+6.9%
16	0.00	+1.4%	+1.6%	+0.2%	+0.8%	-6.8%

Changes in ΔM_{bed} for IM1 are given in Table 6.2. For Designs A1–B2, no pronounced changes in bed mass are observed. Relative changes remain limited, ranging from -2.8% to $+1.5\%$. The corresponding changes in Δc_{IM1}, provided in Appendix E, are also small, ranging from -0.7% to 0.0%. This limited response is consistent with the previous analyses, which showed that IM1 is only weakly affected by the SPE designs. This weak response is therefore also reflected in the accumulation of IM1 within the port.

Table 6.2: Net IM1 bed mass change ($\Delta M_{\mathrm{bed,IM1}}$) for the Reference scenario and SPE-induced relative changes (Δ).

Obs. point	Ref. $\Delta M_{bed,IM1}$ [gDM]	$\Delta M_{bed,IM1}$ [%]				
		A1	A2	B1	B2	C
10	10.4	+0.2%	-0.1%	-0.1%	+0.2%	-2.5%
11	9.8	-0.0%	-0.1%	-0.2%	-0.1%	+0.1%
12	21.9	+0.5%	+1.2%	+1.5%	-0.4%	-20.8%
13	65.6	-0.1%	-0.3%	-0.4%	-0.3%	-0.3%
14	59.3	+0.0%	+0.1%	-0.2%	-0.2%	+0.1%
15	62.2	-0.1%	+0.0%	-0.4%	-0.1%	+0.7%
16	40.7	-2.0%	-2.0%	-2.7%	-2.8%	-18.4%

Changes in ΔM_{bed} for IM2 are given in Table 6.3. For Designs A1–B2, similar to IM1, no pronounced changes in bed mass are observed. The corresponding changes in Δc_{IM2}, provided in Appendix E, typically range between -1% and $+1\%$ at these observation points. This limited response is also consistent with the previous analyses, where IM2 showed only a weak response to the SPE designs. As a result, the accumulation of IM2 within the port remains largely unchanged for Designs A1–B2.

Table 6.3: Net IM2 bed mass change ($\Delta M_{\mathrm{bed,IM2}}$) for the Reference scenario and SPE-induced relative changes (Δ).

Obs. point	Ref. $\Delta M_{bed,IM2}$ [gDM]	$\Delta M_{bed,IM2}$ [%]				
		A1	A2	B1	B2	C
10	163.0	+0.4%	-0.0%	+0.8%	+0.3%	-0.9%
11	150.0	+0.1%	-0.3%	-0.1%	-0.4%	-0.0%
12	297.0	+1.0%	+1.3%	+1.1%	+0.3%	-8.2%
13	1,537.0	+1.1%	+1.3%	+0.8%	+0.3%	-5.8%
14	2,037.0	-0.1%	-0.4%	-0.6%	-0.3%	-9.1%
15	1,190.0	+1.1%	+1.6%	+0.3%	+0.2%	-3.3%
16	821.0	+0.2%	+0.4%	-1.2%	-1.7%	-6.8%

For IM1 and IM2, Design C shows a different bed mass response compared to the other designs. For both fractions, a decrease in ΔM_{bed} is observed across several observation points. This response is attributed to local hydrodynamic changes induced by the additional basin in Design C. Although $\overline{\tau}_b \approx 0\ \mathrm{N/m^2}$ in the inner basins, small absolute changes in bed shear stress can apparently still produce relative changes in bed mass accumulation compared to the Reference. This response is therefore interpreted as a local effect of the additional basin geometry in Design C, rather than as a change in IM1 or IM2 supply from the offshore domain, which was not observed in Chapter 5.

Overall, IM1 and IM2 show no systematic increase in sediment availability within the port basins. A distinct response is limited to Design C, where the extra basin included in the design enhances local hydrodynamic forcing and thereby reduces bed mass accumulation of these fractions. The results presented in Chapters 4 and 5 suggest that the strongest changes in port accumulation are expected for IM3. Figure 6.3 shows the SPE-induced difference in IM3 bed mass in layer S_2 at the end of the simulation, relative to the Reference scenario.

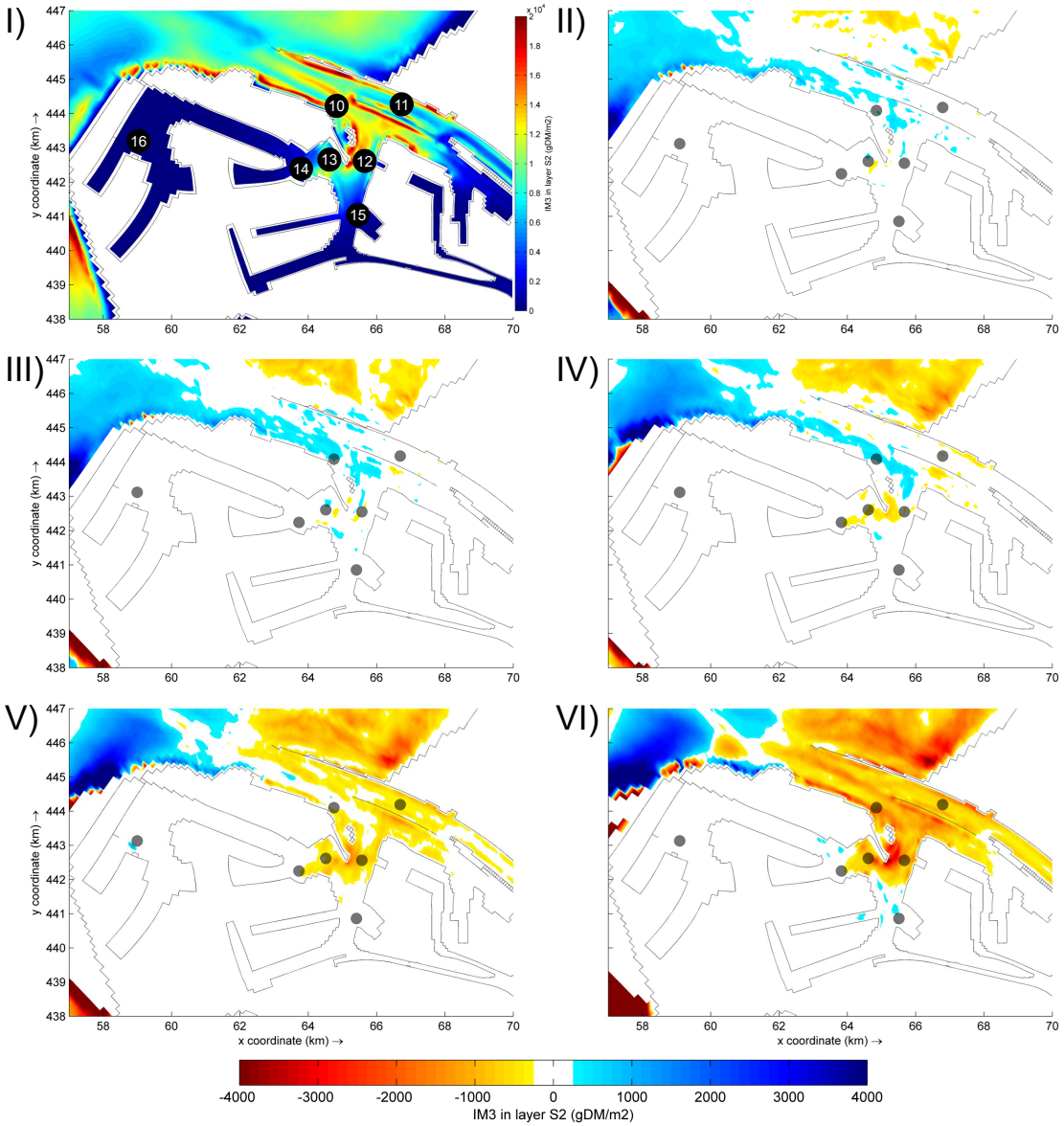

Figure 6.3: IM3 bed mass in Layer S_2 at the end of the DELWAQ simulation. Panel I shows the Reference scenario ($M_{\mathrm{S2,IM3}}(t_1)$), while Panels II–VI show the corresponding bed mass differences relative to the Reference scenario ($\Delta M_{\mathrm{S2,IM3}}(t_1)$) for Designs A1, A2, B1, B2, and C, respectively. Positive values (blue) indicate increased bed mass, while negative values (red) indicate decreased bed mass.

Figure 6.3 shows that, for Designs B2 and C, $\Delta M_{\mathrm{S2,IM3}}(t_1)$ is predominantly negative near the Maasmond and the entrance of the Beerkanaal, indicating reduced IM3 storage in layer S_2. For Designs A1, A2, and B1, the response is weaker and more localised, with positive differences occurring mainly along the northern side of Maasvlakte 2. This local increase in bed mass cannot be attributed to increased IM3 supply, as this was not observed in Chapter 5.

Table 6.4 shows that, in the Reference scenario, $\bar{c}_{\mathrm{IM3}}$ decreases strongly from the Maasmond towards the inner basins, declining from $21.0\ \mathrm{gDM/m^3}$ at the Maasmond to $1.1\ \mathrm{gDM/m^3}$ in the Europahaven. This spatial gradient is consistent with the Reference bed mass distribution shown in Figure 6.2, where IM3 accumulation is concentrated mainly near the Maasmond and the entrance of the Beerkanaal.

Table 6.4: Suspended IM3 concentration ($\bar{c}_{\mathrm{IM3}}$) for the Reference scenario and SPE-induced relative changes (Δ).

Obs. point	Ref. $\bar{c}_{IM3}$ [gDM/m^3]	$\Delta\bar{c}_{IM3}$ [%]				
		A1	A2	B1	B2	C
10	21.0	+1.1%	+2.5%	+1.6%	-1.5%	-9.6%
11	10.6	+0.5%	-0.0%	-1.4%	-3.9%	-8.4%
12	11.5	+1.1%	-0.7%	-0.3%	-5.0%	-8.5%
13	8.4	-0.8%	+0.0%	-2.1%	-7.0%	-3.4%
14	1.1	-2.0%	-2.6%	-5.0%	-3.8%	+21.1%
15	2.7	+1.6%	+4.8%	+1.2%	+1.3%	+3.9%

Note: Observation point 16 is excluded because $\bar{c}_{IM3}$ is approximately zero, resulting in extreme relative differences.

Designs A1, A2, and B1 generally produce only small changes in $\bar{c}_{IM3}$ at observation points 11–13. At observation points 14 and 15, located in the Europahaven and 6th Petroleumhaven, respectively, larger relative changes in $\bar{c}_{\mathrm{IM3}}$ are observed. However, these changes should be interpreted with caution, because absolute IM3 concentrations at these locations are low. At observation point 15, for example, the Reference concentration is only $\bar{c}_{IM3} = 2.7\ \mathrm{gDM/m^3}$, so small absolute differences can produce relatively large percentage changes. Because the corresponding IM3 bed mass in these inner-basin areas is also limited, these changes do not indicate a substantial change in IM3 supply or accumulation.

For Designs B2 and C, $\bar{c}_{IM3}$ decreases at observation points 10–13, indicating reduced IM3 availability in the seaward part of the port. This reduction is consistent over multiple observation points, and agrees with the observed decrease in IM3 import through the Maasmond in Chapter 5. Although an increase is observed at observation points 14–15, the absolute magnitude of these changes is small.

Table 6.5 shows the resulting IM3 bed mass changes at the observation points in the port basin. The clearest pattern that can be observed is the decrease in $\Delta M_{\mathrm{bed,IM3}}$ in the Maasmond and Beerkanaal region for Designs B2 and C. This response can be linked to the reduced IM3 concentrations in this area, which result from the reduced IM3 supply through the Maasmond. Furthermore, this decrease in IM3 bed mass is also persistent over a larger area in the Maasmond and Beerkanaal, as shown in Figure 6.3. For Designs A1, A2, and B1, some bed mass changes are observed, but no consistent pattern in IM3 accumulation can be identified. These changes do not show a persistent trend and cannot be explained by increased or decreased transport into the port, as discussed in Chapter 5. They are therefore attributed to small local differences in the model response.

Table 6.5: Net IM3 bed mass change ($\Delta M_{\mathrm{bed,IM3}}$) for the Reference scenario and SPE-induced relative changes (Δ).

Obs. point	Ref. $\Delta M_{\mathrm{bed},IM3}$ [gDM]	$\Delta M_{\mathrm{bed},IM3}$ [%]				
		A1	A2	B1	B2	C
10	23,999.0	+1.6%	+3.0%	+3.1%	+1.4%	-7.1%
11	8,768.0	-0.9%	-0.4%	-2.3%	-5.3%	-8.5%
12	32,466.0	+0.9%	-0.9%	+1.1%	-6.0%	-25.4%
13	65,377.0	+1.9%	+3.8%	-0.5%	-4.0%	-9.0%
14	11,129.8	-1.8%	-2.2%	-5.1%	-3.6%	+10.1%
15	14,383.0	+3.4%	+8.4%	+1.4%	+3.0%	+7.2%

6.3. Synthesis

The port analysis shows that the SPE designs have no clear effect on bed shear stress within the port area, except for Design C. For this design, flow velocities increase locally within the MV2 basins. This response is attributed to the additional port basin included in Design C, which increases the basin volume and modifies the local flow field.

For IM1 and IM2, no clear SPE-induced changes in accumulation are observed within the port basins, except for the local response associated with Design C. Changes in $\overline{c}_{IM1}$ and $\overline{c}_{IM2}$ remain small, indicating that sediment availability within the port basins is only weakly affected. This is consistent with Chapter 5, where the import of these fractions showed no significant change.

For IM3, the response is more pronounced and depends on design scale. For Designs A1, A2, and B1, some changes in bed mass are observed, but no consistent pattern in IM3 accumulation can be identified. In contrast, Designs B2 and C reduce $\overline{c}_{IM3}$ and $\Delta M_{bed,IM3}$ near the Maasmond and the Beerkanaal entrance. This is consistent with the decrease in IM3 transport identified in Chapter 5. At these locations, the decrease in concentration translates into reduced bed mass accumulation. This reduction in IM3 bed mass extends persistently over a larger area in the Maasmond and Beerkanaal, as shown in Figure 6.3.

7
Discussion

7.1. Interpretation of system response

The goal of this research is to understand how a future Seaward Port Expansion (SPE) could affect maintenance dredging demand for the Port of Rotterdam (PoR) through changes in hydrodynamics and fine sediment transport. This response is traced from the offshore domain, through the Maasmond, and into the port basins. In doing so, this research provides a system-scale assessment of the potential impact of the SPE on maintenance dredging demand.

The interpretation of this response should be viewed in light of the research approach and model limitations described in Section 3.4. The outcomes of the model results are interpreted as independent responses of IM1 (clay), IM2 (fine silt), and IM3 (coarse silt/micro floc) to the SPE designs under regular hydrodynamic conditions, rather than as quantitative predictions of absolute sediment concentrations, bed-level change, or dredging volumes.

As described in Section 3.2, IM3 represents both coarse silt and micro floc through its prescribed settling velocity. For readability, the IM3 response is discussed primarily in terms of coarse silt behaviour, while recognising that this fraction should more generally be interpreted as a combined coarse silt/micro floc fraction.

Conceptual interpretation

Figure 7.1 presents the conceptual framework used to interpret the SPE-induced response in fine sediment dynamics. The SPE designs cause flow contraction around the seaward expansions, thereby increasing local flow velocities and bed shear stresses. The magnitude of this contraction increases for the larger designs, particularly B2 and C. As a result, the existing scour area along Maasvlakte 2 expands and shifts in response to the altered flow field. The SPE-induced scour area moves southwestward towards the seaward tip of the extension, consistent with observations made by Kroon et al. (2025) and Verbruggen et al. (2025). The altered flow regime around the SPE designs has only a limited effect on the clay and fine silt fractions. These fractions remain predominantly in suspension offshore and are therefore less sensitive to the imposed bathymetric changes. Consequently, their transport through the Maasmond and accumulation within the port basins remain largely unchanged, indicating that no change in maintenance dredging demand is expected for these fractions.

The coarse silt/micro floc fraction exhibits a more pronounced response because its higher settling velocity makes it more prone to deposition in the offshore domain, including near Maasvlakte 2. This makes the fraction more sensitive to the altered flow regime imposed by the SPE. The resulting bed mass accumulation and scour response are illustrated in the lower panels of Figure 7.1. In this conceptual figure, the coarse silt response is divided into two cases: Panel I represents the smaller designs, A1–B1, while Panel II represents the larger and less streamlined designs, B2 and C.

For Designs A1–B1, coarse silt is depleted from the SPE-induced scour area and accumulates in the adjacent lee zones, where flow velocities are reduced. This accumulation may result from local redistribution of coarse silt eroded from the scour area, or from enhanced settling of coarse silt that would otherwise be transported along the curvature of Maasvlakte 2. In addition to this bed mass redistribution, the release of fine sediment from the newly formed scour area was estimated. This released volume is limited compared to the annual dredging volumes of the PoR. Together, the smaller and more streamlined designs, A1–B1, do not produce a significant change in coarse silt transport through the Maasmond. Consequently, no change in accumulation of coarse silt within the port basins or in maintenance dredging demand is expected for these designs.

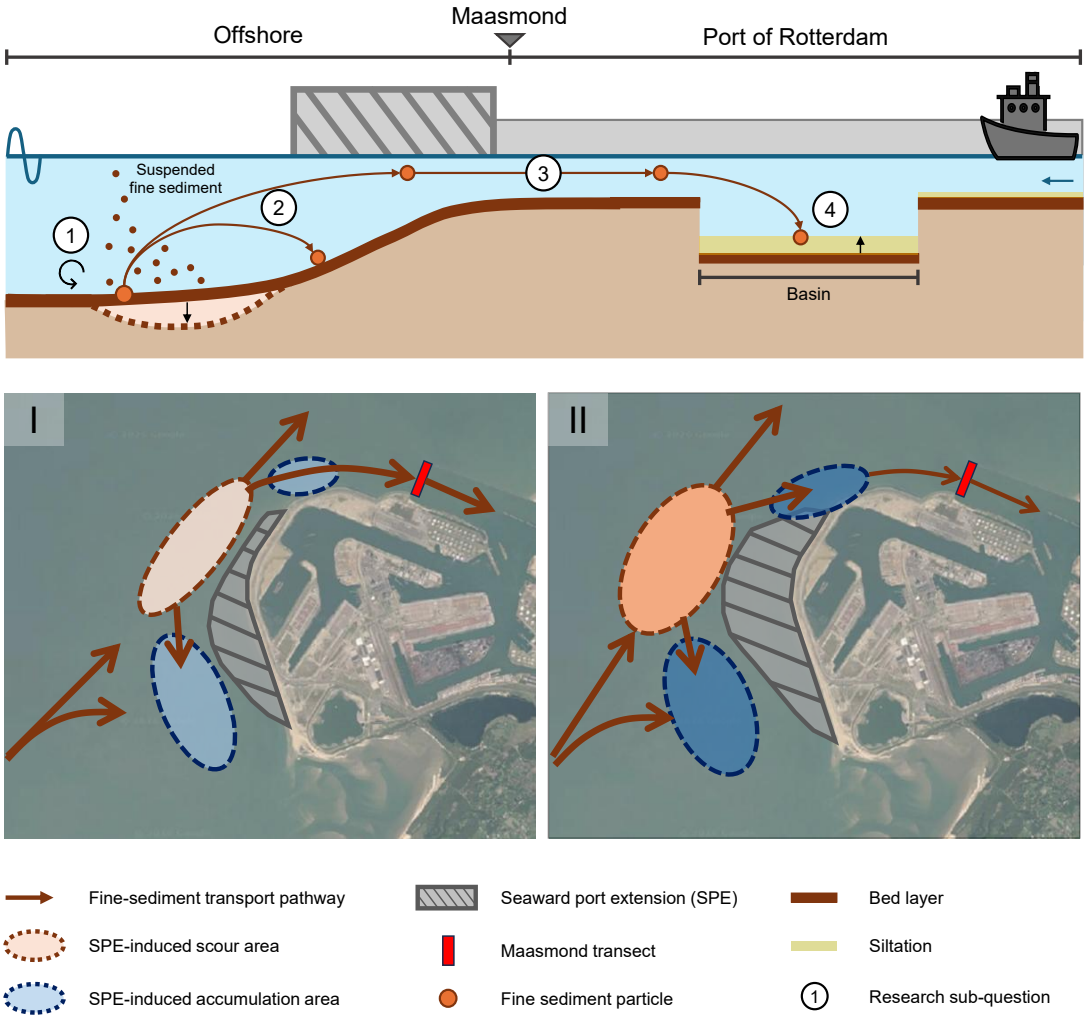

Figure 7.1: Conceptual interpretation of the modelled response of coarse silt to the SPE. The upper panel shows the hypothesis and conceptual framework used to structure the analysis, in which the SPE-induced response of fine sediment dynamics is tracked from the offshore domain, through the Maasmond, and into the port domain; the numbers indicate the corresponding research sub-questions. The lower panel conceptually visualises the interpreted response of coarse silt/microfloc (IM3) to the SPE designs. Panel I shows the response for the smaller designs A1, A2, and B1, where coarse silt is mobilised from the newly induced scour area and transported along the curvature towards the Maasmond, with limited effect on the magnitude of the transport pathway. Panel II shows the general response for the larger designs B2 and C, where increased mobilisation occurs in the intensified scour area and coarse silt accumulates in adjacent zones through decreased flow velocity. As a result, coarse silt that would otherwise be transported along the curvature towards the Maasmond is retained in these accumulation zones, thereby reducing the coarse silt supply to, and transport through, the Maasmond. The stronger colour intensity in Panel II indicates the more pronounced scour and accumulation response for the larger designs.

The larger and less streamlined designs, B2 and C, produce a different response in coarse silt/micro floc dynamics. Although the estimated release of new fines from the scour area remains small compared to the annual dredging volumes of the PoR, these larger designs increase the accumulation potential of coarse silt in the low-energy zones adjacent to the scour area. This enhances the retention of coarse silt in the offshore domain. Coarse silt that would otherwise be advected along the curvature of Maasvlakte 2 tends to settle in these low-energy zones due to the reduced flow velocities induced by the larger designs. As a result, less coarse silt is transported towards the Maasmond. This effect reduces the supply of coarse silt to the port and limits the material available for accumulation within the port basins. The decrease in coarse silt accumulation is mainly observed near the Maasmond and the Beerkanaal. This decrease in coarse silt supply may therefore reduce the maintenance dredging demand associated with this fraction for the PoR.

Model-based support for the interpretation

This interpretation of the system response is supported by the model results across the three analysed domains: the offshore domain, transport through the Maasmond, and accumulation within the port basins.

Clay and fine silt

For IM1 (clay) and IM2 (fine silt), the results show a limited response in offshore bed mass accumulation across all SPE scenarios, as shown in Chapter 4. Both fractions remain relatively well distributed throughout the water column. Clay behaves as a wash-load fraction, while fine silt shows only a weak vertical concentration gradient. Substantial settling and accumulation of these fractions therefore occur mainly in the low-energy port basins, where flow velocities are low and residence times are longer. Although the SPE designs affect offshore flow patterns and bed shear stresses, clay and fine silt remain predominantly in suspension offshore and are therefore only weakly affected by the imposed hydrodynamic changes.

This limited response of clay and fine silt is reflected in the transport of these fractions through the Maasmond, as analysed in Chapter 5. Since the SPE designs have no significant effect on the horizontal velocity profile at the Maasmond, changes in fine sediment transport are primarily governed by changes in concentration and therefore sediment supply. For clay and fine silt, changes in import through the Maasmond remain smaller than 1% across all designs. The control transect therefore confirms the behaviour observed in the offshore domain: clay and fine silt show only a limited response to the changed coastal geometry imposed by the SPE.

The accumulation response of clay and fine silt within the port basins, analysed in Chapter 6, is consistent with the transport response described above. Since no systematic change in clay or fine silt import through the Maasmond is observed, no substantial change in port-basin accumulation is expected. This is reflected in the bed mass changes of both fractions, which remain smaller than 3% for Designs A1–B2. Together with the differences in clay and fine silt concentration, which are typically smaller than 1%, these results confirm that the SPE does not increase clay or fine silt accumulation through enhanced sediment supply. Only Design C shows a pronounced decrease in clay and fine silt accumulation. This decrease is attributed to the additional basin included in Design C, which locally increases flow velocities and reduces accumulation, rather than to changes in offshore sediment supply or transport through the Maasmond.

Taken together, the analyses across the three domains, offshore response, Maasmond transport, and port-basin accumulation, indicate that the SPE has no significant effect on clay and fine silt dynamics under regular hydrodynamic conditions.

Coarse silt/micro floc

For IM3 (coarse silt/micro floc), the offshore bed mass results presented in Chapter 4 show that the hydrodynamic changes induced by the SPE have a more pronounced effect on accumulation, because this fraction is more prone to settling in the offshore domain. In the area towards which the SPE-induced scour zone shifts, coarse silt accumulation decreases, while accumulation increases in the adjacent lee zones. The magnitude of this bed mass depletion and adjacent accumulation increases with design size. This offshore accumulation pattern is consistent with observations by Hendriks et al. (2020), who reported increased fine sediment accumulation after the construction of Maasvlakte 2, particularly on the southern side of Maasvlakte 2 (Figure 2.3).

For Design C, for example, the mean bed shear stress decreases from $1.18\ \mathrm{N/m^2}$ to $0.78\ \mathrm{N/m^2}$ in the northern accumulation zone, and from $0.23\ \mathrm{N/m^2}$ to $0.12\ \mathrm{N/m^2}$ south of Maasvlakte 2. The larger and less streamlined designs therefore create more pronounced low-energy zones adjacent to the scour area, increasing the local retention potential of coarse silt.

Although the model results show a distinct pattern of coarse silt depletion and adjacent accumulation, the estimated release of new fines from the SPE-induced scour area remains small. Even under conservative assumptions, the additional dredging volume associated with these newly released fines remains below $0.1\ \mathrm{Mm^3/yr}$, corresponding to less than 1% of the annual maintenance dredging volume of the Port of Rotterdam. This limited contribution mainly results from the low fine sediment content of the eroded bed material, which is < 1%. The main implication of the offshore response is therefore not that

the scour area acts as a substantial new fine sediment source. Instead, changes in transport pathways and accumulation patterns are interpreted as the main drivers of changes in coarse silt transport.

The effect of offshore coarse silt redistribution is most clearly reflected in the Maasmond transport analysis presented in Chapter 5. This analysis highlights the contrast between the smaller designs, A1–B1, and the larger, less streamlined designs, B2 and C. For the smaller designs, changes in net coarse silt transport remain limited, with differences relative to the Reference smaller than 1%. For Designs B2 and C, however, net coarse silt import decreases by 4% and 9%, respectively. This reduction is not driven by a change in the velocity profile at the Maasmond. Instead, it results from a decrease in coarse silt supply in the lower water column, where the saline inflow would normally advect coarse silt into the port system. The reduced supply is attributed to increased offshore retention of coarse silt in the lee zones created by the larger designs.

The reduced inflow of coarse silt is also reflected in the accumulation response within the port basins (Chapter 6). In areas where coarse silt settles in the Reference scenario, particularly in the Maasmond and Beerkanaal, Designs B2 and C show reduced accumulation and lower bed mass. The decrease in bed mass is typically larger than 5% in the Maasmond area and near the entrance of the Beerkanaal. For the smaller designs, A1–B1, no clear spatial pattern or systematic change is observed, which is consistent with the limited change in coarse silt transport through the Maasmond for these scenarios.

Taken together, the analyses across the three domains (offshore response, Maasmond transport, and port-basin accumulation) indicate that the SPE-induced change in coarse silt dynamics is not primarily driven by the release of additional fines from the newly formed scour area. Instead, the dominant mechanism is the modification of flow patterns around the expansions, which increases offshore retention of coarse silt that would otherwise remain available for advection towards the port system. For the smaller and more streamlined designs, A1–B1, this mechanism does not result in a significant change in coarse silt import through the Maasmond. For the larger and less streamlined designs, B2 and C, increased offshore retention reduces coarse silt import and may therefore decrease port-basin accumulation and maintenance dredging demand for this fraction.

However, as noted earlier, the implications of these results should be interpreted in light of the underlying assumptions, simplifications, and limitations of the research approach and numerical model set-up. These are discussed in the next section.

7.2. Research limitations

The fine sediment response to the SPE designs is interpreted in light of assumptions and simplifications in the research approach and model set-up, and sediment parametrisation. These limitations affect the conclusions that can be drawn and indicate where future research is required.

1) Exploratory character of the research
This research should be interpreted as an exploratory assessment of the potential impact of SPE designs on fine sediment dynamics in the Port of Rotterdam system. The SPE designs represent future scenarios, so the simulated response cannot be validated against observed post-construction conditions. In addition, no other studies have yet assessed the impact of these designs on fine sediment transport and accumulation in the Port of Rotterdam, which limits opportunities for direct comparison.

The conceptual framework builds on the approach used by Hendriks et al. (2020) to analyse the impact of human interventions on the distribution of fines along the Holland Coast, but adapts it to the objectives of the present study and the available model output. This results in a study-specific framework for interpreting the SPE-induced response. In addition, the model applies constant fine sediment concentrations at the boundaries. Consequently, the model outcomes should be interpreted as relative response patterns of the individual fine sediment fractions, rather than as absolute predictions of SPM concentrations, mass accumulation, or maintenance dredging volumes. Despite these simplifications, the approach does provide a consistent basis for comparing the SPE scenarios using semi-quantitative indicators of hydrodynamics, sediment transport, and accumulation potential.

2) Scope of simulated conditions
The model is forced with representative hydrodynamic conditions and does not include storm events or other episodic high-energy conditions. This limits the interpretation of offshore coarse silt retention, because storm-driven remobilisation can contribute substantially to the import of marine fines into the Port of Rotterdam (Verlaan et al. 2000). Coarse silt retained offshore by Designs B2 and C under regular hydrodynamic conditions may therefore be remobilised during energetic events and subsequently advected towards the Maasmond and port basins.

This research also represents a system with a completed SPE geometry. Construction-phase effects, including sand mining, reclamation works, dredging activities, and other construction-related disturbances, are not included. These processes, especially overflow during sand mining, are known to introduce fine sediment into the system, as observed for Maasvlakte 2 (Berkenbosch et al. 2006; Hendriks et al. 2020). The study therefore isolates the effect of the changed coastal geometry, but does not represent the full disturbance associated with the construction and operation of a future SPE. Operational processes such as shipping-induced bed shear stresses, maintenance dredging within the port basins, and relocation of dredged material to disposal sites such as the Verdiepte Loswal are also outside the research scope.

3) Representation of fine sediment
The results of this study should be interpreted as fraction-specific responses to the implementation of the SPE designs. They should not be interpreted as a complete representation of natural cohesive-sediment dynamics in the port, because several processes are simplified in the model set-up.

Fine sediment consists of particles smaller than $63\ \mu\mathrm{m}$, including silt (2–$63\ \mu\mathrm{m}$) and clay ($< 2\ \mu\mathrm{m}$) (Winterwerp et al. 2004). In natural systems, these particles occur as a continuous distribution of particle and floc sizes, with flocculation controlling the effective settling velocity and sedimentation rate (Bruens 1999). In the model set-up used in this research, this continuous range is simplified into three Inorganic Matter (IM) fractions: IM1 (clay), IM2 (fine silt), and IM3 (coarse silt/micro floc). These fractions are distinguished by their prescribed settling velocity, w_s.

Flocculation effects are therefore represented implicitly through the assigned settling velocities. Dynamic flocculation processes, including aggregation, break-up, and exchange between fractions, are not resolved. Instead, the IM fractions are modelled as independent sediment classes. Additional bed-exchange processes, such as armouring and washing-out of fine material, are also simplified or not explicitly resolved. Furthermore, no spatial differentiation in bed composition is applied, although bed composition is known to differ between the offshore domain, waterways, and port basins (Rijn et al. 2007; De Nijs et al. 2009).

4) DELWAQ boundary forcing
The DELWAQ simulations use constant boundary concentrations for the IM fractions. This enables a controlled relative comparison between the Reference scenario and the SPE scenarios, which is appropriate for the exploratory character of this research. Because DELWAQ and the Buffer module respond linearly to the imposed boundary concentrations, this allows for the analysis to be based on relative differences. However, constant boundary concentrations do not represent realistic, time-varying SPM forcing from the Dutch coastal system (Suijlen et al. 2002; Van Der Hout et al. 2015). In addition, the relative abundance of IM1, IM2, and IM3 is not prescribed. The individual IM fractions therefore cannot be combined into a physically meaningful Total Inorganic Matter (TIM) signal. As a result, this study cannot draw conclusions on absolute SPM concentrations or TIM dynamics. The interpretation is limited to the relative response of the individual IM fractions.

5) Morphodynamic development
The model set-up (DELWAQ) does not include morphodynamic feedback or bed-level updating (Deltares 2025a). Accumulated sediment mass therefore does not modify the bed level or feed back into the local flow conditions. This limitation is most relevant near the scour and accumulation zones, where the model indicates redistribution and retention of coarse silt.

Under fixed-bed conditions, continued accumulation in the low-energy zones adjacent to the scour area may be overestimated. The offshore retention mechanism identified for coarse silt should therefore be interpreted as accumulation potential, rather than as long-term bed-level evolution. Morphodynamic feedback could also weaken the simulated reduction in coarse silt supply towards the Maasmond for the larger SPE designs, B2 and C. If bed-level updating were included, accumulation in lower-energy zones would modify the local flow field over time, potentially reducing further deposition of coarse silt in that area. Part of the retained coarse silt could then become available again for transport towards the Maasmond, dispersing the effect that these accumulation zones have on the system over time.

6) Sensitivity to fine sediment parameters
Uncertainty remains in the parameters controlling fine sediment transport, deposition, and bed exchange, of which settling velocity (w_s) proved to be the most relevant in this study. Since IM1 and IM2 show limited responses to the SPE designs, whereas IM3 shows the strongest response, sensitivity analysis should focus primarily on settling velocities in the range of IM3. Testing alternative values of w_s within that range would help assess the robustness of the interpretation of the SPE-induced response in coarse silt/micro floc dynamics.

The most relevant sensitivity range would be between the settling velocities currently assigned to IM2 and IM3. Intermediate values within this range would represent silt fractions that settle sufficiently fast to be affected by SPE-induced changes in the offshore domain, while remaining suspended long enough to be transported towards the Maasmond and into the port basins. These fractions are therefore most relevant for assessing potential changes in maintenance dredging demand for the PoR. For example, additional simulations with $w_s = 40\ \mathrm{m/day}$ and $w_s = 60\ \mathrm{m/day}$ could be used to represent such intermediate silt fractions and assess the robustness of the observations made in this study.

7) Implications for interpretation
Despite these limitations and simplifications, this research provides a basis for interpreting how individual fine sediment fractions may respond to a completed SPE under regular hydrodynamic conditions, excluding construction-phase effects. The hydrodynamic response can be interpreted with relatively high confidence, as the OSR-NSC Delft3D-FLOW model has been extensively calibrated and validated (Kranenburg 2015a; Kranenburg 2015b). The results show clear flow contraction around the SPE designs, while the velocity profile through the Maasmond and the internal port hydrodynamics remain largely unaffected.

For the fine sediment results, the uncertainty range cannot be quantified, because the modelled response cannot be validated against observed SPE conditions or comparable previous studies. However, the use of relative differences between the Reference and SPE scenarios reduces the sensitivity to systematic model bias. In addition, the analysis is based on variables averaged over multiple spring–neap cycles, which reduces the influence of short-term variability or outliers. By tracing the fine sediment response across the offshore domain, the Maasmond, and the port basins, the study provides a coherent system-scale interpretation of the modelled particle behaviour.

7.3. Recommendations

Building on the interpreted system response and the limitations of the modelling approach, several recommendations are made for future research:

- **Test the sensitivity of the coarse silt response to settling velocity**
  As discussed in Section 7.2, the robustness of the modelled coarse silt/micro floc response should first be assessed by testing alternative settling velocities (w_s). Additional simulations with, for example, $w_s = 40\,\mathrm{m/day}$ and $w_s = 60\,\mathrm{m/day}$ would help determine whether the offshore retention mechanism and reduced coarse silt import through the Maasmond remain robust. This can be done relatively efficiently, as the model set-up of this study can be reused.
- **Assess morphodynamic development and storm-driven remobilisation of coarse silt**
  After the robustness of the coarse silt response has been assessed, future research should examine the morphodynamic development around the SPE-induced scour and accumulation zones. A model set-up with bed-level updating, for example using Delft3D-Sediment, as applied in PRISMA, would clarify whether offshore retention of coarse silt for Designs B2 and C persists over time. It would also provide insight into the volume, depth, and spatial extent of the SPE-induced scour area, including potential implications for the structural integrity of the SPE designs.

  If persistent coarse silt accumulation develops in these zones, the same model set-up could be used to assess storm-driven remobilisation. Although the larger SPE designs reduce coarse silt transport towards the Maasmond under regular hydrodynamic conditions, retained sediment north of Maasvlakte 2 may be resuspended during storm events and advected towards the port basins (Verlaan et al. 2000). This could lead to high peaks in siltation rates and is therefore directly relevant for maintenance dredging operations in the Port of Rotterdam.
- **Analyse the impact of Design C on fine sediment dynamics in the Maasvlakte basins**
  If Design C is considered for further development, its impact on hydrodynamics and fine sediment accumulation within the Maasvlakte basins should be assessed in more detail. Due to the additional basin included in this design, Design C locally increases bed shear stress in the Maasvlakte basins, particularly near the Beerkanaal entrance and in the 8th Petroleumhaven. Although the absolute changes in flow velocities remain low, the analysis in Chapter 6 does show pronounced local changes in bed mass accumulation. These changes may affect the mobilisation of fluid-mud deposits in this region (Kirichek et al. 2021), making them directly relevant for maintenance dredging operations in the Port of Rotterdam.
- **Assess the impact of offshore fine sediment redistribution near Natura 2000 areas**
  The SPE designs affect fine sediment dynamics in the offshore domain, but this study focused mainly on their implications for transport through the Maasmond and accumulation within the port basins. Effects on the coastal zone south of Maasvlakte 2, towards Rockanje, were not analysed in detail. This area contains the Natura 2000 sites Voornes Duin and Duinen Goeree (Rijksoverheid 2026b; Rijksoverheid 2026a), where ecological conditions may be sensitive to changes in suspended particulate matter. The potential impact of SPE-induced fine sediment dynamics on these protected coastal areas should therefore be included in the environmental impact assessment of future SPE designs.
- **Assess construction-phase fine sediment release**
  This research isolates the effect of the completed SPE geometry and indicates that the coastline change itself does not increase fine sediment import into the Port of Rotterdam under regular hydrodynamic conditions. Future research should therefore focus primarily on construction-related processes that affect fine sediment dynamics during SPE development, such as sand mining, reclamation works, overflow losses, dredging activities, and other seabed disturbances (Berkenbosch et al. 2006). A first-order assessment of potential future sand mining locations for an SPE would already be a valuable step towards reducing fine sediment impacts in the port. Strategic positioning of these pits could reduce the likelihood that released fines are transported towards the Maasmond and into the port basins.

8
Conclusion

This research aimed to assess how alternative Seaward Port Expansion (SPE) designs, implemented as direct extensions of Maasvlakte 2, could affect maintenance dredging demand in the Port of Rotterdam through changes in hydrodynamics and fine sediment transport. To this end, a process-based framework was established to describe fine sediment dynamics, and a numerical modelling sequence was applied to simulate the hydrodynamic and fine sediment response. The main research question was:

How do alternative seaward port expansion (SPE) designs affect maintenance dredging demand in the Port of Rotterdam through changes in hydrodynamics and fine sediment transport?

This question was addressed through four research sub-questions:

1) How do SPE designs influence flow velocity fields and bed shear stress offshore?

The SPE designs alter offshore hydrodynamic forcing by causing flow contraction around the seaward expansions, which increases local flow velocities and bed shear stresses. The magnitude and spatial extent of this response increase with design scale. As a result, the zone of maximum hydrodynamic forcing shifts southwestward from the present Maasvlakte 2 scour area. Lower-energy zones develop next to this higher-energy scour-prone area. In these zones, flow velocities and bed shear stresses are reduced relative to the Reference scenario.

2) How do SPE designs influence the spatial redistribution of fine sediment offshore, including the formation of an erosion pit?

The offshore sediment response depends strongly on the fine sediment class. Clay and fine silt show limited sensitivity to the imposed bathymetric changes because they remain predominantly in suspension offshore and show limited settling near the SPE designs.

The coarse silt/micro floc fraction shows a more pronounced response, as this fraction is prone to settling in the offshore domain, including near the SPE designs. For this fine sediment class, bed mass decreases in the scour-prone zone near the extensions, while accumulation increases in adjacent low-energy lee zones. This redistribution pattern becomes more pronounced with increasing design scale. However, the estimated release of new fines from the scour area is small. Even under conservative assumptions, the additional volume would amount to at most $0.1\ \mathrm{Mm}^3/\mathrm{yr}$, corresponding to approximately 1% of the annual maintenance dredging volume of the Port of Rotterdam. Changes in accumulation of fines in the port are therefore primarily driven by changes in fine sediment transport pathways, rather than by the release of new fines from the scour area.

3) How do the SPE designs change fine sediment transport through the Maasmond transect?

The SPE designs have limited impact on the velocity profile through the Maasmond. Changes in fine sediment transport through this control transect are therefore mainly driven by changes in sediment supply. For clay and fine silt, differences in transport between the SPE scenarios and the Reference remain small, with relative changes smaller than 1%. This is consistent with the limited offshore response of these fractions to the SPE designs.

For the coarse silt/micro floc fraction, a distinction emerges between the smaller designs, A1, A2, and B1, and the larger designs, B2 and C. For the smaller designs, transport through the Maasmond remains close to the Reference scenario, with relative differences in net transport smaller than 1%. For Designs B2 and C, however, net transport through the Maasmond decreases by 4% and 9%, respectively. This decrease results from reduced coarse silt/micro floc supply in the lower water column, where this fraction is transported into the port system by saline inflow. For the larger designs, the reduced supply of coarse silt/micro floc is attributed to increased offshore retention in the lower-energy zones induced by the extension.

4) How do SPE designs alter fine sediment accumulation within the port waterways and basins, and what do these changes imply for maintenance dredging?

The SPE designs have limited effect on clay and fine silt accumulation within the port waterways and basins, consistent with the limited changes in transport through the Maasmond. For coarse silt/micro floc, the response depends on design scale. For the smaller designs, A1, A2, and B1, no significant change in port-basin accumulation is observed. For the larger designs, B2 and C, reduced import through the Maasmond leads to lower coarse silt/micro floc accumulation within the port system, particularly in the Maasmond and near the Beerkanaal entrance. Consequently, Designs B2 and C may even decrease the maintenance dredging demand associated with this fraction.

Overall, this research shows that the coastline-geometry change associated with the implementation of the SPE does not lead to an increase in marine fine sediment import into the Port of Rotterdam under regular hydrodynamic conditions. For Designs B2 and C, increased offshore retention of coarse silt/micro floc reduces import through the Maasmond and may therefore decrease the maintenance dredging demand associated with this fraction. Within the applied model set-up and excluding storm events, morphodynamic feedback, and construction-phase effects, the SPE designs are therefore not expected to increase maintenance dredging demand through changes in hydrodynamics and fine sediment transport.

References

Berkenbosch, R., J. Meulepas, L. Brouwer, M. van Ledden, F. Heinis, C. Vertegaal, M. van Zanten, and H. de Mars (Sept. 2006). *Milieueffectrapport Aanleg Maasvlakte 2 Hoofdrapport*. Tech. rep. Nijmegen: Royal Hasknoning, p. 454.

Boer, S., E. Elias, S. Aarninkhof, D. Roelvink, and T. Vellinga (2007). "Large-Scale Scour of the Sea Floor and the Effect of Natural Armouring Processes, Land Reclamation Maasvlakte 2, Port of Rotterdam". In: *Coastal Sediments '07*, pp. 598–611. DOI: 10.1061/40926(239)45.

Bosboom, J. and M. J. Stive (Jan. 2023). *Coastal dynamics*. TU Delft OPEN Publishing. DOI: 10.5074/t.2021.001.

Bruens, A. (Jan. 1999). "Transport of cohesive sediments: Classification and requirements for turbulence modelling". In: *Data Archiving and Networked Services (DANS)*.

Bruijn, L. (2018). "Maintenance Dredging in the Port of Rotterdam". MSc Thesis. Delft: Delft University of Technology.

Clark, M. (Jan. 2009). *Transport Modeling for Environmental Engineers and Scientists, Second Edition, ISBN: 978-0-470-26072-2*. John Wiley and Sons.

Cox, J. R., Y. Huismans, S. M. Knaake, J. R. F. W. Leuven, N. E. Vellinga, M. Van Der Vegt, A. J. F. Hoitink, and M. G. Kleinhans (June 2021). "Anthropogenic effects on the contemporary sediment budget of the Lower Rhine Meuse Delta Channel Network". In: *Earth s Future* 9.7. DOI: 10.1029/2020ef001869.

Cronin, K., Y. Huismans, and T. Van Kessel (Oct. 9, 2019). *Local Mud Dynamics and Sedimentation around the Maasmond*. 11202804–000. Delft: Deltares, p. 33.

De Boer, G. J., J. D. Pietrzak, and J. C. Winterwerp (Jan. 2009). "SST Observations of Upwelling Induced by Tidal Straining in the Rhine ROFI". In: *Continental Shelf Research* 29.1, pp. 263–277. DOI: 10.1016/j.csr.2007.06.011.

De Nijs, M. A. J., J. D. Pietrzak, and J. C. Winterwerp (Jan. 1, 2011). "Advection of the Salt Wedge and Evolution of the Internal Flow Structure in the Rotterdam Waterway". In: *Journal of Physical Oceanography* 41.1, pp. 3–27. DOI: 10.1175/2010JPO4228.1.

De Nijs, M. A. J., J. C. Winterwerp, and J. D. Pietrzak (Apr. 2010). "The effects of the internal flow structure on SPM entrapment in the Rotterdam Waterway". In: *Journal of Physical Oceanography* 40.11, pp. 2357–2380. DOI: 10.1175/2010jpo4233.1.

De Nijs, M. A. and J. D. Pietrzak (June 2012). "Saltwater Intrusion and ETM Dynamics in a Tidally-Energetic Stratified Estuary". In: *Ocean Modelling* 49–50, pp. 60–85. DOI: 10.1016/j.ocemod.2012.03.004.

De Nijs, M. A., J. C. Winterwerp, and J. D. Pietrzak (Jan. 2009). "On Harbour Siltation in the Fresh-Salt Water Mixing Region". In: *Continental Shelf Research* 29.1, pp. 175–193. DOI: 10.1016/j.csr.2008.01.019.

De Wit, L. and L. Jaksic (Nov. 2022). *Gel Barriers in the Port of Rotterdam*. Rapport Deltares. Delft: Deltares, p. 52.

Deltares (Nov. 2025a). *Delft3D FM Suite 2D3D D-Water Quality. User Manual*. Deltares. Delft.

— (Oct. 2025b). *Delft3D-FLOW User Manual. User Manual*. Deltares. Delft.

Dronkers, J. (1986). "Tidal asymmetry and estuarine morphology". In: *Netherlands Journal of Sea Research* 20.2, pp. 117–131. DOI: https://doi.org/10.1016/0077-7579(86)90036-0.

Fischer, H. (1972). "Mass transport mechanisms in partially stratified estuaries". In: *Journal of Fluid Mechanics* 53.4, pp. 671–687. DOI: 10.1017/S0022112072000412.

Flores, R. P., S. Rijnsburger, A. R. Horner-Devine, N. Kumar, A. J. Souza, and J. D. Pietrzak (2020). "The Formation of Turbidity Maximum Zones by Minor Axis Tidal Straining in Regions of Freshwater Influence". In: *Journal of Physical Oceanography* 50.5, pp. 1265–1287. DOI: 10.1175/JPO-D-18-0264.1.

Franca., M. J. and C. Juez (Dec. 1, 2019). "Fine Sediments: Transport in Suspension, Storage and Supply". IRSTEA Lyon-Villeurbanne. Conference.

Geyer, W. R. (1993). "The Importance of Suppression of Turbulence by Stratification on the Estuarine Turbidity Maximum". In: *Estuaries* 16.1, pp. 113–125. DOI: 10.2307/1352769.

Hendriks and De Wit (Aug. 2025). *Executive Summary TKI Prisma 3*. Tech. rep. Delft: Deltares.

Hendriks, H., B. Van Prooijen, S. Aarninkhof, and J. Winterwerp (June 2020). "How human activities affect the fine sediment distribution in the Dutch Coastal Zone seabed". In: *Geomorphology* 367, p. 107314. DOI: 10.1016/j.geomorph.2020.107314.

Hoffmans, G. J. C. M. and H. J. Verheij, eds. (2021). *Scour Manual. Current-Related Erosion*. 1st ed. CRC Press. DOI: 10.1201/b22624.

Jay, D., P. Orton, T. Chisholm, D. Wilson, and A. Fain (Dec. 2007). "Particle trapping in stratified estuaries: Application to observations". In: *Estuaries and Coasts* 30, pp. 1106–1125. DOI: 10.1007/BF02841400.

Kirichek, A., K. Cronin, L. De Wit, E. Meshkati, D. Van Keulen, and J. Terwindt (2021). *PRISMA I: Final report*. Deltares.

Kirichek, A., R. Rutgers, M. Wensveen, and A. van Hassent (2018). "Sediment management in the Port of Rotterdam". In: *Baggern–Unterbringen–Aufbereiten–Verwerten: 10. Rostocker Baggergutseminar, Kompetenztreffpunkt Nassbaggergut: Tagungsband* (Universität Rostock, Sept. 11–12, 2018).

Kranenburg, W. (2015a). *Evaluatie van het OSR-model voor zoutindringing in de Rijn-Maasmonding (I)*. Tech. rep. Deltares, p. 114.

— (June 2015b). *Evaluatie van het OSR-model voor zoutindringing in de Rijn-Maasmonding (II)*. Tech. rep. Delft: Deltares, p. 89.

Kroon, A. and M. Niemeijer (Nov. 2025). *Onderhoudsvoorspelling Zeewaartse uitbreiding Maasvlakte 2*. Tech. rep. Rotterdam: SVASEK Hydraulics.

Lerczak, J. A., W. R. Geyer, and R. J. Chant (2006). "Mechanisms Driving the Time-Dependent Salt Flux in a Partially Stratified Estuary". In: *Journal of Physical Oceanography* 36.12, pp. 2296–2311. DOI: 10.1175/JPO2959.1.

Mariotti, G., A. Tweel, G. Gababa, and A. Tymul (Sept. 2025). "Comparing and Improving Different Methods to Quantify Silt and Clay Abundance within Estuarine Mud". In: *Continental Shelf Research* 292, p. 105508. DOI: 10.1016/j.csr.2025.105508.

NOVEX (June 2025). *Technische Verkenning Zeewaartse Uitbreiding in de Rotterdamse haven*. Tech. rep. NOVEX.

Partheniades, E. (2009). *Cohesive Sediments in Open Channels*. Elsevier. DOI: 10.1016/B978-1-85617-556-2.X0001-7.

Pietrzak, J. D., G. J. De Boer, and M. A. Eleveld (Apr. 2011). "Mechanisms Controlling the Intra-Annual Mesoscale Variability of SST and SPM in the Southern North Sea". In: *Continental Shelf Research* 31.6, pp. 594–610. DOI: 10.1016/j.csr.2010.12.014.

Port of Rotterdam (Dec. 13, 2023). *NOVEX: gezamenlijk ontwikkelperspectief voor de haven | Port of Rotterdam*. URL: https://www.portofrotterdam.com/nl/nieuws-en-persberichten/novex-gezamenlijk-ontwikkelperspectief-voor-de-haven.

Rijksoverheid (2026a). *Duinen Goeree & Kwade Hoek*. Ministerie van Landbouw, Visserij, Voedselzekerheid en Natuur. URL: https://www.natura2000.nl/gebieden/zuid-holland/duinen-goeree-kwade-hoek.

— (2026b). *Voornes Duin*. Ministerie van Landbouw, Visserij, Voedselzekerheid en Natuur. URL: https://www.natura2000.nl/gebieden/zuid-holland/voornes-duin.

Rijkswaterstaat (2026). *Baggeren*. https://www.rijkswaterstaat.nl/water/waterbeheer/beheer-en-ontwikkeling-rijkswateren/baggeren. webpagina.

Rijn, L. C. van, D.-J. R. Walstra, and M. van Ormondt (2007). “Unified View of Sediment Transport by Currents and Waves. IV: Application of Morphodynamic Model”. In: *Journal of Hydraulic Engineering* 133.7, pp. 776–793. DOI: 10.1061/(ASCE)0733-9429(2007)133:7(776).

Salomons, W., J. Gandrass, R. Eberhardt, C. Hagner, S. Rzepka, B. van Hattum, R. Peerboom, R. Vink, H. Behrendt, U. Foerstner, C. Peters, and T. Zoumis (Feb. 2001). *Dredged Material in the Port of Rotterdam*. Executive Summary. Geesthacht, Germany: GKSS Research Centre, Institute for Coastal Research, p. 26.

Shirahata, K., S. Yoshimoto, T. Tsuchihara, and S. Ishida (2016). “Digital Filters to Eliminate or Separate Tidal Components in Groundwater Observation Time-Series Data”. In: *Japan Agricultural Research Quarterly: JARQ* 50.3, pp. 241–252. DOI: 10.6090/jarq.50.241.

Souza, A. and J. Simpson (July 1996). “The Modification of Tidal Ellipses by Stratification in the Rhine ROFI”. In: *Continental Shelf Research* 16.8, pp. 997–1007. DOI: 10.1016/0278-4343(95)00042-9.

Suijlen, J. M. and R. N. M. Duin (Dec. 2002). “Atlas of near-surface Total Suspended Matter concentrations in the Dutch coastal zone of the North Sea”. In: *Research Repository (Delft University of Technology)*.

Thompson, R. O. R. Y. (June 1983). “Low-Pass Filters to Suppress Inertial and Tidal Frequencies”. In: *Journal of Physical Oceanography* 13.6, pp. 1077–1083. DOI: 10.1175/1520-0485(1983)013.

Van Alphen, J. (May 1990). “A Mud Balance for Belgian-Dutch Coastal Waters between 1969 and 1986”. In: *Netherlands Journal of Sea Research* 25.1-2, pp. 19–30. DOI: 10.1016/0077-7579(90)90005-2.

Van Der Hout, C. M., T. Gerkema, J. J. Nauw, and H. Ridderinkhof (Mar. 2015). “Observations of a Narrow Zone of High Suspended Particulate Matter (SPM) Concentrations along the Dutch Coast”. In: *Continental Shelf Research* 95, pp. 27–38. DOI: 10.1016/j.csr.2015.01.002.

Van Der Spek, A. J. and E. P. Elias (Dec. 2020). “Half a century of morphological change in the Haringvliet and Grevelingen ebb-tidal deltas (SW Netherlands) - Impacts of large-scale engineering 1964–2015”. In: *Marine Geology* 432, p. 106404. DOI: 10.1016/j.margeo.2020.106404.

Van Kessel, T. (Sept. 16, 1997). “Generation and Transport of Subaqueous Fluid Mud Layers”. PhD thesis. Delft: Delft University of Technology.

Van Kessel, T. (Nov. 2005). *Impacts on Maasvlakte 2 on the Wadden Sea and North Sea Coastal Zone*. Technical Report. Nijmegen: Royal Haskoning, p. 72.

Van Kessel, T., J. Vroom, and M. Taal (Apr. 2023). *A Conceptual Framework for Fine Sediment Dynamics in the Scheldt Estuary*. Tech. rep. 11208065-000. Delft: Deltares, p. 60.

Van Kessel, T., H. Winterwerp, B. Van Prooijen, M. Van Ledden, and W. Borst (May 2010). “Modelling the seasonal dynamics of SPM with a simple algorithm for the buffering of fines in a sandy seabed”. In: *Continental Shelf Research* 31.10, S124–S134. DOI: 10.1016/j.csr.2010.04.008.

Van Keulen, D., Q. Bi, F. Buschman, F. Bisschop, and T. van Kessel (Apr. 2025). *WP1 River Release Modelling, Monitoring and Analysis*. Tech. rep. Delft: Deltares, p. 120.

Vellinga, T. and M. Eisma (2005). “Management of contaminated dredged material in the port of Rotterdam”. In: *Managing European Coasts*. Ed. by J. Vermaat, W. Salomons, L. Bouwer, and K. Turner. Berlin, Heidelberg: Springer Berlin Heidelberg, pp. 315–322.

Verbruggen, W., W. de Boer, and F. Bisschop (Sept. 2025). *Eerste Beoordeling Nautische Veiligheid En Bereikbaarheid Zeewaartse Uitbreiding Haven van Rotterdam*. Tech. rep. Delft: Deltares, p. 84.

Verlaan, P. A. J. and R. Spanhoff (2000). “Massive sedimentation events at the mouth of the Rotterdam Waterway”. In: *Journal of Coastal Research* 16.2, pp. 458–469.

Waal, B. van der (May 2025). *PUMA-KF-BC-2025-08 Keuringsformulier*. Technical report 2.0. Rotterdam: Projectorganisatie Uitbreiding Maasvlakte, p. 19.

Winterwerp, J. C. and W. G. Van Kesteren (2004). *Introduction to the Physics of Cohesive Sediment in the Marine Environment*. Vol. Developments in Sedimentology. Amsterdam: Elsevier.

Zijl, F., S. Laan, A. Emmanouil, T. Van Kessel, L. Vilmin, and L. Van Duren (Apr. 2021). *Potential Ecosystem Effects of Large Upscaling of Offshore Wind in the North Sea*. Tech. rep. Delft: Deltares, p. 96.

A
Model settings

A.1. Delft3D-FLOW

Table A.1: Delft3D-FLOW model settings.

Parameter	Value
Timestep	$0.05\,\mathrm{min}$
Processes	Salinity
Roughness	Manning
Physical forcing	Wind, wave, online Delft3D-WAVE
Gravity	$9.813\,\mathrm{m\,s^{-2}}$
Water density	$1000\,\mathrm{kg\,m^{-3}}$
Air density	$1.25\,\mathrm{kg\,m^{-3}}$
Temperature	$10\,^{\circ}\mathrm{C}$
Horizontal eddy viscosity	$1\,\mathrm{m^2\,s^{-1}}$
Horizontal eddy diffusivity	$0.01\,\mathrm{m^2\,s^{-1}}$
Vertical eddy viscosity	$9.752 \times 10^{-7}\,\mathrm{m^2\,s^{-1}}$
Vertical eddy diffusivity	$9.752 \times 10^{-7}\,\mathrm{m^2\,s^{-1}}$
Turbulence model	k-ε
Wind drag coefficient	0.0006 at $5\,\mathrm{m\,s^{-1}}$ wind speed
Wind drag coefficient	0.0026 at $20\,\mathrm{m\,s^{-1}}$ wind speed
Wind drag coefficient	0.0026 at $100\,\mathrm{m\,s^{-1}}$ wind speed
Threshold depth	$0.15\,\mathrm{m}$
Advection scheme for momentum	Cyclic
Advection scheme for transport	Cyclic

A.2. DELWAQ

Table A.2: DELWAQ model settings.

Parameter	Value		Unit	Description
Taushields	0.8		$\mathrm{N\,m^{-2}}$	Shields shear stress for resuspension pick-up
GRAIN50	3.0	$\times 10^{-4}$	m	Median grain size (D_{50})
GRAV	9.8		$\mathrm{m\,s^{-2}}$	Gravitational acceleration
KinViscos	1.0	$\times 10^{-6}$	$\mathrm{m^2\,s^{-1}}$	Kinematic viscosity
RHOSAND	2.6	$\times 10^{6}$	$\mathrm{gDM/m^3}$	Bulk density of sand
RhoWater	1020		$\mathrm{kg\,m^{-3}}$	Density of water
PORS2	0.4		$\mathrm{m^3\,m^{-3}}$	Porosity of sediment layer S2
ThickS2	0.05		m	Thickness of sediment layer S2
MinDepth	0.01		m	Minimum water-layer thickness
MaxResPup	3600		$\mathrm{g\,m^{-2}\,d^{-1}}$	Maximum resuspension pick-up
FactResPup	3.0	$\times 10^{-8}$	–	Factor for resuspension pick-up
VSedIM1	0.1		$\mathrm{m\,d^{-1}}$	Settling velocity of IM1
TaucSIM1	0		$\mathrm{N\,m^{-2}}$	Critical shear stress for sedimentation of IM1
FrIM1SedS2	0.15		–	Fraction of IM1 sedimentation to bed layer S2
FrTIMS2Max	1		gDM/gDM	Max. fraction of total inorganic matter in bed layer S2
SWResIM1	1		–	Switch for resuspension of IM1
SWResusp	1		–	Switch for resuspension
ZResIM1	8640		$\mathrm{gDM/m^2/d}$	Zero-order resuspension rate of IM1
VResIM1	0.1		$\mathrm{d^{-1}}$	First-order resuspension rate of IM1
TaucRS1IM1	0.2		$\mathrm{N\,m^{-2}}$	Critical shear stress for resuspension of IM1 from S1
VSedIM2	10.8		$\mathrm{m\,d^{-1}}$	Settling velocity of IM2
TaucSIM2	0.15		$\mathrm{N\,m^{-2}}$	Critical shear stress for sedimentation of IM2
SWResIM2	1		–	Switch for resuspension of IM2
ZResIM2	8640		$\mathrm{gDM/m^2/d}$	Zero-order resuspension rate of IM2
VResIM2	0.3		$\mathrm{d^{-1}}$	First-order resuspension rate of IM2
TaucRS1IM2	0.2		$\mathrm{N\,m^{-2}}$	Critical shear stress for resuspension of IM2 from S1
VSedIM3	86.4		$\mathrm{m\,d^{-1}}$	Settling velocity of IM3
FrIM3SedS2	0.15		–	Fraction of IM3 sedimentation to bed layer S2
SWResIM3	1		–	Switch for resuspension of IM3
ZResIM3	8640		$\mathrm{gDM/m^2/d}$	Zero-order resuspension rate of IM3
VResIM3	0.1		$\mathrm{d^{-1}}$	First-order resuspension rate of IM3
TaucRS1IM3	0.2		$\mathrm{N\,m^{-2}}$	Critical shear stress for resuspension of IM3 from S1
Rough	1.0	$\times 10^{-4}$	m	Nikuradse roughness length
SwChezy	2		–	Switch to activate Manning roughness formulation
SwTauVeloc	1		–	Switch for shear-stress calculation from velocity

B
Model forcing

B.1. Forcing Delft3D-FLOW

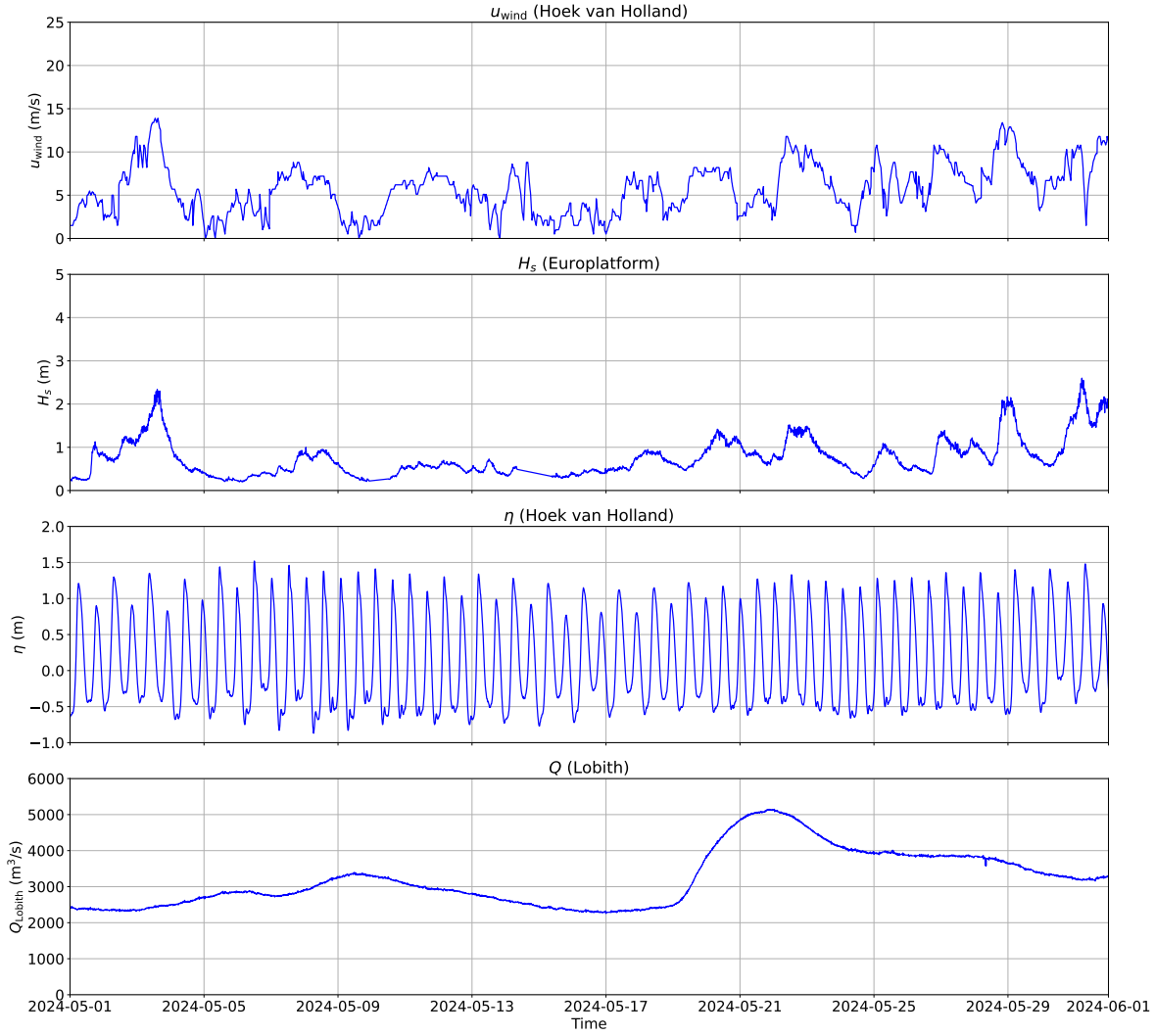

Figure B.1: Delft3D-FLOW forcing conditions retrieved from the Port of Rotterdam and used to select the representative 14.5-day spring–neap cycle. Panels show wind velocity (u_{wind}), significant wave height (H_s), water level (η), and discharge (Q).

B.2. Delft3D-FLOW Reference run validation

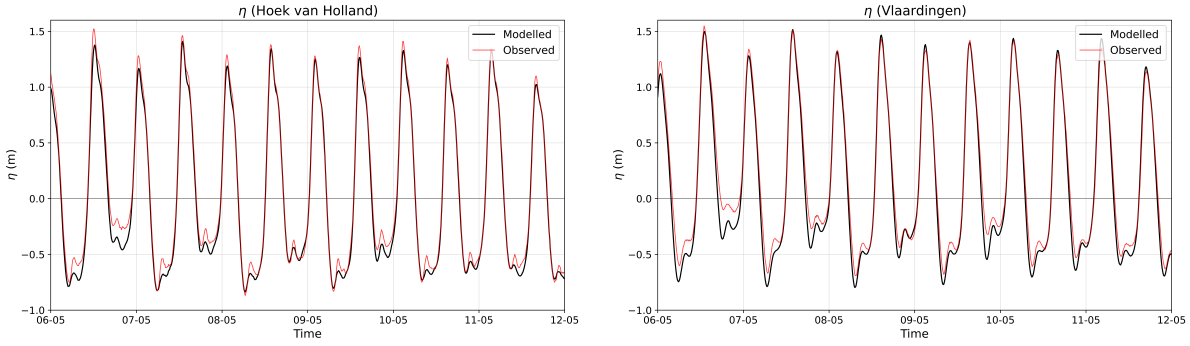

(a) Hoek van Holland

(b) Vlaardingen

Figure B.2: Modelled water-level time series at Hoek van Holland and Vlaardingen from the OSR–NSC Delft3D-FLOW simulation, validated against Port of Rotterdam measurements.

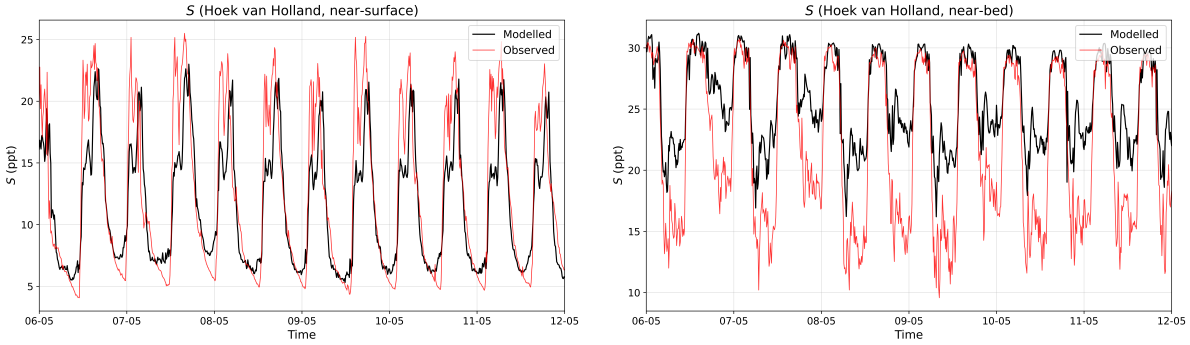

(a) Near-surface salinity

(b) Near-bed salinity

Figure B.3: Modelled salinity time series at Hoek van Holland from the OSR–NSC Delft3D-FLOW simulation, validated against Port of Rotterdam measurements.

B.3. Time-frame selection

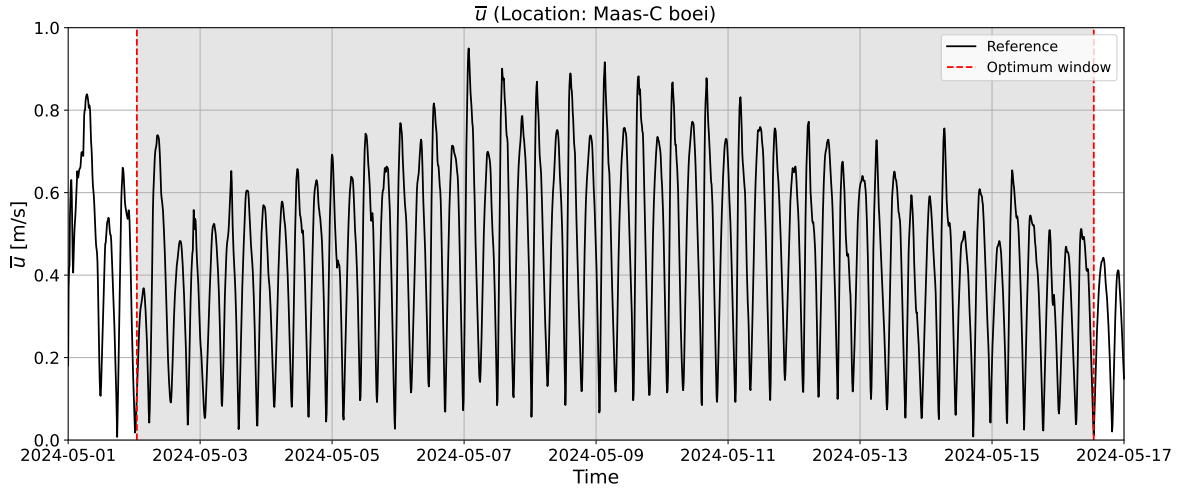

Figure B.4: Selected 14.5-day spring–neap cycle based on the minimum start–end discontinuity in depth-averaged velocity ($\overline{u}$). The selected period runs from 02-05-2024 01:00:00 to 16-05-2024 13:00:00.

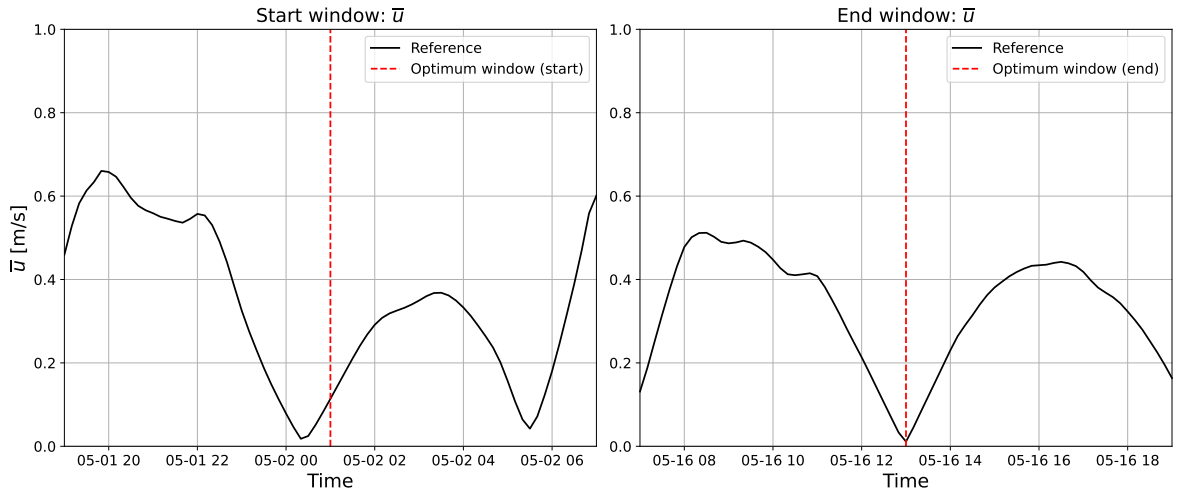

Figure B.5: Start–end discontinuity in depth-averaged velocity for the selected 14.5-day spring–neap cycle ($\Delta\overline{u} = -0.10\ \mathrm{m\,s^{-1}}$).

C
Offshore

C.1. Hydrodynamics

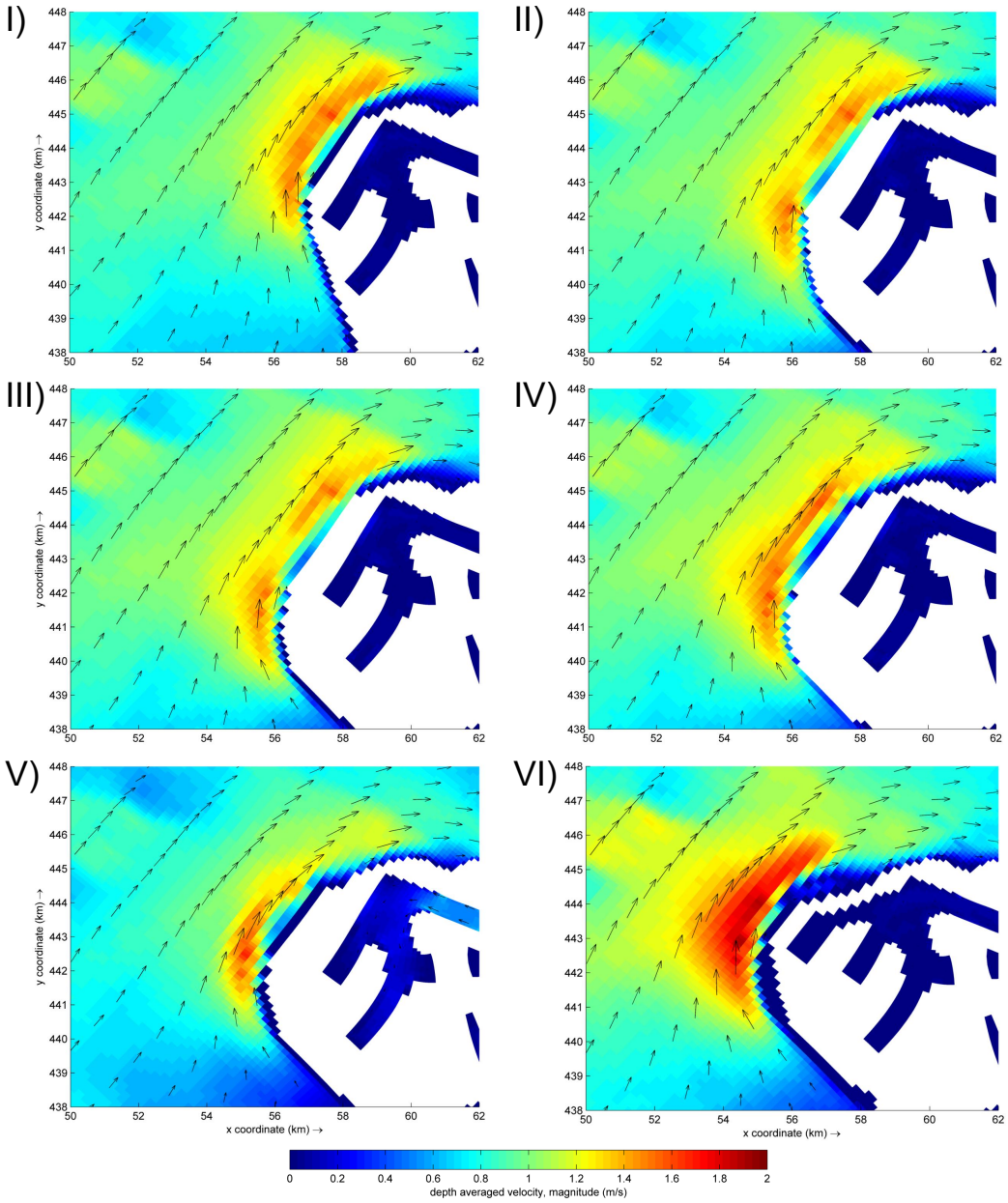

Figure C.1: Depth-averaged flow field ($\overline{u}$) around MV2 and the SPE designs during peak spring flood. Panels I–VI show the Reference scenario, A1, A2, B1, B2, and C, respectively.

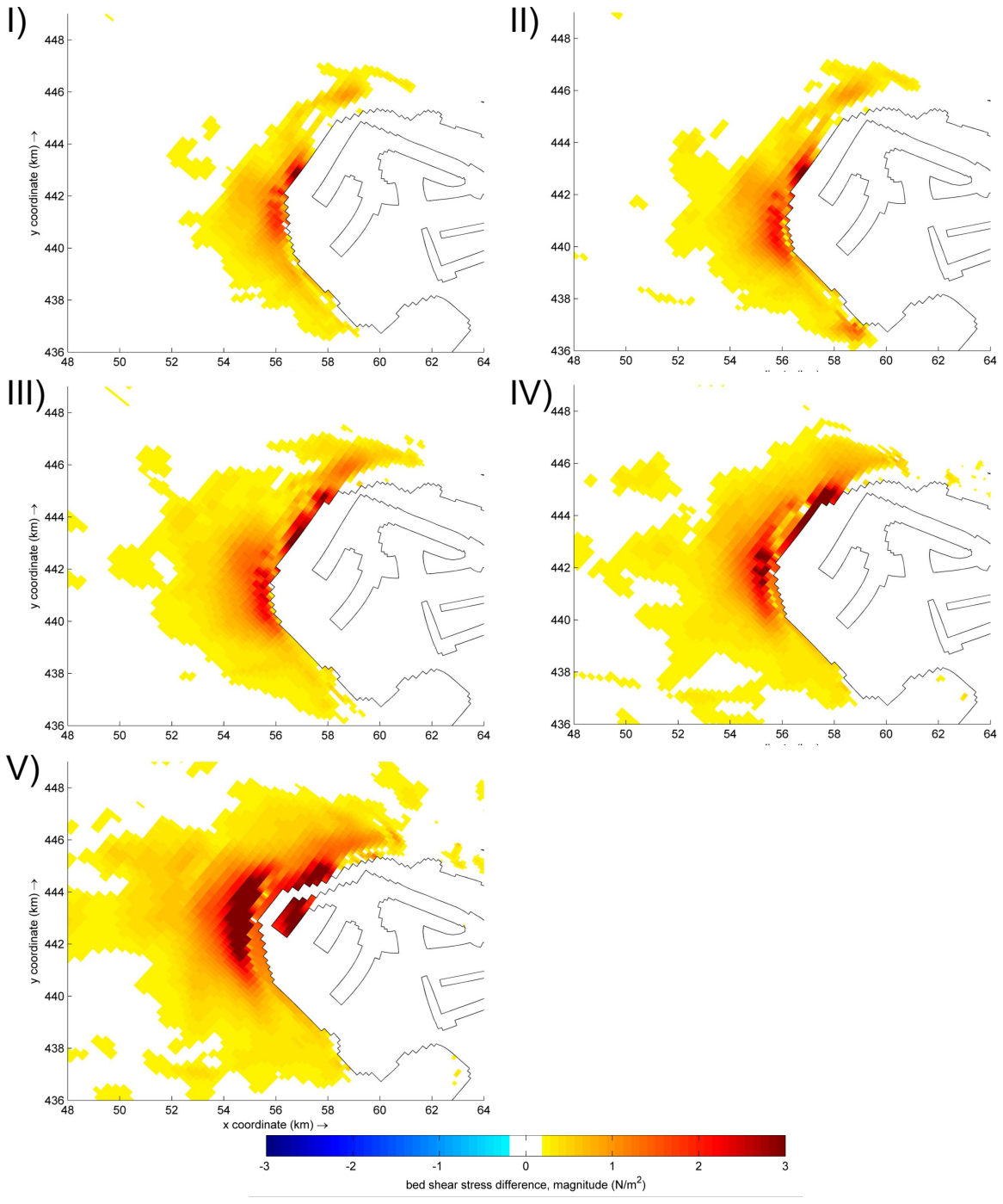

Figure C.2: Absolute difference in bed shear stress ($\Delta\tau_b$) between the SPE designs and the Reference scenario during peak spring flood. Panels I–V show A1, A2, B1, B2, and C, respectively.

C.2. Redistribution

Sources

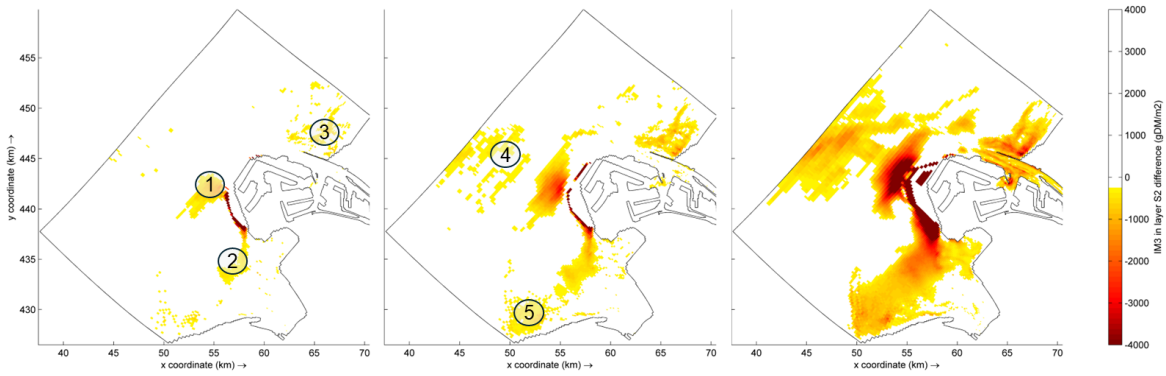

Figure C.3: IM3 bed mass differences in Layer S_2 at the end of the simulation relative to the Reference scenario. Panels show Design A1 (left), Design B1 (middle), and Design C (right). Negative values ($\Delta M_{S2,\mathrm{IM3}}(t_1) < 0$) indicate potential fine sediment source regions. Locations 1–5 indicate selected areas of interest for further analysis.

Area 1

Table C.1: Observation point (115,24) — IM1

Scenario	ΔM_{bed} [gDM]	ΔM_{bed}	$\overline{\tau}_b$ [N/m^2]	$\Delta\tau_b$	$\overline{c}_{IM1}$ [gDM/m^3]	Δc_{IM1}
Reference	10.2	–	0.62	–	1.0	–
Design A1	9.9	-2.2%	0.65	+4.6%	1.0	-0.0%
Design A2	9.9	-2.8%	0.66	+6.0%	1.0	-0.0%
Design B1	9.3	-8.6%	0.73	+17.5%	1.0	-0.1%
Design B2	8.3	-18.6%	0.84	+36.1%	1.0	-0.3%
Design C	4.4	-56.8%	1.30	+110.7%	1.0	-0.7%

Table C.2: Observation point (115,24) — IM2

Scenario	ΔM_{bed} [gDM]	ΔM_{bed}	$\overline{\tau}_b$ [N/m^2]	$\Delta\tau_b$	$\overline{c}_{IM2}$ [gDM/m^3]	Δc_{IM2}
Reference	97.3	–	0.62	–	6.2	–
Design A1	95.1	-2.2%	0.65	+4.6%	6.2	+1.0%
Design A2	94.5	-2.8%	0.66	+6.0%	6.2	+0.9%
Design B1	87.3	-10.3%	0.73	+17.5%	6.2	+0.8%
Design B2	75.9	-22.0%	0.84	+36.1%	6.2	-0.1%
Design C	38.5	-60.4%	1.30	+110.7%	5.9	-4.2%

Table C.3: Observation point (115,24) — IM3

Scenario	ΔM_{bed} [gDM]	ΔM_{bed}	$\overline{\tau}_b$ [N/m^2]	$\Delta\tau_b$	$\overline{c}_{IM3}$ [gDM/m^3]	Δc_{IM3}
Reference	7,319.0	–	0.62	–	21.6	–
Design A1	7,328.4	+0.1%	0.65	+4.6%	22.6	+5.0%
Design A2	7,331.3	+0.2%	0.66	+6.0%	22.8	+5.7%
Design B1	6,749.2	-7.8%	0.73	+17.5%	23.5	+9.2%
Design B2	6,068.0	-17.1%	0.84	+36.1%	25.1	+16.2%
Design C	3,628.9	-50.4%	1.30	+110.7%	28.1	+30.1%

Table C.4: Observation point (141,31) — IM1

Scenario	ΔM_{bed} [gDM]	ΔM_{bed}	$\overline{\tau}_b$ [N/m^2]	$\Delta \tau_b$	$\overline{c}_{IM1}$ [gDM/m^3]	Δc_{IM1}
Reference	10.5	–	0.50	–	1.0	–
Design A1	9.9	-5.9%	0.62	+24.4%	1.0	-0.1%
Design A2	9.6	-9.2%	0.67	+35.6%	1.0	-0.1%
Design B1	9.1	-13.4%	0.75	+50.8%	1.0	-0.3%
Design B2	8.2	-22.4%	0.86	+73.0%	1.0	-0.4%
Design C	6.4	-39.2%	1.03	+107.6%	0.9	-1.0%

Table C.5: Observation point (141,31) — IM2

Scenario	ΔM_{bed} [gDM]	ΔM_{bed}	$\overline{\tau}_b$ [N/m^2]	$\Delta \tau_b$	$\overline{c}_{IM2}$ [gDM/m^3]	Δc_{IM2}
Reference	102.3	–	0.50	–	6.6	–
Design A1	95.8	-6.4%	0.62	+24.4%	6.6	-0.3%
Design A2	92.0	-10.1%	0.67	+35.6%	6.6	-1.0%
Design B1	86.1	-15.8%	0.75	+50.8%	6.4	-2.7%
Design B2	74.6	-27.1%	0.86	+73.0%	6.2	-6.3%
Design C	57.8	-43.5%	1.03	+107.6%	5.7	-14.1%

Table C.6: Observation point (141,31) — IM3

Scenario	ΔM_{bed} [gDM]	ΔM_{bed}	$\overline{\tau}_b$ [N/m^2]	$\Delta \tau_b$	$\overline{c}_{IM3}$ [gDM/m^3]	Δc_{IM3}
Reference	9,313.7	–	0.50	–	27.8	–
Design A1	8,132.4	-12.7%	0.62	+24.4%	29.9	+7.5%
Design A2	7,765.7	-16.6%	0.67	+35.6%	30.2	+8.4%
Design B1	7,145.8	-23.3%	0.75	+50.8%	30.2	+8.4%
Design B2	6,306.4	-32.3%	0.86	+73.0%	31.0	+11.5%
Design C	6,121.6	-34.3%	1.03	+107.6%	30.6	+10.1%

Area 2

Table C.7: Observation point (151,75) — IM1

Scenario	ΔM_{bed} [gDM]	ΔM_{bed}	$\overline{\tau}_b$ [N/m^2]	$\Delta \tau_b$	$\overline{c}_{IM1}$ [gDM/m^3]	Δc_{IM1}
Reference	20.3	–	0.16	–	0.8	–
Design A1	20.4	+0.7%	0.16	-1.9%	0.8	-0.7%
Design A2	18.0	-11.2%	0.17	+5.2%	0.8	-1.2%
Design B1	20.0	-1.7%	0.16	-3.4%	0.8	-2.0%
Design B2	20.1	-1.2%	0.15	-4.3%	0.8	-2.4%
Design C	20.3	-0.1%	0.15	-5.6%	0.8	-2.6%

Table C.8: Observation point (151,75) — IM2

Scenario	ΔM_{bed} [gDM]	ΔM_{bed}	$\overline{\tau}_b$ [N/m^2]	$\Delta \tau_b$	$\overline{c}_{IM2}$ [gDM/m^3]	Δc_{IM2}
Reference	216.5	–	0.16	–	6.9	–
Design A1	210.8	-2.6%	0.16	-1.9%	6.8	-1.5%
Design A2	188.5	-12.9%	0.17	+5.2%	6.4	-6.9%
Design B1	231.1	+6.8%	0.16	-3.4%	6.8	-1.1%
Design B2	213.9	-1.2%	0.15	-4.3%	6.6	-5.2%
Design C	232.2	+7.3%	0.15	-5.6%	6.5	-5.9%

Table C.9: Observation point (151,75) — IM3

Scenario	ΔM_{bed} [gDM]	ΔM_{bed}	$\overline{\tau}_b$ [N/m^2]	$\Delta \tau_b$	$\overline{c}_{IM3}$ [gDM/m^3]	Δc_{IM3}
Reference	4,639.3	–	0.16	–	5.5	–
Design A1	3,709.2	-20.0%	0.16	-1.9%	4.6	-16.0%
Design A2	3,182.1	-31.4%	0.17	+5.2%	4.0	-27.0%
Design B1	3,539.7	-23.7%	0.16	-3.4%	4.0	-26.4%
Design B2	2,957.6	-36.2%	0.15	-4.3%	3.3	-38.6%
Design C	1,783.6	-61.6%	0.15	-5.6%	1.8	-66.2%

Area 3

Table C.10: Observation point (70,22) — IM1

Scenario	ΔM_{bed} [gDM]	ΔM_{bed}	$\overline{\tau}_b$ [N/m^2]	$\Delta \tau_b$	$\overline{c}_{IM1}$ [gDM/m^3]	Δc_{IM1}
Reference	13.4	–	0.27	–	1.0	–
Design A1	13.5	+0.9%	0.27	-0.7%	1.0	-0.0%
Design A2	13.4	+0.6%	0.27	-0.4%	1.0	-0.1%
Design B1	13.7	+2.4%	0.26	-2.4%	1.0	-0.0%
Design B2	14.0	+5.1%	0.26	-4.5%	1.0	-0.1%
Design C	14.9	+11.7%	0.24	-9.9%	1.0	-0.1%

Table C.11: Observation point (70,22) — IM2

Scenario	ΔM_{bed} [gDM]	ΔM_{bed}	$\overline{\tau}_b$ [N/m^2]	$\Delta \tau_b$	$\overline{c}_{IM2}$ [gDM/m^3]	Δc_{IM2}
Reference	89.4	–	0.27	–	5.5	–
Design A1	87.5	-2.1%	0.27	-0.7%	5.4	-0.4%
Design A2	86.9	-2.7%	0.27	-0.4%	5.4	-0.9%
Design B1	87.4	-2.2%	0.26	-2.4%	5.4	-1.0%
Design B2	88.9	-0.5%	0.26	-4.5%	5.4	-1.0%
Design C	89.7	+0.4%	0.24	-9.9%	5.4	-0.5%

Table C.12: Observation point (70,22) — IM3

Scenario	ΔM_{bed} [gDM]	ΔM_{bed}	$\overline{\tau}_b$ [N/m^2]	$\Delta \tau_b$	$\overline{c}_{IM3}$ [gDM/m^3]	Δc_{IM3}
Reference	11,128.2	–	0.27	–	23.7	–
Design A1	10,586.8	-4.9%	0.27	-0.7%	23.1	-2.5%
Design A2	10,158.5	-8.7%	0.27	-0.4%	22.4	-5.5%
Design B1	10,669.1	-4.1%	0.26	-2.4%	22.5	-5.1%
Design B2	11,308.0	+1.6%	0.26	-4.5%	22.5	-5.0%
Design C	12,103.6	+8.8%	0.24	-9.9%	21.9	-7.6%

Area 4

Table C.13: Observation point (120,16) — IM1

Scenario	ΔM_{bed} [gDM]	ΔM_{bed}	$\overline{\tau}_b$ [N/m^2]	$\Delta \tau_b$	$\overline{c}_{IM1}$ [gDM/m^3]	Δc_{IM1}
Reference	10.5	–	0.59	–	1.0	–
Design A1	10.3	-1.5%	0.61	+4.1%	1.0	+0.0%
Design A2	10.3	-1.7%	0.62	+5.2%	1.0	+0.1%
Design B1	10.0	-4.1%	0.66	+11.5%	1.0	+0.0%
Design B2	9.7	-7.6%	0.71	+20.1%	1.0	+0.0%
Design C	8.5	-19.1%	0.85	+43.8%	1.0	-0.0%

Table C.14: Observation point (120,16) — IM2

Scenario	ΔM_{bed} [gDM]	ΔM_{bed}	$\overline{\tau}_b$ [N/m^2]	$\Delta \tau_b$	$\overline{c}_{IM2}$ [gDM/m^3]	Δc_{IM2}
Reference	90.1	–	0.59	–	5.6	–
Design A1	88.9	-1.3%	0.61	+4.1%	5.6	+0.4%
Design A2	88.6	-1.7%	0.62	+5.2%	5.6	+0.4%
Design B1	86.2	-4.3%	0.66	+11.5%	5.6	+0.4%
Design B2	82.8	-8.1%	0.71	+20.1%	5.6	+0.6%
Design C	71.5	-20.6%	0.85	+43.8%	5.6	+0.6%

Table C.15: Observation point (120,16) — IM3

Scenario	ΔM_{bed} [gDM]	ΔM_{bed}	$\overline{\tau}_b$ [N/m^2]	$\Delta \tau_b$	$\overline{c}_{IM3}$ [gDM/m^3]	Δc_{IM3}
Reference	5,684.2	–	0.59	–	16.8	–
Design A1	5,626.9	-1.0%	0.61	+4.1%	16.9	+0.8%
Design A2	5,607.1	-1.4%	0.62	+5.2%	16.9	+1.0%
Design B1	5,411.4	-4.8%	0.66	+11.5%	16.9	+1.1%
Design B2	5,209.2	-8.4%	0.71	+20.1%	17.2	+2.9%
Design C	4,785.5	-15.8%	0.85	+43.8%	18.5	+10.4%

Area 5

Table C.16: Observation point (201,62) — IM1

Scenario	ΔM_{bed} [gDM]	ΔM_{bed}	$\overline{\tau}_b$ [N/m^2]	$\Delta \tau_b$	$\overline{c}_{IM1}$ [gDM/m^3]	Δc_{IM1}
Reference	22.9	–	0.17	–	0.9	–
Design A1	24.0	+5.0%	0.16	-3.4%	0.9	-0.6%
Design A2	24.3	+6.3%	0.16	-4.4%	0.9	-0.8%
Design B1	24.8	+8.5%	0.16	-5.7%	0.9	-1.1%
Design B2	25.6	+12.0%	0.15	-7.4%	0.9	-1.4%
Design C	27.0	+17.7%	0.15	-11.5%	0.9	-1.7%

Table C.17: Observation point (201,62) — IM2

Scenario	ΔM_{bed} [gDM]	ΔM_{bed}	$\overline{\tau}_b$ [N/m^2]	$\Delta \tau_b$	$\overline{c}_{IM2}$ [gDM/m^3]	Δc_{IM2}
Reference	227.8	–	0.17	–	9.6	–
Design A1	230.4	+1.1%	0.16	-3.4%	9.5	-1.6%
Design A2	231.2	+1.5%	0.16	-4.4%	9.4	-2.1%
Design B1	239.0	+4.9%	0.16	-5.7%	9.3	-2.8%
Design B2	230.4	+1.1%	0.15	-7.4%	9.0	-6.1%
Design C	240.0	+5.4%	0.15	-11.5%	8.6	-10.9%

Table C.18: Observation point (201,62) — IM3

Scenario	ΔM_{bed} [gDM]	ΔM_{bed}	$\overline{\tau}_b$ [N/m^2]	$\Delta \tau_b$	$\overline{c}_{IM3}$ [gDM/m^3]	Δc_{IM3}
Reference	9,927.3	–	0.17	–	6.8	–
Design A1	9,346.1	-5.9%	0.16	-3.4%	6.2	-8.9%
Design A2	8,948.9	-9.9%	0.16	-4.4%	6.0	-11.8%
Design B1	8,698.4	-12.4%	0.16	-5.7%	5.7	-17.0%
Design B2	8,330.7	-16.1%	0.15	-7.4%	5.4	-21.6%
Design C	7,405.1	-25.4%	0.15	-11.5%	4.4	-35.1%

Sinks

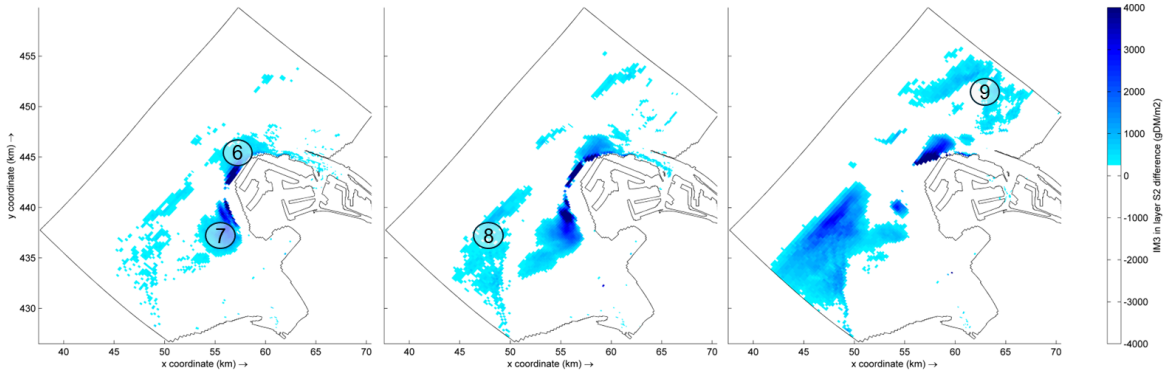

Figure C.4: IM3 bed mass differences in Layer S_2 at the end of the simulation relative to the Reference scenario. Panels show Design A1 (left), Design B1 (middle), and Design C (right). Positive values ($\Delta M_{S2,\mathrm{IM3}}(t_1) > 0$) indicate potential fine sediment sink regions. Locations 6–9 indicate selected areas of interest for further analysis.

Area 6

Table C.19: Observation point (69,36) — IM1

Scenario	ΔM_{bed} [gDM]	ΔM_{bed}	$\overline{\tau}_b$ [N/m^2]	$\Delta\tau_b$	$\overline{c}_{IM1}$ [gDM/m^3]	Δc_{IM1}
Reference	5.0	–	1.18	–	1.0	–
Design A1	5.5	+8.4%	1.14	-3.5%	1.0	-0.1%
Design A2	5.6	+10.6%	1.13	-4.3%	1.0	-0.1%
Design B1	6.4	+27.5%	1.01	-14.2%	1.0	-0.2%
Design B2	7.2	+44.0%	0.91	-23.0%	1.0	-0.1%
Design C	8.3	+64.5%	0.78	-34.3%	1.0	-0.1%

Table C.20: Observation point (69,36) — IM2

Scenario	ΔM_{bed} [gDM]	ΔM_{bed}	$\overline{\tau}_b$ [N/m^2]	$\Delta\tau_b$	$\overline{c}_{IM2}$ [gDM/m^3]	Δc_{IM2}
Reference	43.5	–	1.18	–	6.0	–
Design A1	47.4	+9.0%	1.14	-3.5%	6.1	+0.8%
Design A2	48.4	+11.2%	1.13	-4.3%	6.1	+0.9%
Design B1	55.6	+27.7%	1.01	-14.2%	6.1	+1.0%
Design B2	61.7	+41.6%	0.91	-23.0%	6.0	-0.4%
Design C	68.5	+57.4%	0.78	-34.3%	5.9	-2.4%

Table C.21: Observation point (69,36) — IM3

Scenario	ΔM_{bed} [gDM]	ΔM_{bed}	$\overline{\tau}_b$ [N/m^2]	$\Delta\tau_b$	$\overline{c}_{IM3}$ [gDM/m^3]	Δc_{IM3}
Reference	4,662.9	–	1.18	–	31.0	–
Design A1	5,104.5	+9.5%	1.14	-3.5%	31.9	+3.1%
Design A2	5,327.8	+14.3%	1.13	-4.3%	32.4	+4.5%
Design B1	5,966.4	+28.0%	1.01	-14.2%	31.7	+2.2%
Design B2	6,339.1	+35.9%	0.91	-23.0%	30.3	-2.3%
Design C	6,758.3	+44.9%	0.78	-34.3%	28.6	-7.8%

Area 7

Table C.22: Observation point (152,55) — IM1

Scenario	ΔM_{bed} [gDM]	ΔM_{bed}	$\overline{\tau}_b$ [N/m^2]	$\Delta\tau_b$	$\overline{c}_{IM1}$ [gDM/m^3]	Δc_{IM1}
Reference	18.6	–	0.23	–	0.9	–
Design A1	30.6	+64.4%	0.18	-22.3%	0.9	-0.4%
Design A2	34.1	+83.2%	0.17	-27.9%	0.9	-0.5%
Design B1	38.4	+106.0%	0.15	-33.6%	0.9	-0.9%
Design B2	43.6	+133.9%	0.14	-39.5%	0.9	-1.4%
Design C	53.1	+185.0%	0.12	-49.8%	0.9	-2.5%

Table C.23: Observation point (152,55) — IM2

Scenario	ΔM_{bed} [gDM]	ΔM_{bed}	$\overline{\tau}_b$ [N/m^2]	$\Delta\tau_b$	$\overline{c}_{IM2}$ [gDM/m^3]	Δc_{IM2}
Reference	112.1	–	0.23	–	5.5	–
Design A1	145.5	+29.8%	0.18	-22.3%	5.5	-0.8%
Design A2	163.0	+45.4%	0.17	-27.9%	5.5	-1.4%
Design B1	196.4	+75.2%	0.15	-33.6%	5.4	-2.2%
Design B2	243.7	+117.4%	0.14	-39.5%	5.3	-4.8%
Design C	388.4	+246.4%	0.12	-49.8%	5.1	-8.6%

Table C.24: Observation point (152,55) — IM3

Scenario	ΔM_{bed} [gDM]	ΔM_{bed}	$\overline{\tau}_b$ [N/m^2]	$\Delta\tau_b$	$\overline{c}_{IM3}$ [gDM/m^3]	Δc_{IM3}
Reference	12,185.4	–	0.23	–	15.6	–
Design A1	21,476.3	+76.2%	0.18	-22.3%	18.0	+15.5%
Design A2	24,646.6	+102.3%	0.17	-27.9%	18.6	+19.1%
Design B1	26,190.6	+114.9%	0.15	-33.6%	17.9	+14.8%
Design B2	25,829.4	+112.0%	0.14	-39.5%	16.3	+4.7%
Design C	21,072.3	+72.9%	0.12	-49.8%	11.1	-29.1%

Area 8

Table C.25: Observation point (174,26) — IM1

Scenario	ΔM_{bed} [gDM]	ΔM_{bed}	$\overline{\tau}_b$ [N/m^2]	$\Delta\tau_b$	$\overline{c}_{IM1}$ [gDM/m^3]	Δc_{IM1}
Reference	11.2	–	0.41	–	1.0	–
Design A1	11.1	-0.4%	0.42	+1.2%	1.0	+0.1%
Design A2	11.1	-0.5%	0.42	+2.1%	1.0	+0.1%
Design B1	11.1	-0.4%	0.42	+2.5%	1.0	+0.1%
Design B2	11.1	-0.9%	0.43	+3.4%	1.0	+0.1%
Design C	11.1	-1.0%	0.43	+3.2%	1.0	+0.0%

Table C.26: Observation point (174,26) — IM2

Scenario	ΔM_{bed} [gDM]	ΔM_{bed}	$\overline{\tau}_b$ [N/m^2]	$\Delta\tau_b$	$\overline{c}_{IM2}$ [gDM/m^3]	Δc_{IM2}
Reference	112.6	–	0.41	–	6.3	–
Design A1	109.7	-2.6%	0.42	+1.2%	6.3	+0.1%
Design A2	108.5	-3.6%	0.42	+2.1%	6.3	-0.1%
Design B1	107.3	-4.6%	0.42	+2.5%	6.3	-0.5%
Design B2	104.3	-7.4%	0.43	+3.4%	6.2	-1.4%
Design C	100.1	-11.1%	0.43	+3.2%	6.2	-1.9%

Table C.27: Observation point (174,26) — IM3

Scenario	ΔM_{bed} [gDM]	ΔM_{bed}	$\overline{\tau}_b$ [N/m^2]	$\Delta \tau_b$	$\overline{c}_{IM3}$ [gDM/m^3]	Δc_{IM3}
Reference	8,677.4	–	0.41	–	20.7	–
Design A1	8,939.7	+3.0%	0.42	+1.2%	22.0	+6.5%
Design A2	8,938.8	+3.0%	0.42	+2.1%	22.4	+8.3%
Design B1	8,941.1	+3.0%	0.42	+2.5%	22.8	+10.4%
Design B2	8,932.4	+2.9%	0.43	+3.4%	23.4	+13.3%
Design C	10,267.1	+18.3%	0.43	+3.2%	27.6	+33.4%

Area 9

Table C.28: Observation point (27,19) — IM1

Scenario	ΔM_{bed} [gDM]	ΔM_{bed}	$\overline{\tau}_b$ [N/m^2]	$\Delta \tau_b$	$\overline{c}_{IM1}$ [gDM/m^3]	Δc_{IM1}
Reference	11.2	–	0.43	–	1.0	–
Design A1	11.2	+0.1%	0.43	-0.9%	1.0	-0.0%
Design A2	11.2	+0.2%	0.43	-1.0%	1.0	-0.0%
Design B1	11.2	+0.5%	0.42	-2.7%	1.0	-0.0%
Design B2	11.3	+1.2%	0.41	-5.1%	1.0	-0.0%
Design C	11.4	+2.5%	0.39	-9.0%	1.0	-0.0%

Table C.29: Observation point (27,19) — IM2

Scenario	ΔM_{bed} [gDM]	ΔM_{bed}	$\overline{\tau}_b$ [N/m^2]	$\Delta \tau_b$	$\overline{c}_{IM2}$ [gDM/m^3]	Δc_{IM2}
Reference	80.0	–	0.43	–	5.1	–
Design A1	80.0	-0.0%	0.43	-0.9%	5.1	-0.2%
Design A2	79.8	-0.3%	0.43	-1.0%	5.1	-0.5%
Design B1	79.9	-0.1%	0.42	-2.7%	5.1	-0.4%
Design B2	79.7	-0.3%	0.41	-5.1%	5.1	-0.4%
Design C	79.8	-0.3%	0.39	-9.0%	5.1	-0.3%

Table C.30: Observation point (27,19) — IM3

Scenario	ΔM_{bed} [gDM]	ΔM_{bed}	$\overline{\tau}_b$ [N/m^2]	$\Delta \tau_b$	$\overline{c}_{IM3}$ [gDM/m^3]	Δc_{IM3}
Reference	7,069.1	–	0.43	–	20.6	–
Design A1	7,150.3	+1.1%	0.43	-0.9%	20.5	-0.4%
Design A2	7,102.4	+0.5%	0.43	-1.0%	20.4	-0.9%
Design B1	7,151.8	+1.2%	0.42	-2.7%	20.6	+0.0%
Design B2	7,025.0	-0.6%	0.41	-5.1%	20.5	-0.3%
Design C	7,194.9	+1.8%	0.39	-9.0%	20.8	+1.1%

C.3. Scour area

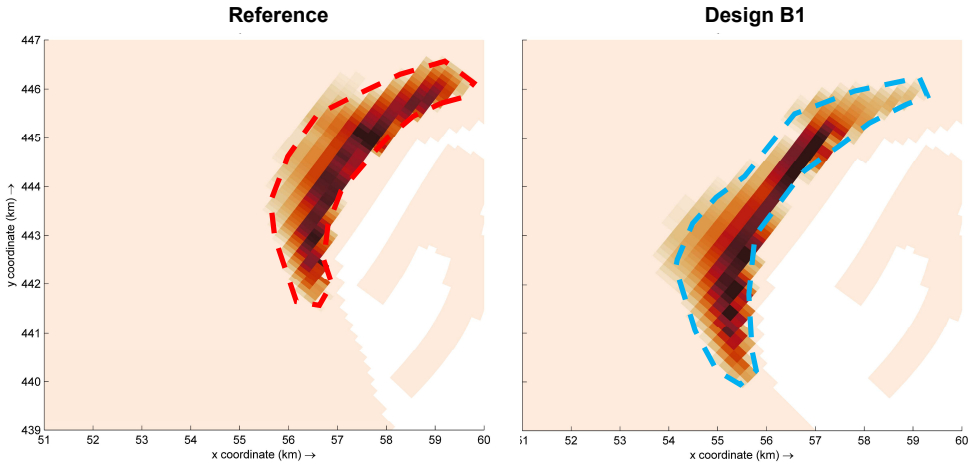

(a) Threshold-exceedance areas for the Reference and Design B1 scenarios.

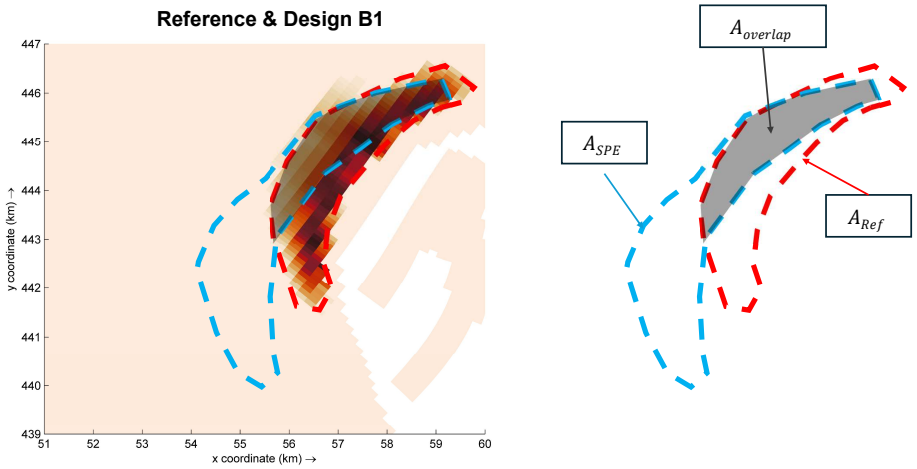

(b) Area decomposition used to isolate the newly induced potential scour area.

Figure C.5: Example of the Delft3D-based scour-area estimate for $\tau_{b,\mathrm{cr}} = 1.2$ N/m^2. The potential scour area is defined as the threshold-exceedance area where $\tau_b > \tau_{b,\mathrm{cr}}$.

Table C.31: Potential scour-area estimates for the Reference and SPE design scenarios, based on three bed shear stress thresholds.

$\tau_{b,\mathrm{cr}}$	Parameter	Reference	Design A1	Design A2	Design B1	Design B2	Design C
0.8 N/m^2	A_{SPE} [km^2]	12.80	16.62	16.38	17.20	12.73	17.07
	A_{overlap} [km^2]	–	11.03	11.42	10.24	8.98	1.26
	A_{new} [km^2]	–	5.59	4.96	6.96	3.75	15.81
	R_A [-]	–	1.44	1.39	1.54	1.29	2.24
1.2 N/m^2	A_{SPE} [km^2]	11.18	11.96	14.14	13.95	10.08	15.12
	A_{overlap} [km^2]	–	8.90	8.89	7.32	3.43	0.00
	A_{new} [km^2]	–	3.06	5.25	6.63	6.65	15.12
	R_A [-]	–	1.27	1.47	1.59	1.59	2.35
1.6 N/m^2	A_{SPE} [km^2]	9.06	10.06	10.18	13.38	12.11	16.80
	A_{overlap} [km^2]	–	6.13	6.51	6.77	5.93	0.84
	A_{new} [km^2]	–	3.93	3.67	6.61	6.19	15.96
	R_A [-]	–	1.31	1.29	1.52	1.48	2.25
	$\overline{R}_A$ [-]	1.00	1.34	1.38	1.55	1.46	2.28

D Transport (Maasmond)

D.1. Transport balance

Table D.1: IM1 transport through the Maasmond, decomposed into net transport, import, and export, and reported as Reference values and SPE-induced absolute and relative changes (△).

	Reference	A1	A2	B1	B2	C
F_{net} [tonDM]	-8,916	-8,901	-8,902	-8,888	-8,883	-8,849
F_{import} [tonDM]	28,579	28,559	28,497	28,487	28,374	28,678
F_{export} [tonDM]	37,495	37,460	37,400	37,375	37,257	37,527
ΔF_{net} [tonDM]	–	+15	+14	+28	+33	+67
ΔF_{import} [tonDM]	–	-20	-82	-92	-205	+99
ΔF_{export} [tonDM]	–	-35	-95	-121	-238	+32
ΔF_{net} [%]	–	-0.17%	-0.15%	-0.32%	-0.37%	-0.75%
ΔF_{import} [%]	–	-0.07%	-0.29%	-0.32%	-0.72%	+0.35%
ΔF_{export} [%]	–	-0.09%	-0.25%	-0.32%	-0.64%	+0.09%

Table D.2: IM2 transport through the Maasmond, decomposed into net transport, import, and export, and reported as Reference values and SPE-induced absolute and relative changes (△).

	Reference	A1	A2	B1	B2	C
F_{net} [tonDM]	-9,662	-9,475	-9,657	-9,544	-9,427	-8,655
F_{import} [tonDM]	182,064	182,768	181,751	181,841	180,142	181,893
F_{export} [tonDM]	191,726	192,242	191,408	191,386	189,569	190,548
ΔF_{net} [tonDM]	–	+187	+5	+118	+235	+1,008
ΔF_{import} [tonDM]	–	+704	-313	-222	-1,921	-170
ΔF_{export} [tonDM]	–	+516	-318	-340	-2,157	-1,178
ΔF_{net} [%]	–	-1.94%	-0.05%	-1.22%	-2.44%	-10.43%
ΔF_{import} [%]	–	+0.39%	-0.17%	-0.12%	-1.06%	-0.09%
ΔF_{export} [%]	–	+0.27%	-0.17%	-0.18%	-1.12%	-0.61%

Table D.3: IM3 transport through the Maasmond, decomposed into net transport, import, and export, and reported as Reference values and SPE-induced absolute and relative changes (△).

	Reference	A1	A2	B1	B2	C
F_{net} [tonDM]	526,331	529,046	528,181	521,520	504,362	478,975
F_{import} [tonDM]	840,246	847,035	846,090	835,517	809,290	775,449
F_{export} [tonDM]	313,915	317,989	317,909	313,997	304,927	296,474
ΔF_{net} [tonDM]	–	+2,715	+1,850	-4,811	-21,968	-47,355
ΔF_{import} [tonDM]	–	+6,789	+5,844	-4,729	-30,956	-64,797
ΔF_{export} [tonDM]	–	+4,074	+3,994	+82	-8,988	-17,441
ΔF_{net} [%]	–	+0.52%	+0.35%	-0.91%	-4.17%	-9.00%
ΔF_{import} [%]	–	+0.81%	+0.70%	-0.56%	-3.68%	-7.71%
ΔF_{export} [%]	–	+1.30%	+1.27%	+0.03%	-2.86%	-5.56%

D.2. Temporal variability

Horizontal velocity

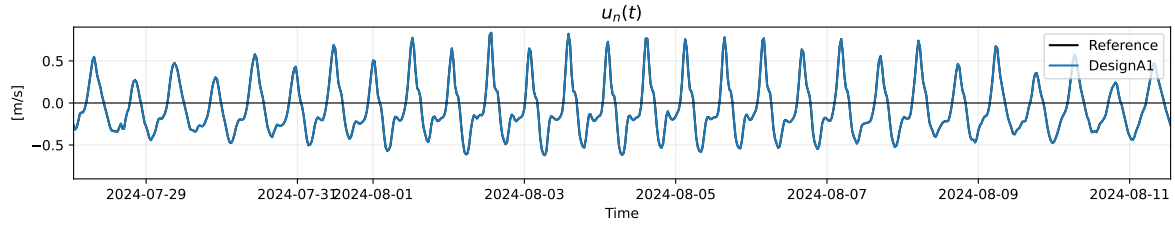

(a) Design A1

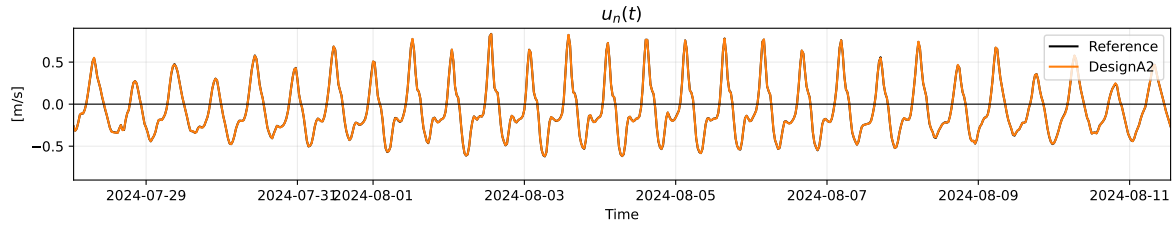

(b) Design A2

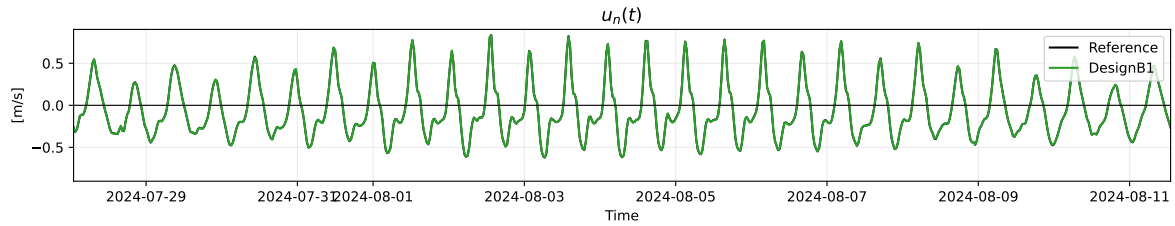

(c) Design B1

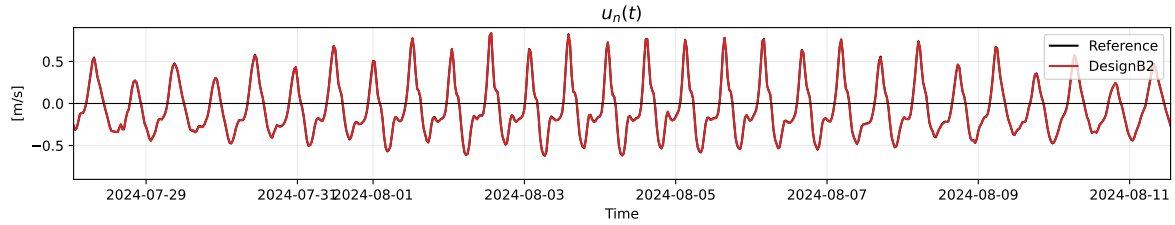

(d) Design B2

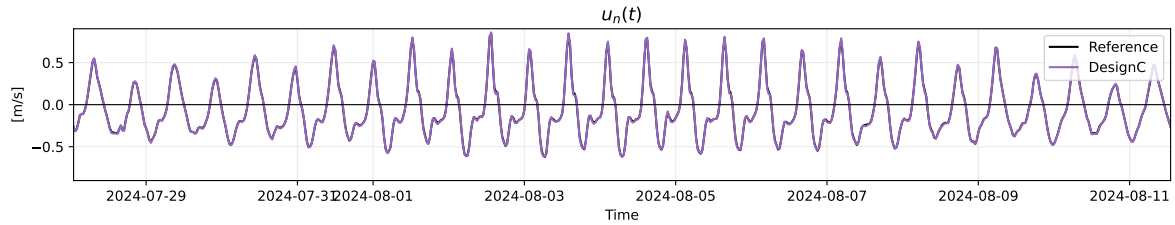

(e) Design C

Figure D.1: Temporal variability of the transect-integrated normal velocity component ($u_n(t)$) through the Maasmond over one spring–neap cycle for the Reference scenario and SPE designs.

IM1

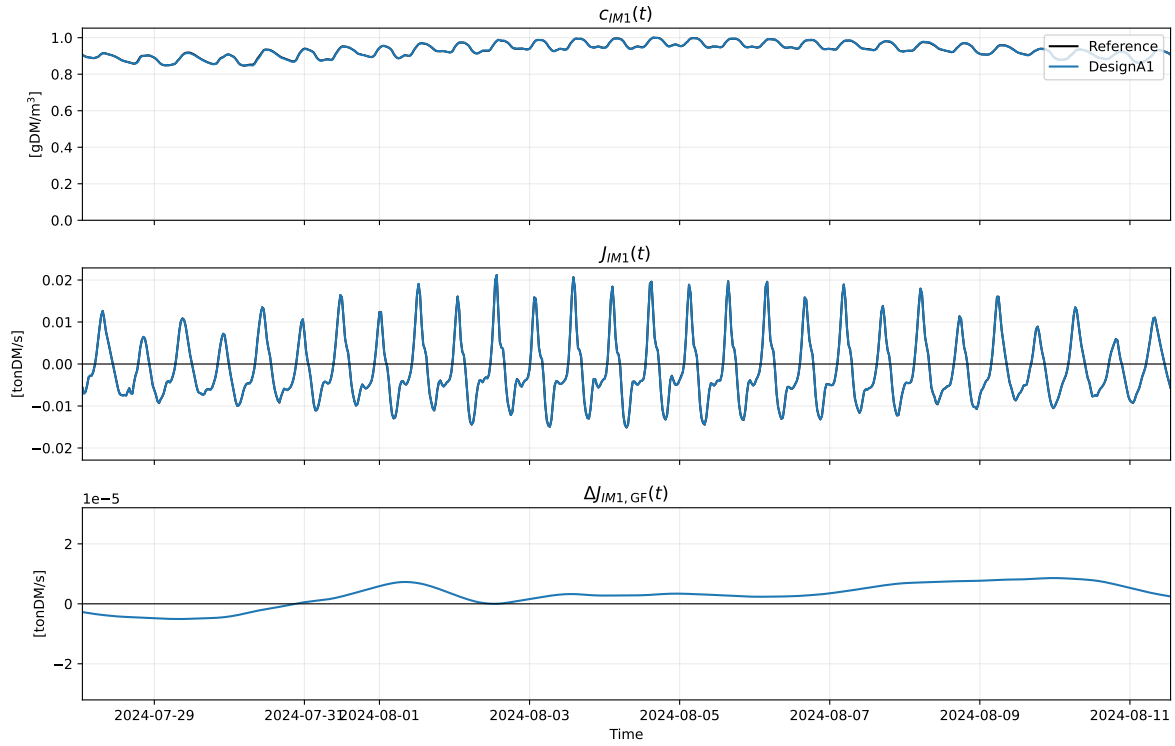

Figure D.2: Temporal variability of IM1 concentration (c_{IM1}), advective flux (J_{IM1}), and Godin-filtered flux difference ($\Delta J_{\mathrm{IM1,GF}}$) between Design A1 and the Reference scenario.

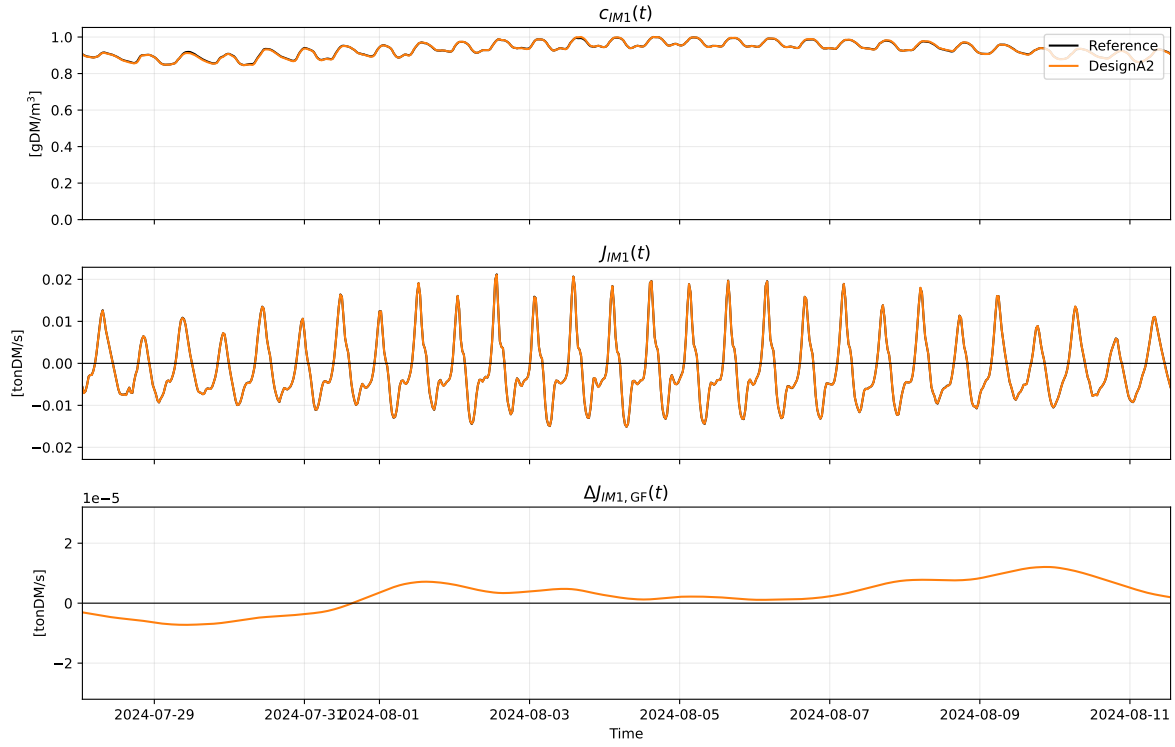

Figure D.3: Temporal variability of IM1 concentration (c_{IM1}), advective flux (J_{IM1}), and Godin-filtered flux difference ($\Delta J_{\mathrm{IM1,GF}}$) between Design A2 and the Reference scenario.

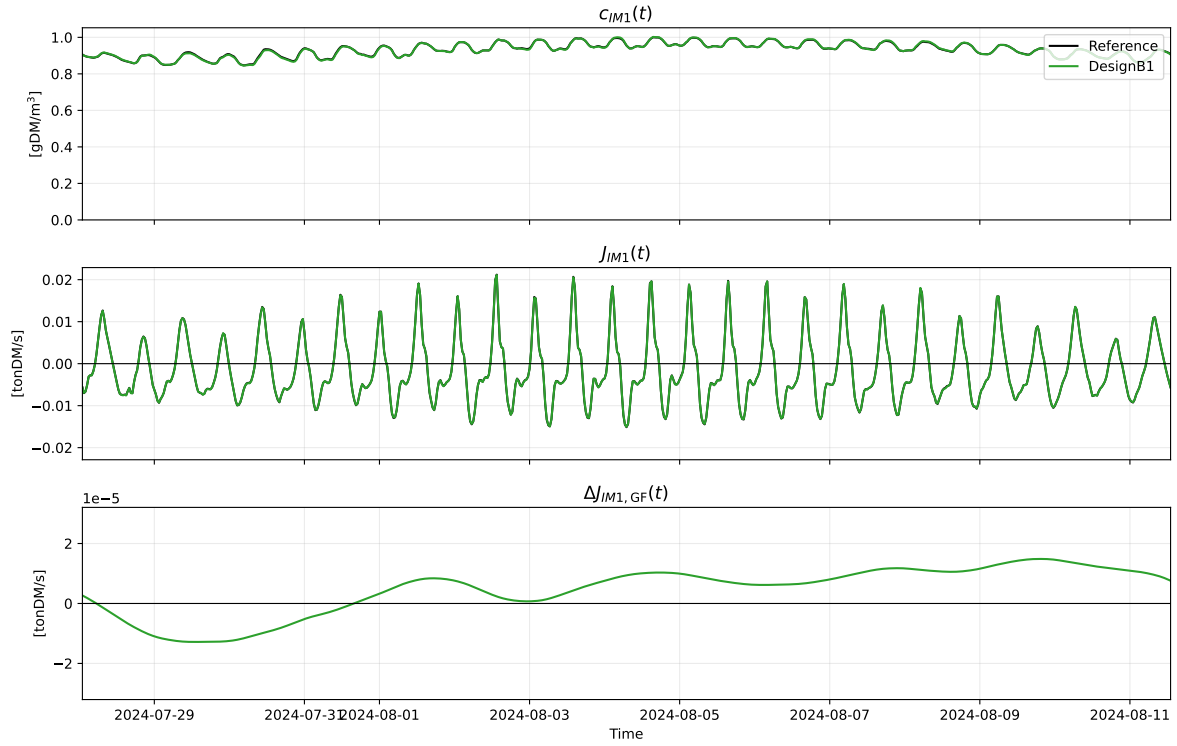

Figure D.4: Temporal variability of IM1 concentration (c_{IM1}), advective flux (J_{IM1}), and Godin-filtered flux difference ($\Delta J_{\mathrm{IM1,GF}}$) between Design B1 and the Reference scenario.

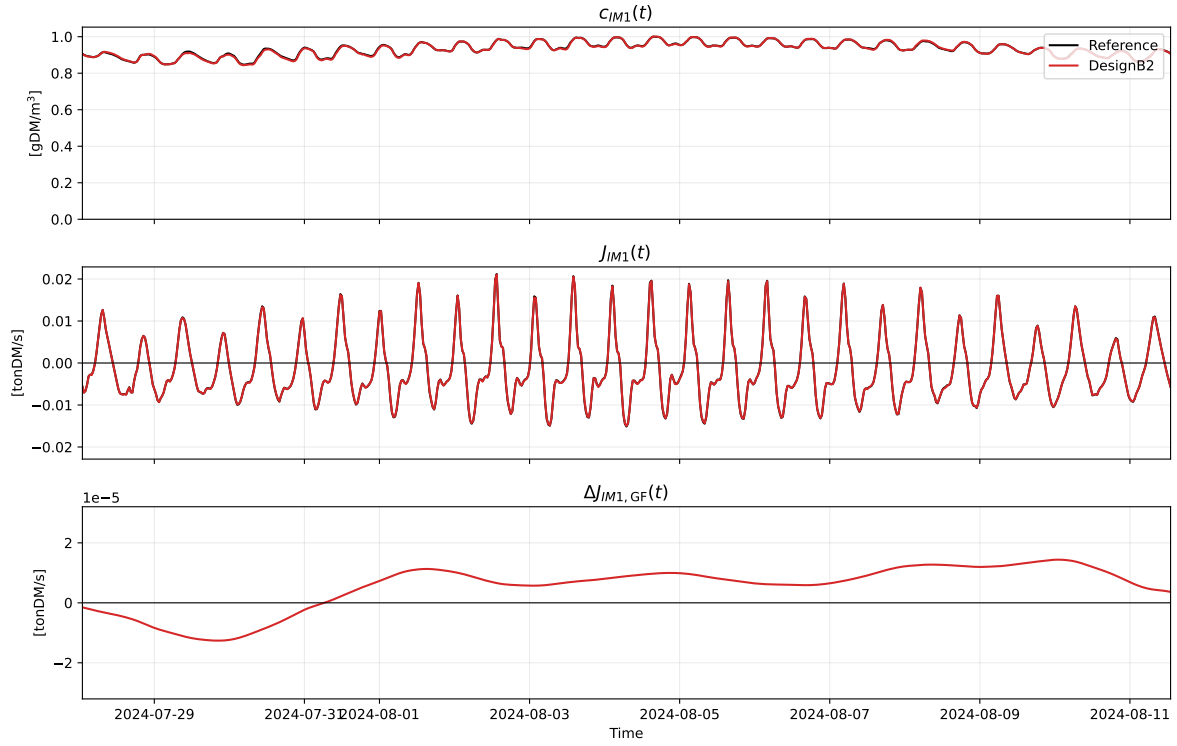

Figure D.5: Temporal variability of IM1 concentration (c_{IM1}), advective flux (J_{IM1}), and Godin-filtered flux difference ($\Delta J_{\mathrm{IM1,GF}}$) between Design B2 and the Reference scenario.

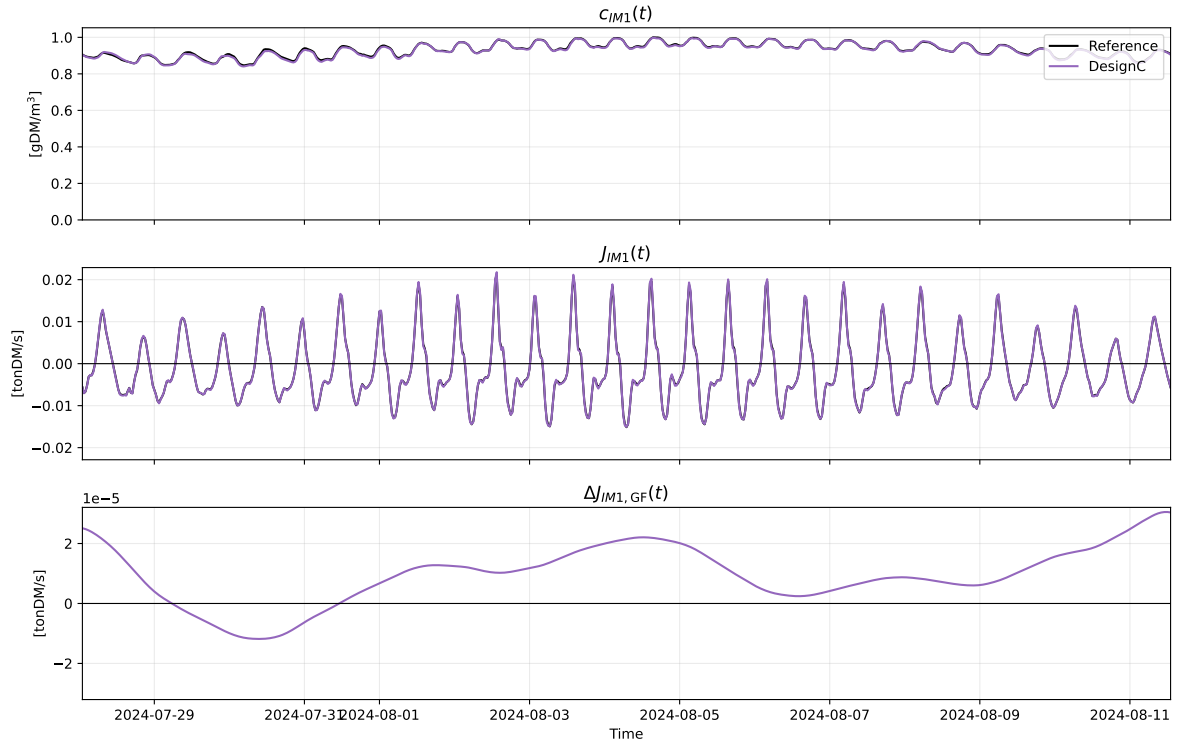

Figure D.6: Temporal variability of IM1 concentration (c_{IM1}), advective flux (J_{IM1}), and Godin-filtered flux difference ($\Delta J_{\mathrm{IM1,GF}}$) between Design C and the Reference scenario.

IM2

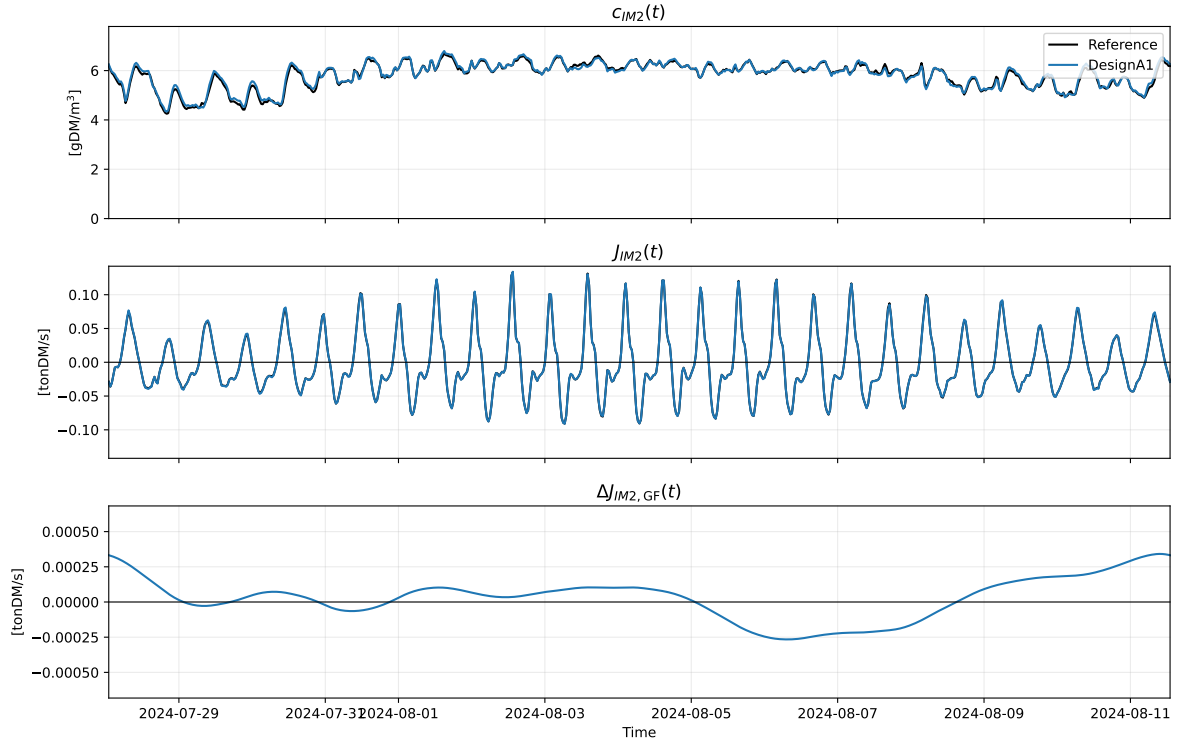

Figure D.7: Temporal variability of IM2 concentration (c_{IM2}), advective flux (J_{IM2}), and Godin-filtered flux difference ($\Delta J_{\mathrm{IM2,GF}}$) between Design A1 and the Reference scenario.

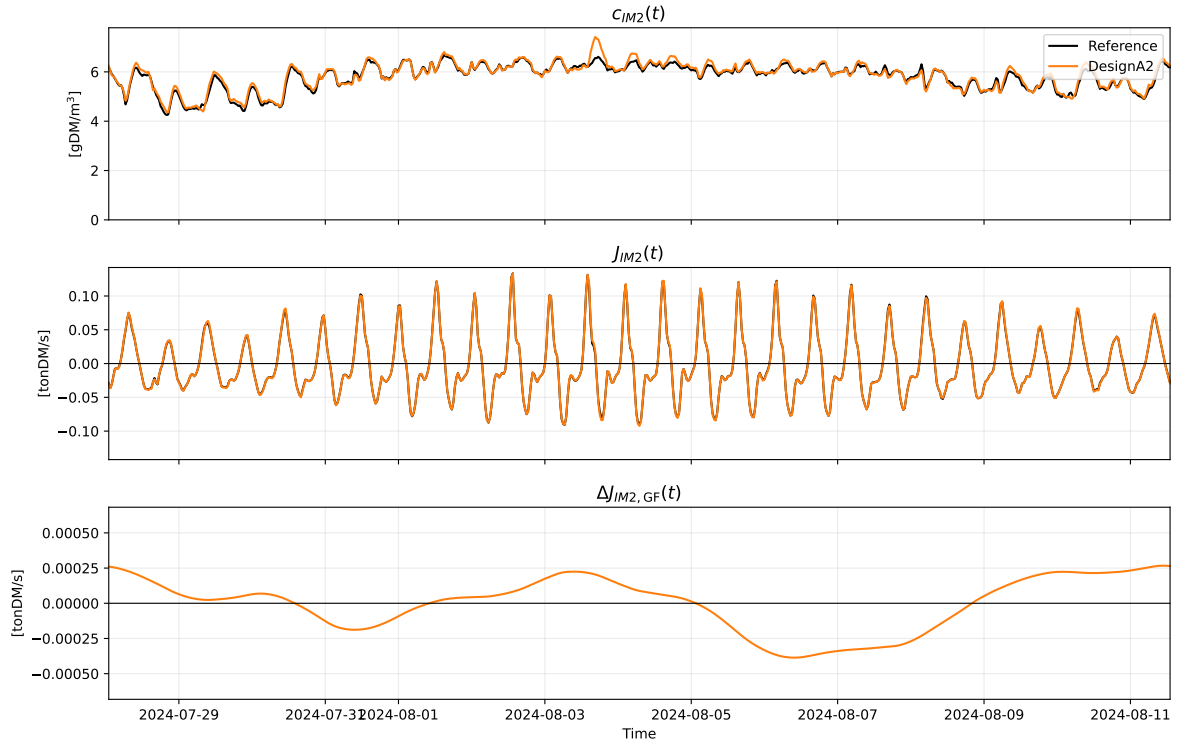

Figure D.8: Temporal variability of IM2 concentration (c_{IM2}), advective flux (J_{IM2}), and Godin-filtered flux difference ($\Delta J_{\mathrm{IM2,GF}}$) between Design A2 and the Reference scenario.

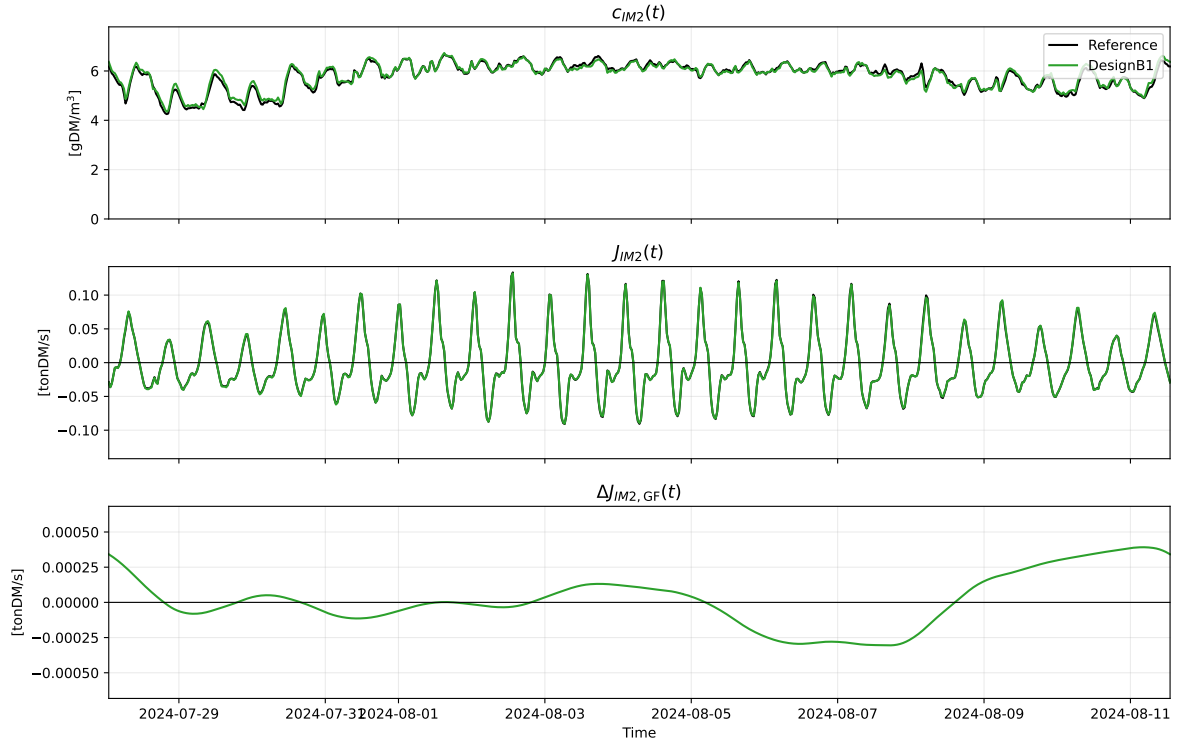

Figure D.9: Temporal variability of IM2 concentration (c_{IM2}), advective flux (J_{IM2}), and Godin-filtered flux difference ($\Delta J_{\mathrm{IM2,GF}}$) between Design B1 and the Reference scenario.

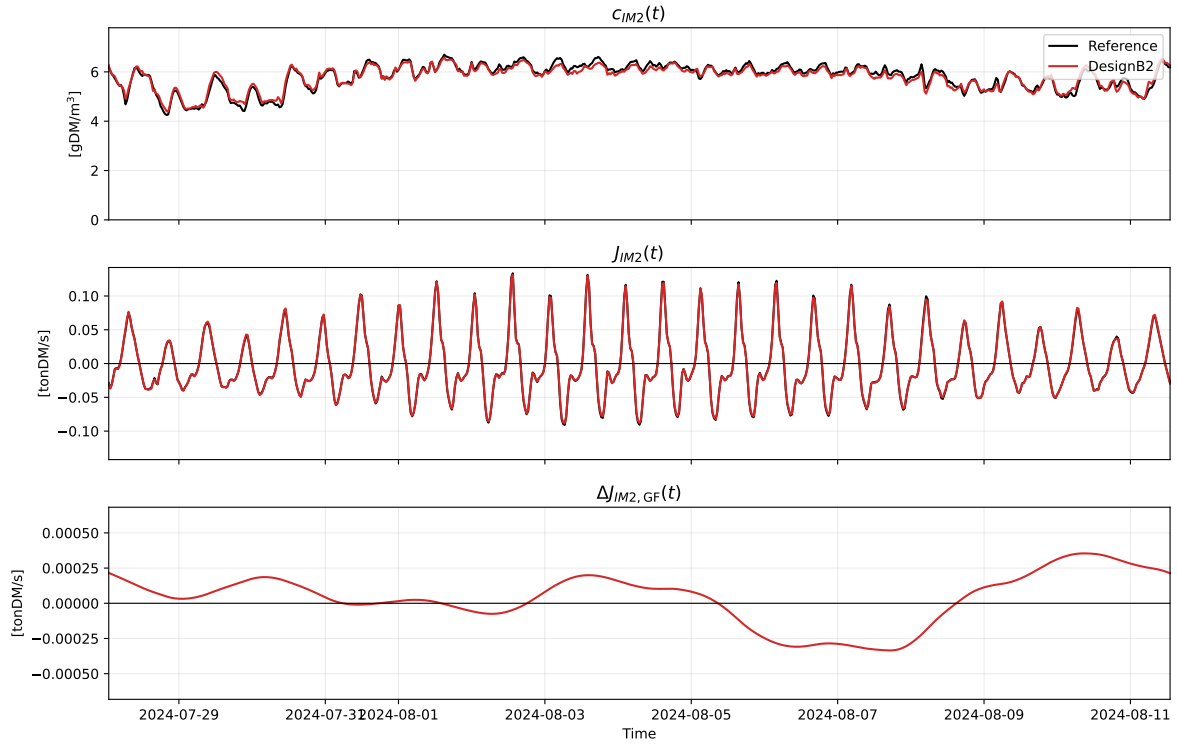

Figure D.10: Temporal variability of IM2 concentration (c_{IM2}), advective flux (J_{IM2}), and Godin-filtered flux difference ($\Delta J_{\mathrm{IM2,GF}}$) between Design B2 and the Reference scenario.

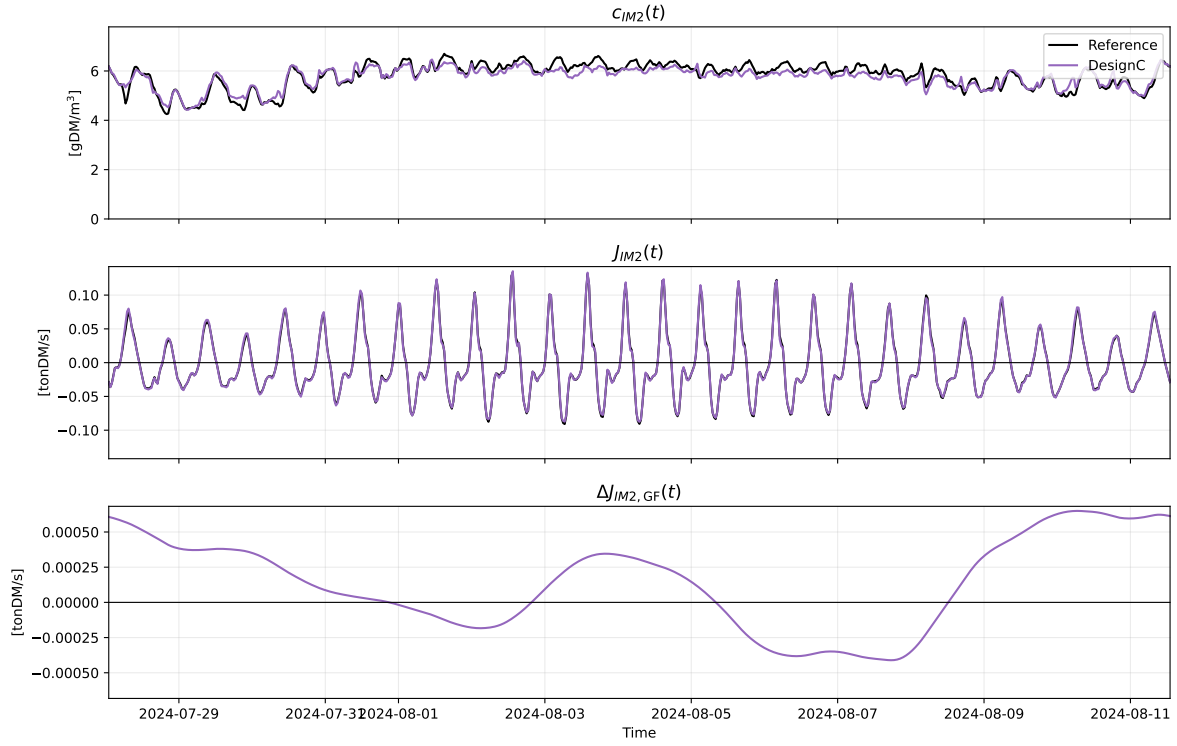

Figure D.11: Temporal variability of IM2 concentration (c_{IM2}), advective flux (J_{IM2}), and Godin-filtered flux difference ($\Delta J_{\mathrm{IM2,GF}}$) between Design C and the Reference scenario.

IM3

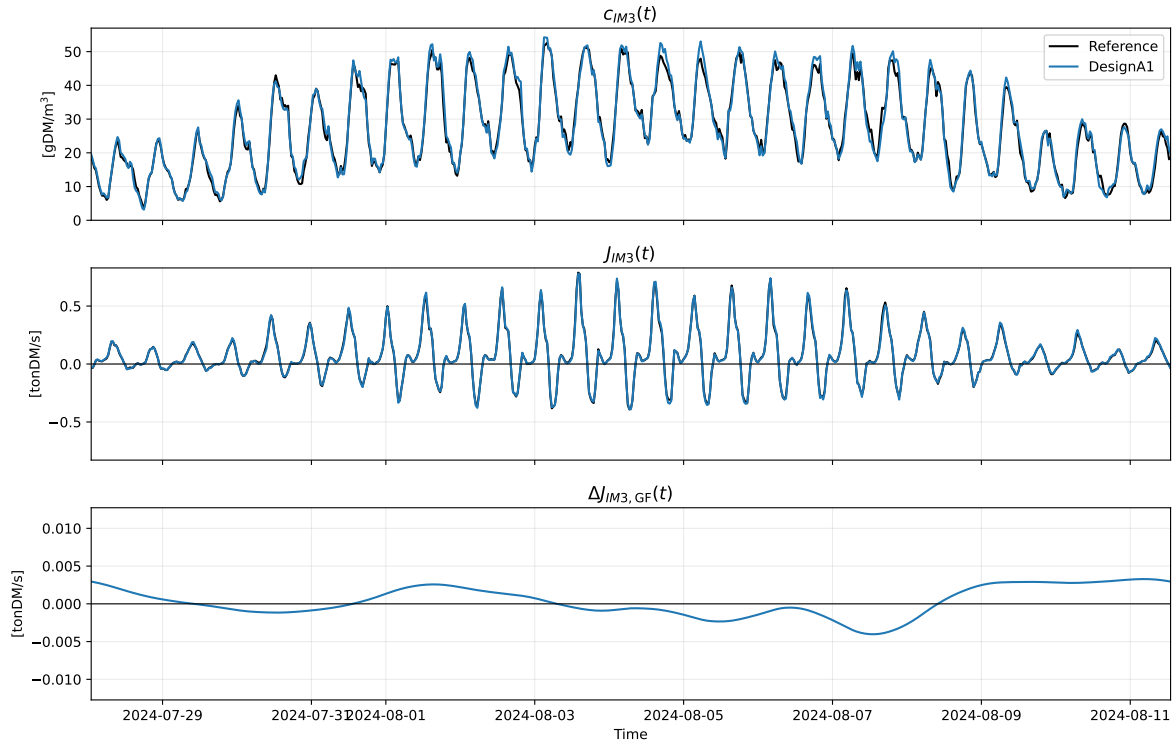

Figure D.12: Temporal variability of IM3 concentration (c_{IM3}), advective flux (J_{IM3}), and Godin-filtered flux difference ($\Delta J_{\mathrm{IM3,GF}}$) between Design A1 and the Reference scenario.

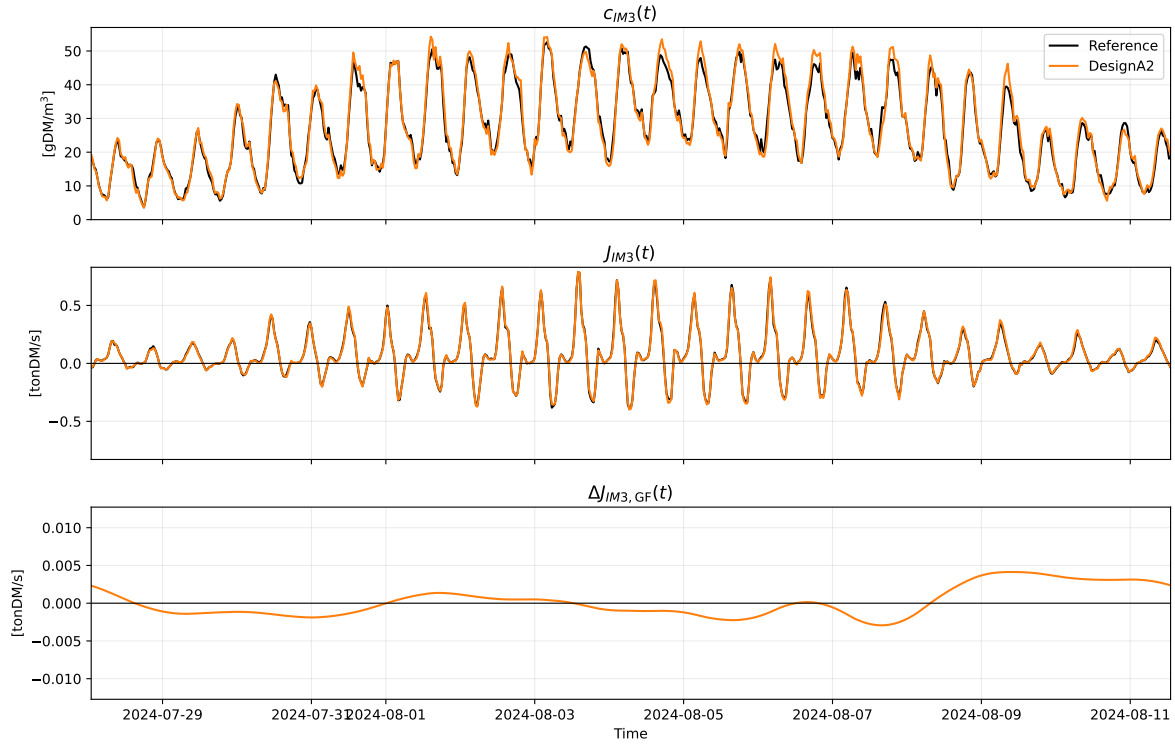

Figure D.13: Temporal variability of IM3 concentration (c_{IM3}), advective flux (J_{IM3}), and Godin-filtered flux difference ($\Delta J_{\mathrm{IM3,GF}}$) between Design A2 and the Reference scenario.

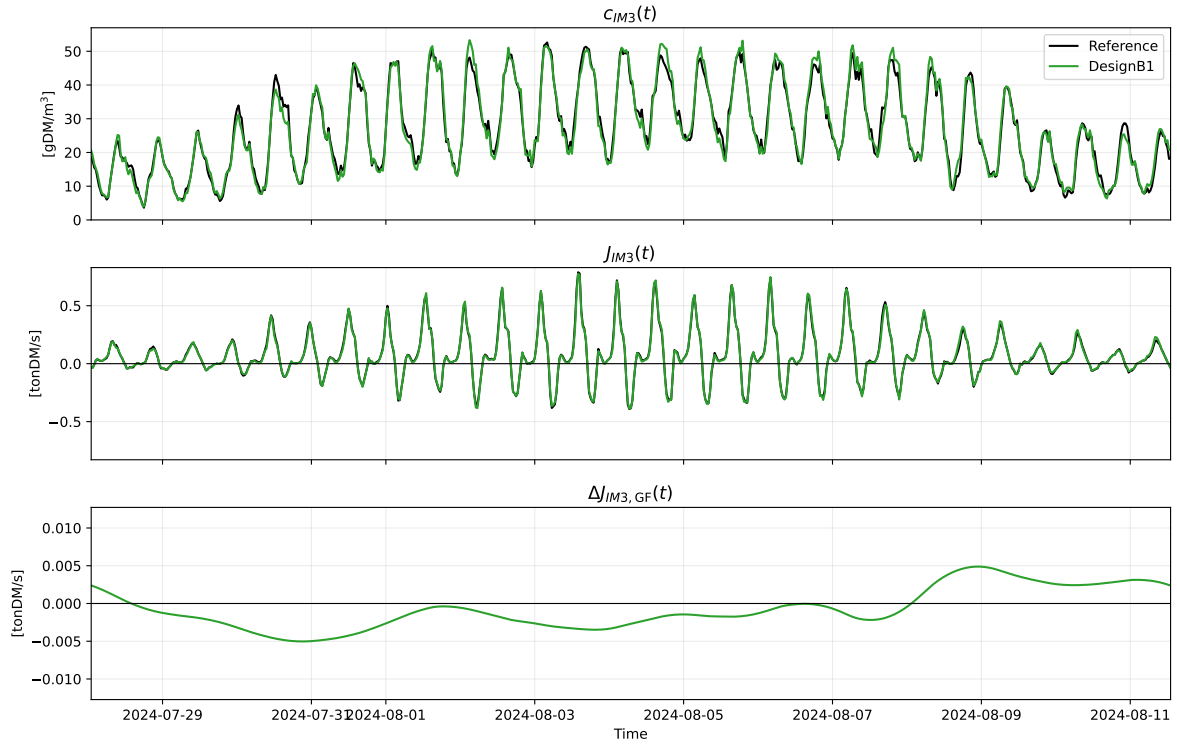

Figure D.14: Temporal variability of IM3 concentration (c_{IM3}), advective flux (J_{IM3}), and Godin-filtered flux difference ($\Delta J_{\mathrm{IM3,GF}}$) between Design B1 and the Reference scenario.

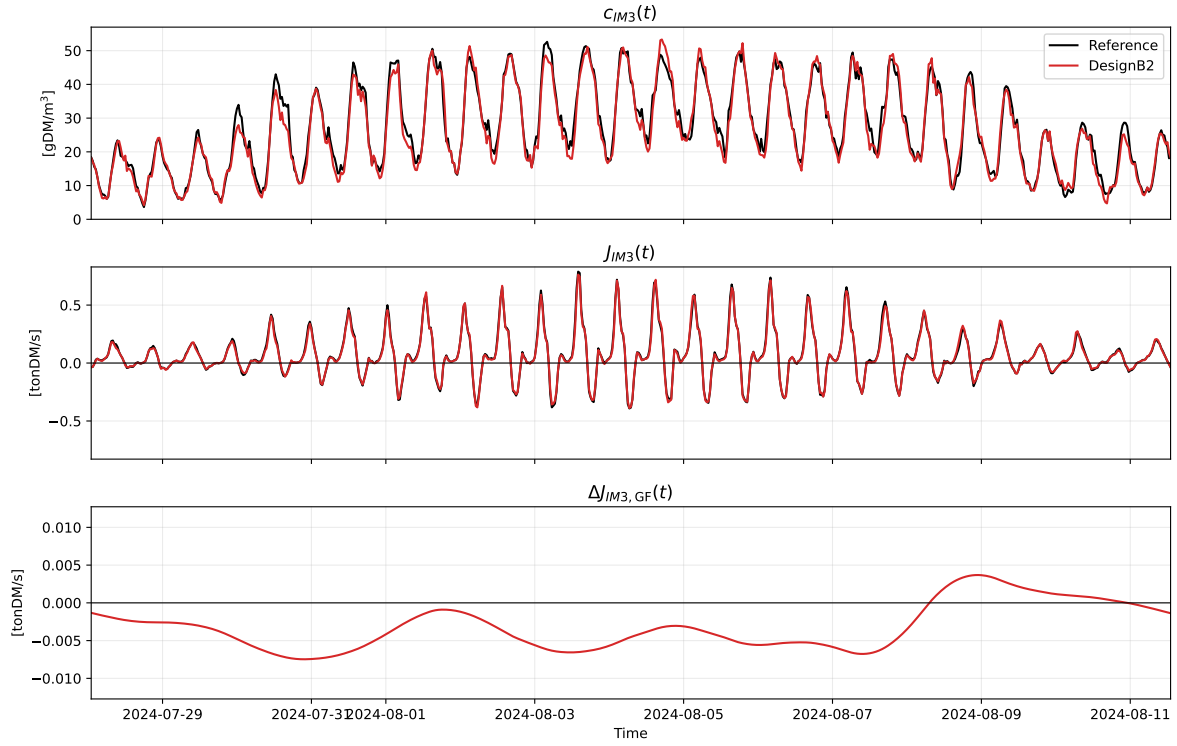

Figure D.15: Temporal variability of IM3 concentration (c_{IM3}), advective flux (J_{IM3}), and Godin-filtered flux difference ($\Delta J_{\mathrm{IM3,GF}}$) between Design B2 and the Reference scenario.

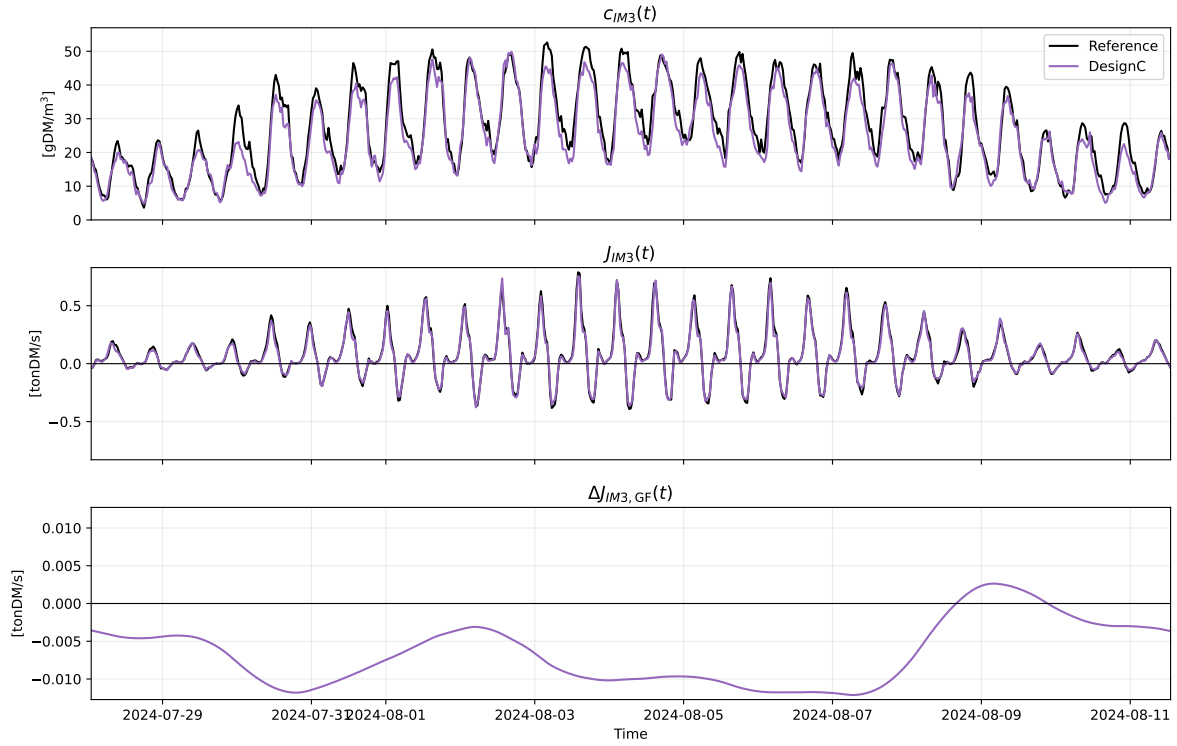

Figure D.16: Temporal variability of IM3 concentration (c_{IM3}), advective flux (J_{IM3}), and Godin-filtered flux difference ($\Delta J_{\mathrm{IM3,GF}}$) between Design C and the Reference scenario.

E

Port

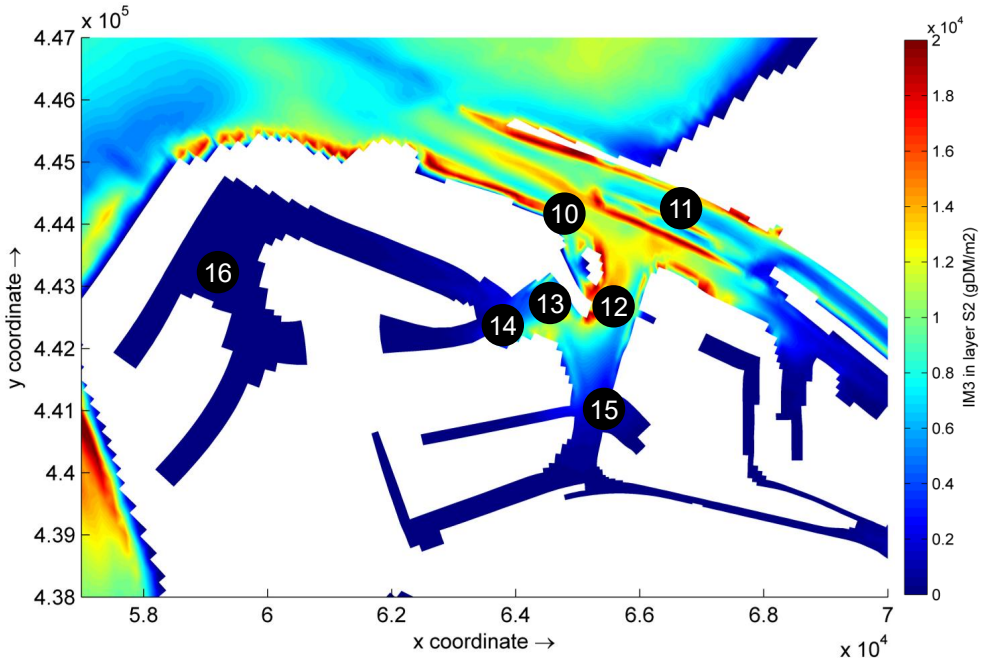

Figure E.1: IM3 bed mass in Layer S_2 at the end of the DELWAQ simulation ($M_{S2,\mathrm{IM3}}(t_1)$), with selected observation points indicated in the Port of Rotterdam.

Area 10

Table E.1: Observation point (82,57) — IM1

Scenario	ΔM_{bed} [gDM]	ΔM_{bed}	$\overline{\tau}_b$ [N/m^2]	$\Delta\tau_b$	$\overline{c}_{IM1}$ [gDM/m^3]	Δc_{IM1}
Reference	10.4	–	0.33	–	0.9	–
Design A1	10.4	+0.2%	0.33	-0.5%	0.9	-0.0%
Design A2	10.4	-0.1%	0.33	-0.6%	0.9	-0.1%
Design B1	10.4	-0.1%	0.33	-0.8%	0.9	-0.1%
Design B2	10.4	+0.2%	0.33	-1.1%	0.9	-0.2%
Design C	10.1	-2.5%	0.35	+3.9%	0.9	-0.4%

Table E.2: Observation point (82,57) — IM2

Scenario	ΔM_{bed} [gDM]	ΔM_{bed}	$\overline{\tau}_b$ [N/m^2]	$\Delta\tau_b$	$\overline{c}_{IM2}$ [gDM/m^3]	Δc_{IM2}
Reference	95.6	–	0.33	–	5.1	–
Design A1	96.0	+0.4%	0.33	-0.5%	5.1	+0.5%
Design A2	95.6	-0.0%	0.33	-0.6%	5.1	+0.2%
Design B1	96.3	+0.8%	0.33	-0.8%	5.1	+0.4%
Design B2	95.9	+0.3%	0.33	-1.1%	5.0	-0.2%
Design C	94.7	-0.9%	0.35	+3.9%	5.0	-0.8%

Table E.3: Observation point (82,57) — IM3

Scenario	ΔM_{bed} [gDM]	ΔM_{bed}	$\overline{\tau}_b$ [N/m^2]	$\Delta \tau_b$	$\overline{c}_{IM3}$ [gDM/m^3]	Δc_{IM3}
Reference	16,462.4	–	0.33	–	21.0	–
Design A1	16,727.5	+1.6%	0.33	-0.5%	21.3	+1.1%
Design A2	16,960.7	+3.0%	0.33	-0.6%	21.5	+2.5%
Design B1	16,971.2	+3.1%	0.33	-0.8%	21.3	+1.6%
Design B2	16,685.9	+1.4%	0.33	-1.1%	20.7	-1.5%
Design C	15,300.2	-7.1%	0.35	+3.9%	19.0	-9.6%

Area 11

Table E.4: Observation point (114,48) — IM1

Scenario	ΔM_{bed} [gDM]	ΔM_{bed}	$\overline{\tau}_b$ [N/m^2]	$\Delta \tau_b$	$\overline{c}_{IM1}$ [gDM/m^3]	Δc_{IM1}
Reference	9.8	–	0.42	–	0.9	–
Design A1	9.8	-0.0%	0.42	+0.2%	0.9	-0.0%
Design A2	9.8	-0.1%	0.42	+0.4%	0.9	-0.0%
Design B1	9.8	-0.2%	0.42	+0.5%	0.9	-0.1%
Design B2	9.8	-0.1%	0.42	+0.9%	0.9	-0.1%
Design C	9.9	+0.1%	0.42	+1.2%	0.9	-0.2%

Table E.5: Observation point (114,48) — IM2

Scenario	ΔM_{bed} [gDM]	ΔM_{bed}	$\overline{\tau}_b$ [N/m^2]	$\Delta \tau_b$	$\overline{c}_{IM2}$ [gDM/m^3]	Δc_{IM2}
Reference	90.7	–	0.42	–	5.5	–
Design A1	90.7	+0.1%	0.42	+0.2%	5.5	+0.3%
Design A2	90.4	-0.3%	0.42	+0.4%	5.5	-0.0%
Design B1	90.5	-0.1%	0.42	+0.5%	5.5	+0.1%
Design B2	90.3	-0.4%	0.42	+0.9%	5.5	-0.2%
Design C	90.6	-0.0%	0.42	+1.2%	5.5	-0.3%

Table E.6: Observation point (114,48) — IM3

Scenario	ΔM_{bed} [gDM]	ΔM_{bed}	$\overline{\tau}_b$ [N/m^2]	$\Delta \tau_b$	$\overline{c}_{IM3}$ [gDM/m^3]	Δc_{IM3}
Reference	6,225.6	–	0.42	–	10.6	–
Design A1	6,169.0	-0.9%	0.42	+0.2%	10.7	+0.5%
Design A2	6,199.3	-0.4%	0.42	+0.4%	10.6	-0.0%
Design B1	6,079.4	-2.3%	0.42	+0.5%	10.5	-1.4%
Design B2	5,896.3	-5.3%	0.42	+0.9%	10.2	-3.9%
Design C	5,697.5	-8.5%	0.42	+1.2%	9.7	-8.4%

Area 12

Table E.7: Observation point (101,66) — IM1

Scenario	ΔM_{bed} [gDM]	ΔM_{bed}	$\overline{\tau}_b$ [N/m^2]	$\Delta \tau_b$	$\overline{c}_{IM1}$ [gDM/m^3]	Δc_{IM1}
Reference	21.9	–	0.13	–	0.8	–
Design A1	22.0	+0.5%	0.13	+0.0%	0.8	-0.0%
Design A2	22.2	+1.2%	0.13	-0.2%	0.8	-0.1%
Design B1	22.2	+1.5%	0.13	-2.1%	0.8	-0.2%
Design B2	21.8	-0.4%	0.13	-0.6%	0.8	-0.3%
Design C	17.3	-20.8%	0.15	+14.9%	0.8	-0.6%

Table E.8: Observation point (101,66) — IM2

Scenario	ΔM_{bed} [gDM]	ΔM_{bed}	$\overline{\tau}_b$ [N/m^2]	$\Delta \tau_b$	$\overline{c}_{IM2}$ [gDM/m^3]	Δc_{IM2}
Reference	143.1	–	0.13	–	5.3	–
Design A1	144.5	+1.0%	0.13	+0.0%	5.3	+0.3%
Design A2	144.9	+1.3%	0.13	-0.2%	5.2	-0.5%
Design B1	144.7	+1.1%	0.13	-2.1%	5.3	+0.2%
Design B2	143.6	+0.3%	0.13	-0.6%	5.2	-0.7%
Design C	131.4	-8.2%	0.15	+14.9%	5.2	-1.4%

Table E.9: Observation point (101,66) — IM3

Scenario	ΔM_{bed} [gDM]	ΔM_{bed}	$\overline{\tau}_b$ [N/m^2]	$\Delta \tau_b$	$\overline{c}_{IM3}$ [gDM/m^3]	Δc_{IM3}
Reference	24,237.0	–	0.13	–	11.5	–
Design A1	24,452.1	+0.9%	0.13	+0.0%	11.6	+1.1%
Design A2	24,020.5	-0.9%	0.13	-0.2%	11.4	-0.7%
Design B1	24,513.9	+1.1%	0.13	-2.1%	11.5	-0.3%
Design B2	22,790.3	-6.0%	0.13	-0.6%	10.9	-5.0%
Design C	18,081.5	-25.4%	0.15	+14.9%	10.5	-8.5%

Area 13

Table E.10: Observation point (84,70) — IM1

Scenario	ΔM_{bed} [gDM]	ΔM_{bed}	$\overline{\tau}_b$ [N/m^2]	$\Delta \tau_b$	$\overline{c}_{IM1}$ [gDM/m^3]	Δc_{IM1}
Reference	65.6	–	0.01	–	0.8	–
Design A1	65.6	-0.1%	0.01	+1.1%	0.8	-0.1%
Design A2	65.5	-0.3%	0.01	-0.3%	0.8	-0.1%
Design B1	65.4	-0.4%	0.01	-2.5%	0.8	-0.3%
Design B2	65.4	-0.3%	0.01	-1.1%	0.8	-0.3%
Design C	65.5	-0.3%	0.01	+23.0%	0.8	-0.5%

Table E.11: Observation point (84,70) — IM2

Scenario	ΔM_{bed} [gDM]	ΔM_{bed}	$\overline{\tau}_b$ [N/m^2]	$\Delta \tau_b$	$\overline{c}_{IM2}$ [gDM/m^3]	Δc_{IM2}
Reference	1,176.5	–	0.01	–	6.0	–
Design A1	1,189.2	+1.1%	0.01	+1.1%	6.0	+0.2%
Design A2	1,191.3	+1.3%	0.01	-0.3%	6.0	-0.3%
Design B1	1,185.7	+0.8%	0.01	-2.5%	6.0	-0.1%
Design B2	1,180.6	+0.3%	0.01	-1.1%	5.9	-0.8%
Design C	1,108.3	-5.8%	0.01	+23.0%	5.7	-4.3%

Table E.12: Observation point (84,70) — IM3

Scenario	ΔM_{bed} [gDM]	ΔM_{bed}	$\overline{\tau}_b$ [N/m^2]	$\Delta \tau_b$	$\overline{c}_{IM3}$ [gDM/m^3]	Δc_{IM3}
Reference	56,558.8	–	0.01	–	8.4	–
Design A1	57,617.3	+1.9%	0.01	+1.1%	8.3	-0.8%
Design A2	58,702.6	+3.8%	0.01	-0.3%	8.4	+0.0%
Design B1	56,283.3	-0.5%	0.01	-2.5%	8.2	-2.1%
Design B2	54,321.8	-4.0%	0.01	-1.1%	7.8	-7.0%
Design C	51,460.1	-9.0%	0.01	+23.0%	8.1	-3.4%

Area 14

Table E.13: Observation point (80,76) — IM1

Scenario	ΔM_{bed} [gDM]	ΔM_{bed}	$\overline{\tau}_b$ [N/m^2]	$\Delta \tau_b$	$\overline{c}_{IM1}$ [gDM/m^3]	Δc_{IM1}
Reference	59.3	–	0.01	–	0.7	–
Design A1	59.3	+0.0%	0.01	+1.5%	0.7	-0.1%
Design A2	59.4	+0.1%	0.01	+1.6%	0.7	+0.0%
Design B1	59.2	-0.2%	0.01	+0.0%	0.7	-0.2%
Design B2	59.2	-0.2%	0.01	+1.3%	0.7	-0.3%
Design C	59.3	+0.1%	0.01	+10.1%	0.7	-0.7%

Table E.14: Observation point (80,76) — IM2

Scenario	ΔM_{bed} [gDM]	ΔM_{bed}	$\overline{\tau}_b$ [N/m^2]	$\Delta \tau_b$	$\overline{c}_{IM2}$ [gDM/m^3]	Δc_{IM2}
Reference	1,576.6	–	0.01	–	4.6	–
Design A1	1,574.6	-0.1%	0.01	+1.5%	4.6	+0.2%
Design A2	1,570.0	-0.4%	0.01	+1.6%	4.6	-0.5%
Design B1	1,567.3	-0.6%	0.01	+0.0%	4.6	-0.2%
Design B2	1,571.7	-0.3%	0.01	+1.3%	4.6	-0.9%
Design C	1,432.6	-9.1%	0.01	+10.1%	4.3	-6.4%

Table E.15: Observation point (80,76) — IM3

Scenario	ΔM_{bed} [gDM]	ΔM_{bed}	$\overline{\tau}_b$ [N/m^2]	$\Delta \tau_b$	$\overline{c}_{IM3}$ [gDM/m^3]	Δc_{IM3}
Reference	11,129.8	–	0.01	–	1.1	–
Design A1	10,932.0	-1.8%	0.01	+1.5%	1.0	-2.0%
Design A2	10,883.8	-2.2%	0.01	+1.6%	1.0	-2.6%
Design B1	10,565.5	-5.1%	0.01	+0.0%	1.0	-5.0%
Design B2	10,726.3	-3.6%	0.01	+1.3%	1.0	-3.8%
Design C	12,252.4	+10.1%	0.01	+10.1%	1.3	+21.1%

Area 15

Table E.16: Observation point (103,78) — IM1

Scenario	ΔM_{bed} [gDM]	ΔM_{bed}	$\overline{\tau}_b$ [N/m^2]	$\Delta \tau_b$	$\overline{c}_{IM1}$ [gDM/m^3]	Δc_{IM1}
Reference	62.2	–	0.04	–	0.8	–
Design A1	62.1	-0.1%	0.04	-1.4%	0.8	-0.0%
Design A2	62.2	+0.0%	0.04	-1.9%	0.8	-0.1%
Design B1	62.0	-0.4%	0.04	-1.1%	0.8	-0.2%
Design B2	62.1	-0.1%	0.04	-1.0%	0.8	-0.2%
Design C	62.6	+0.7%	0.04	+6.9%	0.8	-0.1%

Table E.17: Observation point (103,78) — IM2

Scenario	ΔM_{bed} [gDM]	ΔM_{bed}	$\overline{\tau}_b$ [N/m^2]	$\Delta \tau_b$	$\overline{c}_{IM2}$ [gDM/m^3]	Δc_{IM2}
Reference	911.9	–	0.04	–	4.8	–
Design A1	922.3	+1.1%	0.04	-1.4%	4.9	+0.6%
Design A2	926.5	+1.6%	0.04	-1.9%	4.8	+0.2%
Design B1	914.6	+0.3%	0.04	-1.1%	4.8	+0.1%
Design B2	913.8	+0.2%	0.04	-1.0%	4.8	-0.5%
Design C	882.1	-3.3%	0.04	+6.9%	4.7	-2.8%

Table E.18: Observation point (103,78) — IM3

Scenario	ΔM_{bed} [gDM]	ΔM_{bed}	$\overline{\tau}_b$ [N/m^2]	$\Delta \tau_b$	$\overline{c}_{IM3}$ [gDM/m^3]	Δc_{IM3}
Reference	14,383.0	–	0.04	–	2.7	–
Design A1	14,872.1	+3.4%	0.04	-1.4%	2.7	+1.6%
Design A2	15,596.1	+8.4%	0.04	-1.9%	2.8	+4.8%
Design B1	14,588.3	+1.4%	0.04	-1.1%	2.7	+1.2%
Design B2	14,820.0	+3.0%	0.04	-1.0%	2.7	+1.3%
Design C	15,425.7	+7.2%	0.04	+6.9%	2.8	+3.9%

Area 16

Table E.19: Observation point (44,96) — IM1

Scenario	ΔM_{bed} [gDM]	ΔM_{bed}	$\overline{\tau}_b$ [N/m^2]	$\Delta \tau_b$	$\overline{c}_{IM1}$ [gDM/m^3]	Δc_{IM1}
Reference	40.7	–	0.00	–	0.5	–
Design A1	39.9	-2.0%	0.00	+1.4%	0.5	-0.2%
Design A2	39.9	-2.0%	0.00	+1.6%	0.5	-0.0%
Design B1	39.6	-2.7%	0.00	+0.2%	0.5	-0.5%
Design B2	39.6	-2.8%	0.00	+0.8%	0.5	-0.4%
Design C	33.2	-18.4%	0.00	-6.8%	0.4	-13.5%

Table E.20: Observation point (44,96) — IM2

Scenario	ΔM_{bed} [gDM]	ΔM_{bed}	$\overline{\tau}_b$ [N/m^2]	$\Delta \tau_b$	$\overline{c}_{IM2}$ [gDM/m^3]	Δc_{IM2}
Reference	652.5	–	0.00	–	2.6	–
Design A1	654.1	+0.2%	0.00	+1.4%	2.7	+0.5%
Design A2	655.3	+0.4%	0.00	+1.6%	2.6	+0.2%
Design B1	644.4	-1.2%	0.00	+0.2%	2.6	-1.0%
Design B2	641.5	-1.7%	0.00	+0.8%	2.6	-1.0%
Design C	603.3	-7.5%	0.00	-6.8%	1.2	-53.6%

Table E.21: Observation point (44,96) — IM3

Scenario	ΔM_{bed} [gDM]	ΔM_{bed}	$\overline{\tau}_b$ [N/m^2]	$\Delta \tau_b$	$\overline{c}_{IM3}$ [gDM/m^3]	Δc_{IM3}
Reference	17.1	–	0.00	–	-0.0	–
Design A1	3.3	-80.8%	0.00	+1.4%	0.0	-108.2%
Design A2	2.9	-83.0%	0.00	+1.6%	0.0	-109.0%
Design B1	6.1	-64.7%	0.00	+0.2%	-0.0	-76.9%
Design B2	48.7	+184.2%	0.00	+0.8%	-0.0	+634.6%
Design C	2.7	-84.0%	0.00	-6.8%	0.0	-106.5%